

## A NEAR-INFRARED CENSUS OF THE MULTI-COMPONENT STELLAR STRUCTURE OF EARLY-TYPE DWARF GALAXIES IN THE VIRGO CLUSTER

J. JANZ<sup>1,2,\*</sup>, E. LAURIKAINEN<sup>3,1</sup>, T. LISKER<sup>2</sup>, H. SALO<sup>1</sup>, R. F. PELETIER<sup>4</sup>, S.-M. NIEMI<sup>5</sup>, E. TOLOBA<sup>6,7</sup>, G. HENSLER<sup>8</sup>,  
J. FALCÓN-BARROSO<sup>9,10</sup>, A. BOSELLI<sup>11</sup>, M. DEN BROK<sup>4,12</sup>, K. S. A. HANSSON<sup>2</sup>, H. T. MEYER<sup>2</sup>, A. RYS<sup>9,10</sup>, S. PAUDEL<sup>13,2</sup>

<sup>1</sup>Division of Astronomy, Department of Physics, P.O. Box 3000, FI-90014 University of Oulu, Finland

<sup>2</sup>Astronomisches Rechen-Institut, Zentrum für Astronomie der Universität Heidelberg, Mönchhofstraße 12-14, D-69120 Heidelberg, Germany

<sup>3</sup>Finnish Centre for Astronomy with ESO (FINCA), University of Turku, Finland

<sup>4</sup>Kapteyn Astronomical Institute, University of Groningen, PO Box 800, 9700 AV Groningen, the Netherlands

<sup>5</sup>Mullard Space Science Laboratory, University College London, Holmbury St. Mary, Dorking, Surrey RH5 6NT, United Kingdom

<sup>6</sup>UCO/Lick Observatory, University of California, Santa Cruz, 1156 High Street, Santa Cruz, CA 95064

<sup>7</sup>Observatories of the Carnegie Institution of Washington, 813 Santa Barbara Street, Pasadena, CA 91101

<sup>8</sup>University of Vienna, Institute of Astronomy, Türkenschanzstraße 17, 1180 Vienna, Austria

<sup>9</sup>Instituto de Astrofísica de Canarias, Vía Láctea s/n, La Laguna, Tenerife, Spain

<sup>10</sup>Departamento de Astrofísica, Universidad de La Laguna, E-38205 La Laguna, Tenerife, Spain

<sup>11</sup>Aix Marseille Université, CNRS, LAM (Laboratoire d'Astrophysique de Marseille) UMR 7326, 13388, Marseille, France

<sup>12</sup>Department of Physics and Astronomy, University of Utah, Salt Lake City, Utah 84112, USA

<sup>13</sup>Laboratoire AIM Paris-Saclay, CNRS/INSU, Université Paris Diderot, CEA/IRFU/SaP, 91191 Gif-sur-Yvette Cedex, France

### ABSTRACT

The fraction of star-forming to quiescent dwarf galaxies varies from almost infinity in the field to zero in the centers of rich galaxy clusters. What is causing this pronounced morphology-density relation? What do quiescent dwarf galaxies look like when studied in detail, and what conclusions can be drawn about their formation mechanism? Here we study a nearly magnitude-complete sample ( $-19 < M_r < -16$  mag) of 121 Virgo cluster early types with deep near-infrared images from the SMAKCED project. We fit two-dimensional models with optional inner and outer components, as well as bar and lens components (in  $\sim 15\%$  of the galaxies), to the galaxy images. While a single Sérsic function may approximate the overall galaxy structure, it does not entirely capture the light distribution of two-thirds of our galaxies, for which multi-component models provide a better fit. This fraction of complex galaxies shows a strong dependence on luminosity, being larger for brighter objects. We analyze the global and component-specific photometric scaling relations of early-type dwarf galaxies and discuss similarities with bright early and late types. The dwarfs' global galaxy parameters show scaling relations that are similar to those of bright disk galaxies. The inner components are mostly fitted with Sérsic  $n$  values close to 1. At a given magnitude they are systematically larger than the bulges of spirals, suggesting that they are not ordinary bulges. We argue that the multi-component structures in early-type dwarfs are mostly a phenomenon inherent to the disks, and may indeed stem from environmental processing.

*Keywords:* galaxies: elliptical and lenticular, cD — galaxies: dwarf — galaxies: photometry — galaxies: structure — galaxies: clusters: individual: (Virgo Cluster)

### 1. INTRODUCTION

Early-type dwarf galaxies populate the Universe in large numbers, their number counts dominate over other galaxy types in clusters, and yet their formation is a widely disputed topic. Their name reflects their morphological resemblance to giant early-type galaxies: both are elliptical in shape and have a featureless appearance with little ongoing star formation and only small amounts of gas and dust. Therefore, they are often called “dwarf ellipticals” (Binggeli, Sandage, & Tammann 1985, but see Kormendy et al. 2009 for a different view). They possibly follow a similar color-magnitude relation as bright ellipticals (e.g. Mieske et al. 2007; Smith Castelli et al. 2008; Misgeld et al. 2008, see however recent studies for Virgo: Ferrarese et al. 2006; Janz & Lisker 2009; Chen et al. 2010), and their sizes and locus in the Kormendy relation may or may not be explained by a continuous variation of the profile shape with galaxy brightness (Graham & Guzmán 2003; Ferrarese et al. 2006, see also Graham 2011 for a review; for an alternative view see e.g. Kormendy et al. 2009). Furthermore,

the early-type dwarfs are preferably found in high density environments of galaxy clusters and manifest the morphology-density relation similar to giant ellipticals (Dressler 1980; for dwarfs see Ferguson & Binggeli 1994; and within the early-type dwarfs, Lisker et al. 2007).

Where do these galaxies come from? A priori it is, despite the similarities, not known whether the name “dwarf elliptical” is justified, i.e. that they are small low mass versions of giant ellipticals (Wirth & Gallagher 1984). There are several indications that this is not the case (Kormendy et al. 2009 and references therein). Alternatively, it was proposed that they developed their spheroidal non-starforming appearance during a transformation from a late-type galaxy in a cluster environment (Kormendy 1985). Due to the morphology-density relation such a mechanism is expected to depend highly on the environment. Suggested processes include ram pressure stripping (Boselli et al. 2008b,a; de Rijcke, van Hese, & Buyle 2010), which may also heat the disk (Smith et al. 2012a), and harassment (Moore et al. 1998; Mastropietro et al. 2005; Smith et al. 2010). While it still remains to be shown in detail that these mechanisms are efficient enough, they all will inevitably act in the cluster environment to some extent. Further aspects might also play a role: the time the galaxy spent within the cluster, i.e. in-situ formation (Toloba et al. 2009; Lisker et al. 2009), an infall into the cluster early on, or a

Based on observations collected at the European Organisation for Astronomical Research in the Southern Hemisphere, Chile, under programme IDs 064.N-0288 and 085.B-0919.

Electronic address: [jjanz@ari.uni-heidelberg.de](mailto:jjanz@ari.uni-heidelberg.de)

\* Fellow of the Gottlieb Daimler and Karl Benz Foundation.

more recent infall. Also, the relevance of mergers at these low masses is expected to be smaller as compared to giant ellipticals (De Lucia et al. 2012; Lisker et al. 2013), but nonetheless interactions take place even today (Martinez-Delgado et al. 2012).

Already Binggeli & Cameron (1991) partially described the heterogeneity of this galaxy class, but it was fully appreciated only recently (Graham & Guzmán 2003; Lisker et al. 2007; Michielsen et al. 2008; Lisker et al. 2009; Toloba et al. 2009, 2011; Koleva et al. 2011 as a biased list of references). The diversity in different galaxy parameters might call for a number of processes shaping the galaxies, with varying importances depending on the evolutionary history of the individual galaxy.

The SMAKCED project (Stellar content,  $M_{\text{Ass}}$  and Kinematics of Cluster Early-type Dwarfs) aims at a more complete understanding of the origin of the early-type dwarf galaxies. We target a complete magnitude limited sample of early-type galaxies in the Virgo cluster in a brightness range where all the different morphological subclasses and varieties of stellar content and kinematical configuration coexist. In order to reveal more details of their presumably heterogeneous evolutionary histories, we want to gain a detailed picture of their morphology with deep near-infrared images and, for a subsample of galaxies, of their kinematics. The near-infrared is particularly useful for our purpose, since it is sensitive to the bulk of the stellar mass. Here we report on our progress with deducing the distributions of stars with two-dimensional multi-component decompositions for the observed 121 galaxies, some initial results of which were presented in Janz et al. (2012).

In Section 2 the sample selection, observations, and data reductions are described. Section 3 summarizes the analysis including multi-component decompositions and non-elliptical isophotal shapes. In Section 4 the results are presented. The analyzed multi-component structures are then compared to those found in bright galaxies in Section 5. The results are discussed in Section 6, and we conclude with the summary in Section 7.

## 2. SAMPLE, OBSERVATIONS, & DATA

### 2.1. Sample

Within SMAKCED we obtained deep near-infrared (NIR)  $H$ -band images for 121 early-type galaxies in the Virgo Cluster. The sample is drawn from the Virgo cluster catalog (VCC, Binggeli, Sandage, & Tammann 1985, with updated memberships by heliocentric velocities from the literature, Lisker et al. 2006a) and spans three magnitudes within  $-19 \text{ mag} < M_r < -16 \text{ mag}$  (Fig. 1, assuming a distance modulus for Virgo of  $m - M = 31.09 \text{ mag}$ , Mei et al. 2007). In total there are 174 galaxies fulfilling these criteria. Our observations are complete down to  $M_r = -16.76 \text{ mag}$ , with images for 121 of the galaxies. The brightness range and sample size guarantee that it is possible to study galaxy parameters binned according to the various early-type dwarf galaxy subclasses (Lisker et al. 2006a,b, 2007), galaxy brightness, local environment, or rotational support (Toloba et al. 2009, 2011) with a sufficient number of galaxies in each bin (see Table 1 = Table 1). Furthermore, some galaxies that were classified as normal (non-dwarf) early types (Binggeli, Sandage, & Tammann 1985) overlap with the early-type dwarf galaxies in this brightness range (e.g. Janz & Lisker 2008).

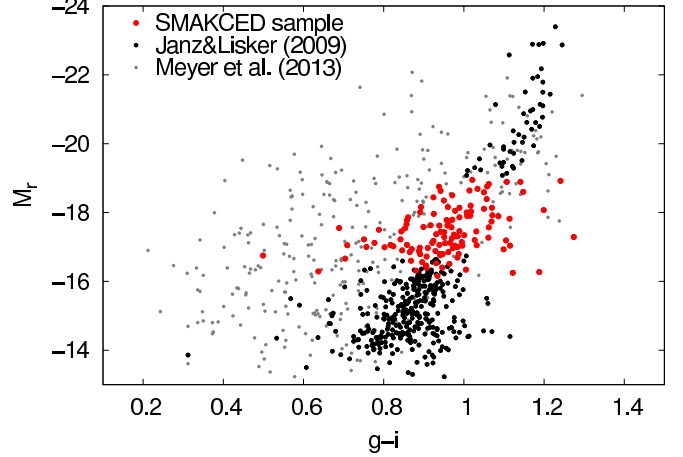


**Figure 1.** The curved  $g-i$  color-magnitude relation of early types in the Virgo cluster from Janz & Lisker (2009). Galaxies that we observed within SMAKCED in the near-infrared are highlighted with *red* color. For comparison the *small gray* symbols in the background display the colors of late-type galaxies in the Virgo cluster (Meyer et al. 2013).

**Table 1**  
Sample

	dE(N)	dE(nN)	dE(di)	dE(bc)	E	SO
$19 \leq M_r \leq -18 \text{ mag}$						
$d_{M87} \leq 1.5^\circ$	1	0	2	0	1	1
$1.5 < d_{M87} \leq 4^\circ$	2	1	4	0	2	4
$d_{M87} > 4^\circ$	3	0	2	0	2	2
$-18 < M_r \leq -17 \text{ mag}$						
$d_{M87} \leq 1.5^\circ$	8	2	3	3	1	1
$1.5 < d_{M87} \leq 4^\circ$	15	0	10	4	2	1
$d_{M87} > 4^\circ$	3	0	4	3	0	2
$-17 < M_r \leq -16 \text{ mag}$						
$d_{M87} \leq 1.5^\circ$	4	1	0	1	2	1
$1.5 < d_{M87} \leq 4^\circ$	6	2	1	2	0	0
$d_{M87} > 4^\circ$	5	0	4	1	0	2

**Note.** — Galaxies binned over basic parameters;  $d_{M87}$  is the angular distance to M87. At the distance of the Virgo Cluster  $1^\circ = 0.284 \text{ Mpc}$ . The classification of the bright galaxies is taken from the VCC (Binggeli, Sandage, & Tammann 1985) and the early-type dwarf subclasses from (Lisker et al. 2006a,b, 2007).

### 2.2. Observations

The observations were done in the NIR allowing the most direct measurement of the distribution of stellar mass in galaxies (e.g. Bell & de Jong 2001). This wavelength is also less affected by dust, which is present even in some of the early-type dwarf galaxies (de Looze et al. 2010). We choose the  $H$ -band, since the observations are more efficient than in the  $K$ -band, and the  $J$ -band is less optimal for characterizing the old stellar population, i.e. the distribution of stellar mass, since it has a shorter wavelength. During the last two years, we obtained images for 97 galaxies using SOFI at ESO/NTT, NICS at TNG, and NOTCam at NOT with the wide-field option (085.B-0919; AOT21/CAT\_193, AOT23/CAT\_102; P41-217, P42-047, P42-212, P43-038, P43-206). The data is complemented with archival data for some bright galaxies (from ESO

NTT/SOFI, 064.N-0288,<sup>2</sup> P.I. A. Boselli; from NOT, Niemi).

The integration times were calculated for each galaxy individually, in order to reach a signal to noise ( $S/N$ ) of 1 per pixel ( $\sim 0''.25 \times 0''.25$ , see Table 2 = Table 2) at 2 half-light radii. The half-light radii were determined on the Sloan Digital Sky Survey (SDSS)  $r$ -band images (Janz & Lisker 2008). The  $H$ -band surface brightness was estimated by measuring the surface brightness in the  $i$ -band (Janz & Lisker 2009) and converting it to the  $H$ -band with a conservative value of  $i-H = 1.7$  mag, based on the  $i-H$  colors for some of the galaxies from SDSS and the archival  $H$ -band data. Generally, we limited the total on-source integration time to three hours. Notice that, the galaxies with low surface brightnesses typically have large sizes, and therefore the effective  $S/N$  is comparable to that in galaxies with higher surface brightnesses.

For a few bright galaxies we integrated longer than their calculated exposure times, in order to reach at least a surface brightness of  $22.2$  mag arcsec<sup>-2</sup>. Typically we reach a surface brightness of  $22.2$ – $23.0$  mag arcsec<sup>-2</sup>, at a  $S/N$  of 1 per pixel. In some cases the upper limit in the integration time, the weather, or the use of archival data resulted in an image depth shallower than desired.

Most of the observations were carried out by dithering the galaxy to the centers of the detector’s four quadrants, since the detectors are sufficiently large ( $\sim 4' \times 4'$ ). This way the sky was obtained simultaneously with the target observation. A good sampling of the bright and variable NIR sky is essential to accurately subtract it (see §2.3). A few galaxies exceeded the size of one quadrant of the detector, or bright foreground stars hampered our dithering strategy. In those cases a customized 3-point dither pattern or beam-switching with separate sky observations were used. With each instrument and for each target we tried to optimize the exposure times for single exposures so that we stayed within the linear regime of the detector, while minimizing the overheads. Typical values for the number of exposures per pointing (NDIT) and for the single exposure time (DIT) were  $10 \times 6$ s for NOTCam and SOFI, while for NICS it was  $3 \times 25$ s. With NOTCam we used the ramp-sampling mode, which allows to read out the detector during the exposure: linear regression applied to the several times sampled signal reduces the noise. The observations are summarized in Table 3.

### 2.3. Reduction

#### 2.3.1. Instrumental effects: flat fields, crosstalk

The data reduction was mostly carried out using our own IRAF<sup>3</sup> scripts. Two of the detectors (SOFI and NICS) suffer from an unwanted effect called crosstalk. This effect causes ghost images of bright sources in some other quadrant of the detector and can enhance the signal in the affected rows or columns. To deal with this problem, we first remove the crosstalk from the images using scripts provided by the observatories (`crosstalk.cl` for SOFI and a FORTRAN script from the SNAP package for NICS). The removal works well for sources that do not exceed the linearity range of the detector. Subsequently, the images are flat fielded. For the three instruments we follow the recommended procedures and use

“special” dome flats<sup>4</sup> for SOFI, differential skyflats for NOTCam, and skyflats for NICS data. For convenience we normalize the images to 1s exposure times.

#### 2.3.2. Sky subtraction

It is crucial to perform the sky subtraction with high accuracy, since the surface brightnesses we are aiming at are on the order of  $10$  mag arcsec<sup>-2</sup> fainter than the sky. Typically we average the sky over the frames taken in a time window of 10–15 minutes around the observation. The length of the time interval is adjusted to the variability of the sky. Any sources (including the target) need to be carefully masked out down to low surface brightnesses. It is unfeasible to create appropriate masks on the single exposures. Therefore, we iterate the reduction process and create the masks on preliminary coadded images with SExtractor (Bertin & Arnouts 1996).

For averaging the masked sky frames, they need to be scaled to a common flux level. Since there can be gradients in the sky over the field of view, it is important to compensate for the masked out regions in the scaling. We find appropriate values for the masked pixels by filling them with fits of fourth order polynomials to the unmasked pixels in each quadrant of the detector. Note that the reconstructed pixels are used only to find the appropriate scaling, not for the averaged sky frame that is then subtracted from the image. The rows and columns of the detector can have a slightly different output. We average over rows and columns, and subtract the result from the image to obtain the final flat foreground subtracted single exposure. When averaging, we again use the masks and compensate for the masked pixels.

In order to assess the quality of the sky subtraction, we measure the sky levels in small boxes of  $21 \times 21$  pixels distributed across the final coadded images. When scaled to the average noise in the individual coadded image, a width of  $1/\sqrt{21 \times 21} = 0.05$  is expected for the distribution if the noise is Gaussian. The expected width is slightly larger if pixels in some boxes are not used due to masked out objects. Moreover, the noise follows overall a pattern due to the used dithering: the central part of the galaxy is imaged every time ( $\sigma_{\text{center}}$ ), parts at the edges in half of the exposures ( $\sigma_{\text{edge}} = \sqrt{2}\sigma_{\text{center}}$ ) and in the corners in every fourth exposure ( $\sigma_{\text{corner}} = 2\sigma_{\text{center}}$ ), for the standard pattern. Fig. 2 shows the measurements in units of the average noise in the individual coadded image. For comparison, we plot a normal distribution ( $\sigma = 0.125$ ) and a combination of three normal distributions accounting for the overall noise pattern. We conclude that the increased width in comparison to the expectation is due to correlated noise and variations of the background on larger scales. These variations are considered in the evaluation of the fitted models in Section §3.4 and the profile figures there.

#### 2.3.3. Illumination correction

During the observing run in March 2012 we observed one standard star in two nights (with NICS and NOTCam) on a  $5$  by  $5$  grid of different positions on the detectors. The measured fluxes of the standard star vary at a  $\sim 10\%$  level depending on the position on the detector (the reason for that is not fully understood, see Hodgkin et al. 2009). The variations are systematic so that they form a smooth surface. We fit second

<sup>2</sup> Obtained via the ESO archive, <http://archive.eso.org>.

<sup>3</sup> IRAF is distributed by the National Optical Astronomy Observatory, which is operated by the Association of Universities for Research in Astronomy (AURA) under cooperative agreement with the National Science Foundation.

<sup>4</sup> The “special” dome flats reduce the bias by a different illumination of the dome flat screen as compared to the sky by additionally considering exposures with the lamp shining only on parts of the screen, see SOFI manual.



**Table 2**  
Telescopes and cameras

Telescope	Diameter	Camera	Detector	Pixel scale	Field of view	Read noise
New Technology Telescope (ESO/NTT)	3.58m	SOFI	1024 × 1024 HAWAII	0.''288/pix	4'92 × 4'92	11.34 e <sup>-</sup>
Telescopio Nazionale Galileo (TNG)	3.58m	NICS	1024 × 1024 HAWAII	0.''25/pix	4'2 × 4'2	24 e <sup>-</sup>
Nordic Optical Telescope (NOT)	2.56m	NOTCam	1024 × 1024 HAWAII	0.''234/pix	4' × 4'	8 e <sup>-</sup>

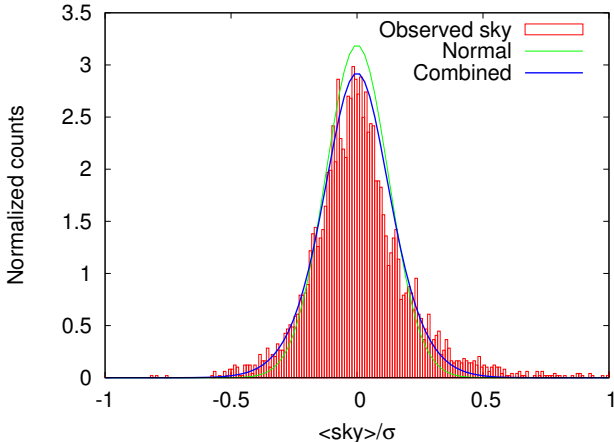


**Figure 2.** Sky values measured in small boxes of 21x21 pixels across the images in units of the noise in the image. The Gaussian has a variance of  $\sigma = 0.125$ , the combined curve adds three Gaussians accounting for the overall pattern in the  $\sigma$ -image (see text).

order polynomials to the surfaces using IRAF/surfit and apply the normalized fits as an illumination correction to the science frames. The illumination correction might vary with time. Therefore, we compare the fitted surface to the brightness variations across the detector using stars in the science frames of two photometric nights in 2010 (Appendix A). From that comparison we conclude that the possible error from a time-dependence of the illumination correction is smaller than the error that would be made without the correction. Indeed, when applying the illumination correction, the scatter of the zeropoints (determined by comparison of sources in the field-of-view to 2MASS and UKIDSS, see §2.5) is reduced.

#### 2.3.4. Distortion correction, alignment, and coaddition

NICS at TNG and NOTCam at NOT suffer from optical distortions large enough to hamper the alignment of the dithered images for coaddition: the galaxy and the stars have different distances depending on the positions on the detector. In the corners the pixels are shifted up to about 10 or 13 pixels for NICS and NOTCam, respectively, relative to their position on an undistorted image. Therefore, we use the IRAF/geotran task and distortion maps to transform the images to geometrically flat images. For NICS the distortion map was extracted from the SNAP pipeline, and for NOTCam the distortions were provided by Magnus Gålfalk. The NTT images have been found to be astrometrically flat to a 0.1% level (Tinney, Burgasser, & Kirkpatrick 2003).

The distortion corrected single exposures are aligned using the IRAF/xregister task. The signal of the galaxy is measured in a small galaxy aperture and the noise on all non-masked pixels. The single exposures are coadded using these values as scales and weights, in order to optimize the  $S/N$  of the final image. During the coaddition, we mask out the detectors' bad

pixels. In some cases a perfect alignment of the images is impossible due to an imperfect modeling of the field distortions. Then we optimize the alignment for the region of the image where the galaxy is located. Since stars in other parts will not be perfectly aligned and since the seeing conditions can vary during the integration time, it is important not to do a clipping in the averaging process. In that case some of the flux of the imperfect stars would be lost and the calibration of the images would be biased. Finally, the averages in lines and columns, masking all sources, are subtracted from the coadded image.

#### 2.4. $\sigma$ -images and PSF

The many single exposures are used to estimate the uncertainties of the flux in each pixel. For all pixels in the final coadded image we calculate the standard deviations. These noise maps we call subsequently  $\sigma$ -images. They will be used later when fitting models to the galaxy's light distribution (§3.4).<sup>5</sup> Finally, the full width at half maximum (FWHM) of the point spread function (PSF) is determined as the average of the FWHM values of the point sources, measured on the coadded images with SExtractor (see Table 3).

#### 2.5. Flux Calibration

The images are calibrated using point sources in the field of view and comparing their fluxes to the magnitudes given in the 2MASS point source (Skrutskie et al. 2006) and UKIDSS catalogues (Lawrence et al. 2007).<sup>6</sup> This has the advantage of obtaining reliable photometry also for the data taken under non-photometric conditions. We require the sources to be sufficiently point-like and the photometric errors to be small. Also too bright sources are rejected in order to be sufficiently in the linear regime of the detector (for details see Appendix A). Typically there are 15 comparison objects in the field of view of the coadded images. The median error of the zeropoints, estimated by the scatter and number of stars used for the determination in each frame, is about 2% (see also Appendix A). Both, the scatter of the zeropoints, determined by individual sources in one field-of-view, and the scatter of the final, averaged zeropoints used for the galaxies are reduced when applying the illumination correction.

Finally, the images are corrected for galactic extinction according to Schlegel, Finkbeiner, & Davis (1998).

### 3. METHODOLOGY

In this paper we look at non-parametric photometric parameters of the galaxies, at the profiles of the disk/boxy characteristics of the isophotes, and carry out a two-dimensional multicomponent structural analysis. Our approach for the decompositions is different from the traditional one-dimensional

<sup>5</sup> For the archival data from the NTT we approximate the  $\sigma$ -images with a constant value of the average noise in the images.

<sup>6</sup> Like 2MASS and UKIDSS, we use the Vega system for our NIR magnitudes. The UKIDSS and 2MASS filter systems are slightly different. We convert the UKIDSS catalog values to the 2MASS system using Hewett et al. (2006).

method for identifying such structures, which considers the azimuthally averaged profiles as well as an isophotal analysis based on ellipse fitting. All the analyses are described in the following paragraphs, and the choice of the two-dimensional decomposition approach is reasoned in Section §3.4.

### 3.1. Non-parametric photometry

First, we want to derive basic non-parametric photometry parameters for all of the galaxies in the sample. We follow a similar procedure as in [Janz & Lisker \(2008\)](#): we determine an aperture, in which we will measure the flux, in terms of the Petrosian radius. The Petrosian radius  $r_p$  ([Petrosian 1976](#)) is the radius at which the intensity drops to a fifth of the mean intensity within this radius,<sup>7</sup>

$$\frac{I(r_p)}{\langle I \rangle_{r_p}} = 0.2. \quad (1)$$

Instead of circles we use ellipses so that we obtain a ‘‘Petrosian semi major axis (SMA)’’ (see, e.g. [Lotz et al. 2004](#)). The total flux of the galaxy is then measured within the aperture of two Petrosian SMA. Immediately, also a value for the half-light SMA can be obtained. The axis ratio and position angle of the aperture are first determined by the image moments within the circular aperture ([Abraham et al. 1994](#)), and after one iteration of the whole process by IRAF/ellipse at an SMA twice the half-light SMA.

Depending on the profile shape a certain fraction of the flux falls outside the aperture. We correct our total magnitudes and half-light apertures for the missed flux according to [Graham et al. \(2005\)](#). However, typically the correction is small, since the early-type dwarf profiles are mostly not much more concentrated than an exponential profile. Our method was shown to be consistent with other curve-of-growth methods ([Chen et al. 2010](#) for early types in Virgo with SDSS data). In the following we denote the SMA of the half-light aperture by  $r_e$ .

Furthermore, we want to quantify the galaxy concentrations in a model-independent way. We follow [Conselice \(2003\)](#) and measure the concentration within 1.5 Petrosian SMA as

$$C = 5 \log r_{80}/r_{20} \quad (2)$$

([Bershady, Jangren & Conselice 2000](#)), with the radii containing 20% and 80% of the light.

### 3.2. Ellipse fitting

We run IRAF/ellipse to measure light profiles, profiles of ellipticity and position angle, as well as parameters for non-elliptical isophotal shape. For that purpose we fix the center of the galaxy, while leaving the position angle and ellipticity as free fitting parameters. In the case of the isophotal shapes we fit the isophotes in steps of 1.1 pixels in order to get detailed profiles, whereas all the other fits are done with a bigger step size, resulting in less noisy measurements.

We also perform ellipse fitting for the two-dimensional decomposition models in Section §3.4. These measurements are done using the same apertures for the observations and the models in order to be directly comparable. We choose to measure the observations, the models, and the individual components along the isophotes obtained by fits to the models.

<sup>7</sup> Other authors use different values (e.g. [Conselice, Gallagher, & Wyse 2002](#); [Conselice et al. 2003](#)).

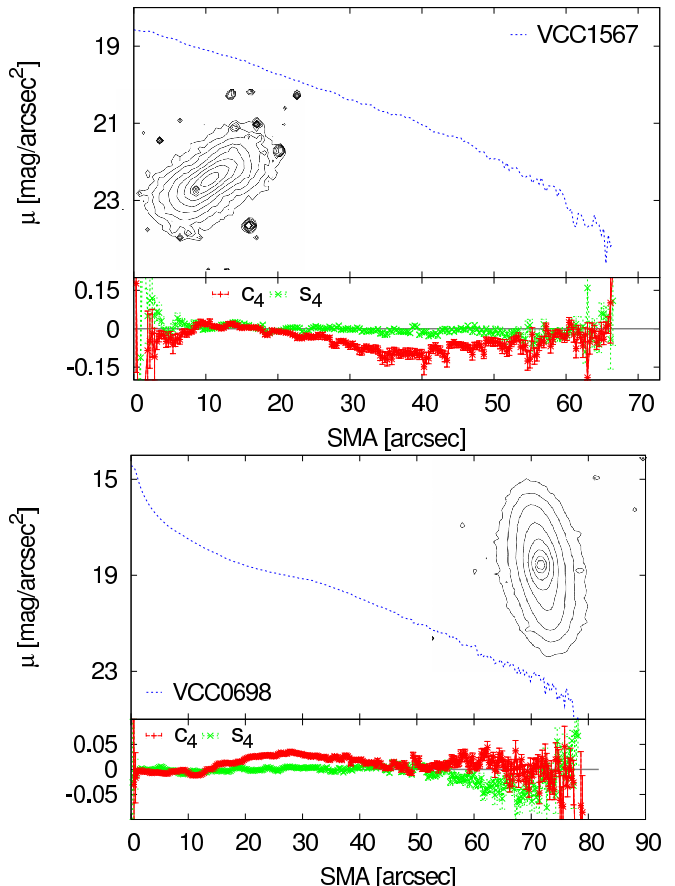


**Figure 3.** Illustration of boxy- and diskiness. One example of a boxy galaxy (VCC1567, upper panel) and a diskier galaxy (VCC0698, lower panel) is shown. For both the light profiles (blue) are plotted together with the profiles of  $c_4$  (red) and  $s_4$  (green). The insets show the isophotes, the outermost isophote correspond to  $a \approx 44$  and  $a \approx 51$  arcsecs, respectively. The two profiles are very consistent with those obtained in a similar manner with SDSS data. The median values in the inner part ( $1''.25 < a < r_e$ ), outer part ( $r_e < a < 2r_e$ ), and for the whole galaxy are  $\bar{c}_4 = -0.0158, -0.0794, -0.0454$  and  $\bar{c}_4 = -0.0039, 0.0270, 0.0129$ , respectively, for VCC1567 and VCC0698. VCC1567 has three features with integrated values  $\bar{c}_4/r_e = -0.028, 0.003, -0.088$ , VCC0698 has two  $\bar{c}_4/r_e = -0.004, 0.035$ .

### 3.3. Isophotal shape

IRAF/ellipse fits deviations of the isophotes from an elliptical shape using a Fourier series:

$$I(\theta) = I_0 + \sum_{n=1}^{\infty} (C_n \cos n\theta + S_n \sin n\theta). \quad (3)$$

Since the nomenclature in IRAF and the literature is not uniform, we adapt the notation of [Toloba et al. \(2011\)](#) with  $C_n$  and  $S_n$  for the cosine and sine terms (in IRAF:  $B_n$  and  $A_n$ , respectively). The coefficients are normalized by the length of the SMA and the gradient of the profile,  $c_n = C_n/(a \cdot dI/dr)$  and  $s_n = S_n/(a \cdot dI/dr)$ , to quantify the distance of the isophote to the ellipse relative to its size. The most interesting coefficient is  $c_4$  ([Carter 1978](#)), which is the parameter describing the boxiness ( $c_4 < 0$ ) or diskiness ( $c_4 > 0$ ) of the isophote (Fig. 3). In the following the parameter is referred to as boxiness.

The sine coefficient of the same order describes deviations of the isophote, not along and between the major and minor axis, but rotated by  $22.5^\circ$ . For a pure boxy or diskier shape

this coefficient should remain close to  $s_4 \approx 0$ . The isophote can also have a more complex deviation from an elliptical shape, in which case the measurement can be less confidently attributed to a boxy or disky shape. For most of the galaxies the profiles are noisier than the examples in Fig. 3: in some cases the values scatter for large parts of the profile around 0, consistent with the errors associated with the measurements.

Moreover, some galaxies have both boxy and disky sections. Therefore, boxiness values are assigned to the galaxies in two ways: (a) the median value  $\tilde{c}_4$  for the inner ( $1''.25 < a < r_e$ ) and outer ( $r_e < a < 2r_e$ ) part of the profile, and (b) integrated values  $\tilde{c}_4$  over boxy or disky features in the  $c_4$  profiles:

$$\tilde{c}_4 = \int_{\text{feature}} c_4(r) dr. \quad (4)$$

These integrals have the dimension of an angular size and are normalized to the angular size of the galaxy ( $r_e$ ) in the later figures. The features are found by searching for sections in the profile where the sign of  $c_4$  does not change for at least three consecutive measurements,  $|c_4|$  is larger than its error as given by IRAF/ellipse, and larger than  $|s_4|$ . We calculate the formal error of  $\tilde{c}_4$  as the square root of the quadratic sum of the single measurement, multiplied by the bin width of the numerical integration. This way multiple disky or boxy values can be assigned to different regions in a single galaxy.

### 3.4. Two-dimensional Decompositions

Traditionally one-dimensional profile decompositions are used in structure analysis both for bright and dwarf galaxies. Although one-dimensional azimuthally averaged profiles themselves are not very sensitive for detecting non-axisymmetric structures in galaxies (§3.4.2, [Byun & Freeman 1995](#); [de Jong et al. 2004](#); [Laurikainen et al. 2005](#); [Noordermeer & van der Hulst 2007](#); [Weinzirl et al. 2009](#)), combined with inspection of the radial profiles of the ellipticities and position angles, they have been successfully used to identify multiple components, including those of the elliptical galaxies.

However, in this study we have chosen the multi-component two-dimensional decomposition approach. That enables functional fitting, not only of bulges and disks, but also of the non-axisymmetric structures like bars, using the complete information of the two-dimensional light distributions. Above all, this allows us to derive quantitative parameters for the different structure components, in a similar manner as has been obtained for the bulges and disks for bright S0s and spirals. A parametric comparison of the structures of the sample galaxies with those obtained for the bright galaxies is one of the goals of this paper.

It has been shown for bright galaxies by [Laurikainen et al. \(2006\)](#) that the flux of the non-axisymmetric structure can be erroneously mixed with the flux of the bulge if not fitted separately. This is the case both with the 1D and 2D decomposition approaches. For the dwarf galaxies this problem was pointed out by [McDonald et al. \(2011\)](#), who speculated that omitting the non-axisymmetric structures some light might erroneously be attributed to some other, mostly the inner component. They estimate the effect on the parameters of the other components to be 10% to 20%. Since in dwarf galaxies the multiple components are expected to be much more subtle than in the bright galaxies, they might be even more difficult to see in the azimuthally averaged one-dimensional profiles. As an example of the strength of the two-dimensional ap-

proach VCC0940 is shown in Figs. 4 & 5. Although the bar is hardly visible in the azimuthally averaged profile it is clearly manifested in the two-dimensional profile, in which all the pixels of the image are shown (Fig. 4). In the two-dimensional decomposition approach these pixels can be functionally fitted.

Our two-dimensional multicomponent decomposition approach was introduced in [Janz et al. \(2012\)](#), but will be described in some detail here. The fitting is carried out with GALFIT 3.0 ([Peng et al. 2010](#)). GALFIT minimizes the  $\chi^2$  to find the optimal solution for a given model. It uses an algorithm that tries to keep the probability of falling into a local minimum of  $\chi^2$  in the parameter space small. For the simple models the starting values are chosen based on the photometric parameters of the whole galaxies, while for the two-component models they are based on reasonable assumptions and improved if needed. It is assumed that the ellipticity and position angle of each individual component are constant with radius. In the case of further features such as bars (see below) the component is first identified in the profile or in the residual image and starting values are then chosen accordingly. For calculating the  $\chi^2$ s we provide GALFIT with the  $\sigma$ -images (§2.3). We use masks for fore- and background sources and assume a Gaussian PSF with the measured FWHM. During the fitting process the model is convolved with the PSF image.

The decompositions of highly inclined galaxies are not considered reliable, unless the galaxy is seen exactly edge-on ([Laurikainen et al. 2010](#); [Kormendy & Bender 2012](#)). Thus we limit this analysis to galaxies with axis ratios larger than the corresponding value of a flat disk inclined by  $65^\circ$ ,  $b/a > \cos 65^\circ$ , which excludes 14 galaxies from this analysis. Furthermore, for 8 galaxies we did not find reliable decompositions and therefore they are excluded as well.<sup>8</sup>

#### 3.4.1. The model functions

The following functions were used for the profiles:

- $\delta$ -function for point-like sources.
- Exponential function:

$$I(r) = I_0 \exp\left(-\frac{r}{h}\right), \quad (5)$$

with the central intensity  $I_0$ , the scale length  $h$ , and  $r_e = 1.678h$ .

- Sérsic function ([Sérsic 1963](#)):

$$I(r) = I_e \exp\left(-b_n \left[\left(\frac{r}{r_e}\right)^{1/n} - 1\right]\right), \quad (6)$$

with the intensity  $I_e$  at  $r_e$ , the Sérsic index  $n$  for the steepness of the profile ( $n = 1$  and  $n = 4$  corresponding

<sup>8</sup> Note that, that the excluded galaxies are not likely to be simple galaxies, so that their inclusion would lower the fraction of one-component galaxies. VCC0575 has possibly even more than two components; VCC0698 is probably highly inclined; VCC1178 and VCC1745 likely have lenses, which are not well-fitted with Ferrers functions; VCC1196 probably has a bar and some residual structures that might remind of shells; VCC1567 is probably seen edge-on and is extremely boxy (see Fig. 3, the values come even close to the galaxy studied by [Graham et al. \(2012\)](#)); VCC1297 has a small angular size, the profile looks overall like a Sérsic profile, but there is a strong structure in the residual image, [Ferrarese et al. \(2006\)](#) report an increasing ellipticity to the galaxy center that may be related to the double nucleus identified by [Lauer et al. \(1996\)](#).



to an exponential and de Vaucouleurs profile, respectively), and the  $b_n$  parameter that depends on  $n$ . The dependency can be expressed by gamma functions (Ciotti 1991) and approximated by  $b_n = 1.992n - 0.3271$  for  $0.5 < n < 10$  (Capaccioli 1989). The purpose of  $b_n$  is to ensure that  $I_e$  is the intensity at the half-light radius.

- Modified Ferrers function (Binney & Tremaine 1987):

$$I(r) = I_0 [1 - (r/r_{\text{out}})^{2-\beta}]^\alpha. \quad (7)$$

This function features a nearly flat core, with a central slope of  $\beta$ , and a truncation at  $r_{\text{out}}$  with the sharpness  $\alpha$ . Beyond  $r > r_{\text{out}}$  the profile is not defined and the function has a value of 0. The flat core and sharp cutoff makes it especially useful for fitting bars.

Except for the  $\delta$ -function, the position angle and axis ratio are two additional fitting parameters. Each component is constrained to have elliptical isophotes and constant position angle and ellipticity. In the following we will use the term simple model for a model that uses a single Sérsic function or a combination of a Sérsic function and a  $\delta$ -function for the nucleus.

### 3.4.2. Fitting procedure

First the following models are fitted to the galaxies, listed in the order of increasing complexity:

- a one-component Sérsic model,
- a combination of a Sérsic model and a point-source, and
- a two-component model with the inner component fitted by a Sérsic function and the outer component with an exponential function.

Although typically the outer component is fitted with an exponential, this condition was relaxed in cases, in which the outer profile is obviously not exponential. In such cases a Sérsic function is used with the Sérsic parameter  $n$  as a free fitting parameter. The position angle and the axis ratio of the outer component in the latter model are fixed to an average value of the outermost isophotes.

These basic models are then compared and visually inspected using GALFIDL.<sup>9</sup> Most important for our evaluation were the residual images after subtracting the model, the profiles of the two-dimensional light distributions of the observation, the whole model, and the models for the different components. By two-dimensional we mean that the surface brightnesses of all pixels are shown as a function of their angular distance to the galaxy center (Laurikainen et al. 2005; Gadotti 2008). The upper panel of Fig. 4 illustrates the information contained in such profiles. For a perfectly round component all the pixels at a certain distance from the center will have the same surface brightness, while for increasing apparent flattening of the component the range of the surface brightness at this distance will also increase, thus making the wedge-shaped profile. In Fig. 5, displaying the same galaxy, but showing the azimuthally averaged one-dimensional profiles instead, the bar is hard to detect, both in the image and in the azimuthally averaged profile. The deviation of the model from the observation in the azimuthally averaged profile is

<sup>9</sup> H. Salo, <http://cc.oulu.fi/~hsalo/galfidl.html>.

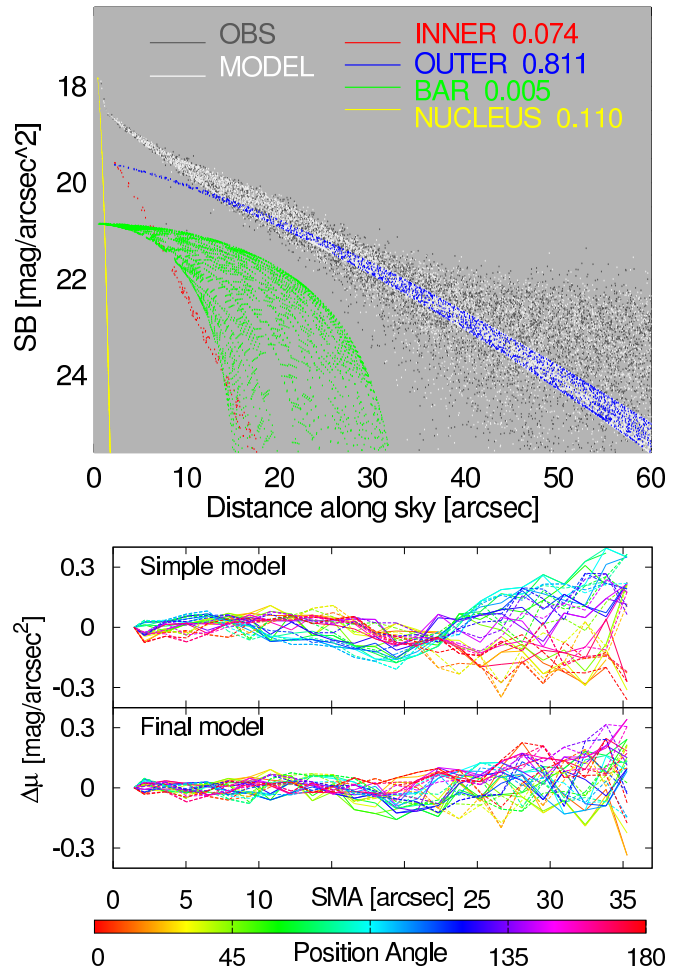


**Figure 4.** Upper panel: Profile of VCC0940 and its final model displaying all pixels (an image of the galaxy is found in Fig. 5). The total model (white) is plotted twice: without noise and including noise according to the image. The model without noise is not a line due to the apparent flattening of the light distribution. It is visible as an area filled with white points. At distances larger than  $30''$  the model is dominated by the outer component and thus blue points showing the disk component are plotted on top of the complete model. The model including the noise has a broader distribution at larger radii, due to an approximately constant noise, displayed on the logarithmic magnitude scale. These white points spread around the dark points of the observed pixels. Colors indicate different components; the number after the label indicates the fractional contribution to the total flux. Middle and lower panel: residual profiles along different position angles (displayed with different colors, see colorbar above the panels, solid and dashed lines show the profiles in sectors rotated by  $180^\circ$ ) for the simple and final model; plotted is the difference of surface brightnesses  $\Delta\mu$ .

less than 10% (cf. Aguerri et al. 2005). However, in the residual image the bar is clearly visible. Moreover, at about 10–20 arcsecs the bar thickens the pixel distribution in the two-dimensional profile because of the ellipticity maximum (Fig. 4, upper panel; generally, the distribution becomes thicker at larger radii due to the nearly constant noise and the logarithmic scale). Notice that in Fig. 5 the observations are measured in the same apertures as the models, in order to allow a direct comparison of the profiles and not to mix it with effects of differences in the isophotes. The observed profile measured along the simple model isophotes is equivalent with determining the profile with fixed ellipticity and position angle. Along the final model isophotes the profile comes very close to a profile determined along the isophotes of the observation.

That the overall shape of the profile is not well represented by a simple model is manifested as a clear structure in the residual profile (Fig. 4, middle panel). In addition to the overall behavior, the residual profiles in sectors at different position angles deviate systematically from each other. This behavior is due to the non-axisymmetric bar. All line up nicely in the final model (lower panel), where the thickened pixel distribution in the bar region (upper panel) is accounted for. Additional guidance for the model evaluation are the profiles of the orientation parameters (Fig. 5). In less clear cases we flag the decomposition as “uncertain” and in doubtful cases we opted for the simpler model.

In those cases where none of the previous models is satisfactory, we try one of the following changes:

- vary the starting values (since GALFIT can end up in a local minimum of  $\chi^2$  in the parameter space when degeneracies occur with the increasing number of components). Or, in a few cases,
- use an outer component with Sérsic  $n < 1$  (instead of an exponential), or
- use different centers for the different components.

A typical profile type turns out to be the one with a “down-bending” part, that is, a component with a flat inner profile and a steep outer decline causing an edge, similar to the profile of a bar, but with a round shape. Since the axis ratio is close to unity this can be seen as a nearly round extended excess of light in the residual image, with an insufficient modeling of the central flux. This kind of component we call “lens” (see §4.1, and also [Binggeli & Cameron 1991](#)) in analogy to lenses frequently detected in bright early-type disk galaxies, which have similar profiles ([Kormendy 1979](#); [Laurikainen et al. 2013](#)). We model it with a Ferrers function, in a similar manner as done for the bright galaxies in our comparison samples. Typically these components replaced the inner component, and only in a few cases we add it to the two-component model or use it in combination with an inner component. Therefore, the galaxies with lenses may also be thought of as special cases of two component galaxies.

Finally, if a bar is revealed in the model subtracted images, we fit the bar with an additional Ferrers function.<sup>10</sup> The complete set of models with their residuals, light profiles, and profiles of the orientation parameters is shown for one galaxy, VCC0940, in Fig. 5.<sup>11</sup> In principle a small error in the sky subtraction can alter the profile at low surface brightnesses enough to change the shape of the profile, i.e. mimic a complex structure. We estimate the potential influence of large scale variations by the standard deviations of mean sky values, measured in small boxes on the image. When evaluating the decompositions, we include new components only if the deviations of the profile shape exceed the uncertainties due to large scale background variations (the uncertainty is indicated as blue shaded areas in the profiles of Fig. 5).

Furthermore, the detection of components, especially in the outer parts, obviously depends on the image depth. The integration time for an individual galaxy was chosen to reach a certain  $S/N$  per pixel at  $2r_e$ , so that the galaxies with lower

surface brightnesses were observed for longer times. Therefore, we do not expect to have missed components of similar relative flux and extent at the faint end of the sample. The decomposition for a single galaxy might be different if yet deeper images were available. For example, in VCC0170 the outer part, with different orientation, is not visible in shallower images (see illustration in Fig. 1 of [Janz et al. 2012](#)). For VCC0490 we did a two component decomposition, with the outer component having a Sérsic  $n < 1$ . However, on a very deep optical (white filter) WFI image ([Lisker, Brunngräber, & Grebel 2009](#)) this part looks more like a bump in the profile on top of an even more extended component.

### 3.4.3. Quantification of fit quality

Although the model selection in the decompositions is done in a visual manner, we seek to quantify the quality of the fits, and to quantitatively justify that for many galaxies in our sample a non-simple model is indeed needed. We follow the approach of [Hoyos et al. \(2011\)](#), who used the following two indices. The residual flux fraction (RFF) (introduced by [Blakeslee et al. 2006](#)) is defined as

$$\text{RFF} = \frac{\sum (|Res| - 0.8 * \sigma)}{\sum Flux}, \quad (8)$$

where  $|Res|$  is the absolute value of the residual flux,  $\sigma$  is the  $\sigma$ -image, and  $Flux$  is the observed flux. The summation is carried out over a chosen aperture. The excess variance index (EVI) is

$$\text{EVI} = \frac{1}{3} \times \left( \frac{\sigma_R^2}{\langle \sigma^2 \rangle} - 1 \right), \quad (9)$$

where  $\sigma_R^2$  is the mean square of the residual and  $\langle \sigma^2 \rangle$  the mean value of the  $\sigma$ -image squared, both again measured in a chosen aperture. The factor 1/3 was chosen according to their data based on a visual examination. The expectation values of both indices for a perfect model are zero. As [Hoyos et al.](#) point out, RFF is close to zero for an extended low surface brightness galaxy even for cases where in the model the inner part shows a significant deviation from the observation. Therefore, they introduced the EVI index, which is sensitive to the variations in the bright inner part of the galaxy. Fig. 6 compares RFF and EVI for our simple models, using apertures containing the outer isophotes of the galaxies. More than 85% of the objects with  $\text{RFF} > 0.013$  are complex galaxies, increasing to 95% with the additional criterion of  $\text{EVI} > 0.13$ . The one-component galaxies have on average smaller values of RFF and EVI, and generally at least one of the indices is rather small. In the right panel of Fig. 6 the improvements (which are less dependent on the noise estimate) in the final models are shown:  $> 95\%$  of complex galaxies show an improvement, i.e. a decrease, of both RFF and EVI from the simple to the final model.

In addition we also evaluated the behavior of the reduced  $\chi^2$  and of the tessellated excess residuals, as detailed in Appendix B. Both quantifications support our visual choices for the necessity of complex models. However, we want to stress at this point that we consciously chose to make the decision about the final decomposition in a non-automated way.

<sup>10</sup> In two galaxies with a lens we find a small bar. These are not fitted, since we want to avoid to have overly complex models.

<sup>11</sup> In a few cases, also outer components fitted by Sérsic functions with  $n > 1$  were used, see Table 5.



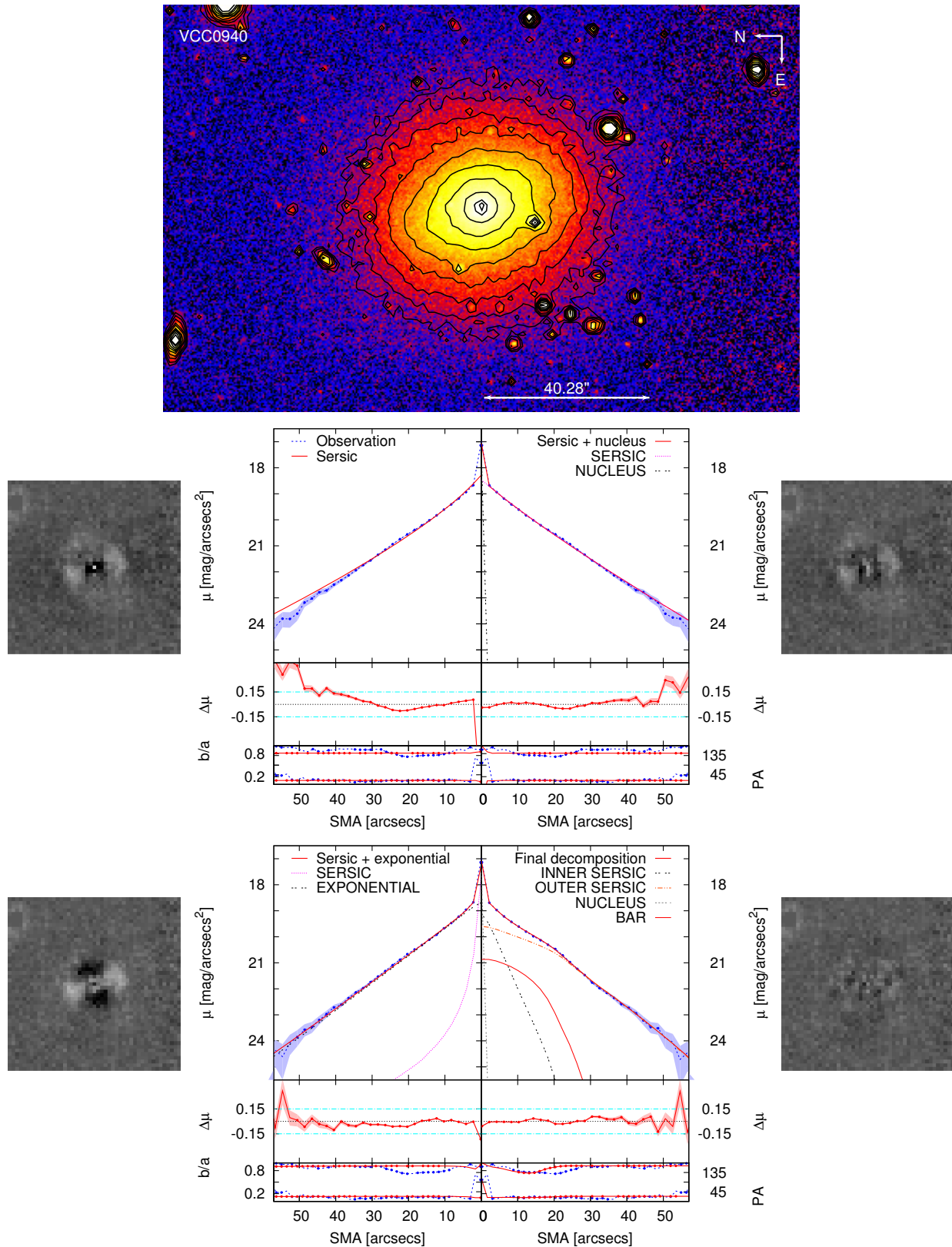


**Figure 5.** Top panel: image of VCC0940. The other panels illustrate the visual model evaluation in the fitting procedure: residuals, azimuthally averaged light profiles, and orientation parameter profiles. The simple models (one Sérsic component and Sérsic+nucleus) are shown in the middle panels. The bottom row displays the two-component model and the final model with a bar. The observations are measured in the same apertures as the models, using the model isophotes, which can lead to slight variations in the observed profile displays between the panels. The residual images display  $\pm 3\sigma$  on a linear scale, and are re-binned for the small scale display. The width of the residual stamps is about half an arcminute. In the bottom part of the profile panels the axis ratio  $b/a$  (*upper lines*) and the position angle (PA, *lower lines*) are shown. The shaded regions and error bars in the profiles and residual profiles illustrate the estimate of large scale background variations and the surface brightness uncertainties given by IRAF/ellipse, respectively. A similar presentation of models can be accessed for all galaxies in our sample as online-only figures and via <http://www.smakced.net/data.html>.

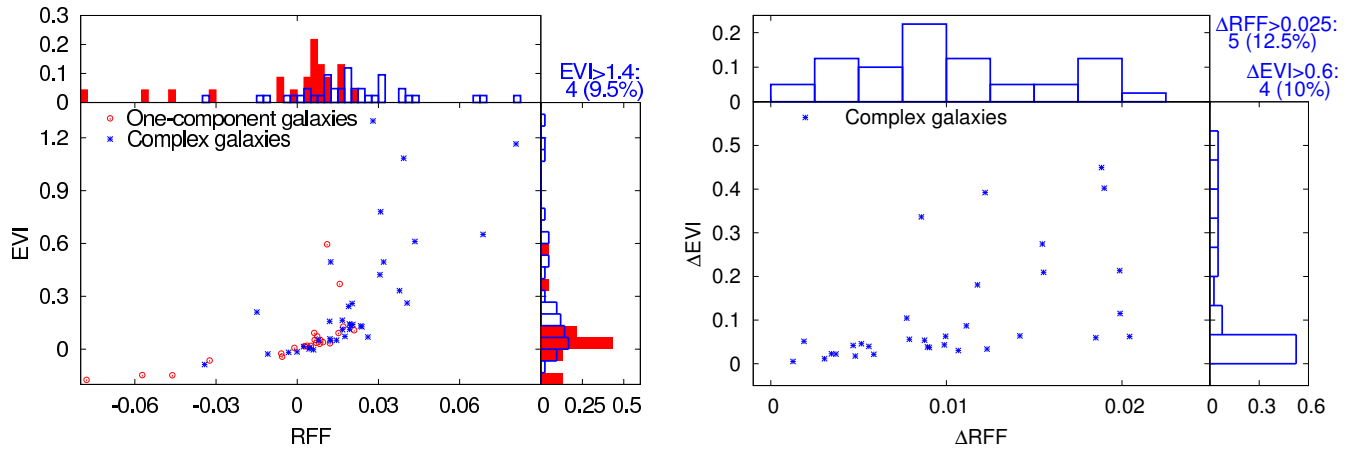


**Figure 6.** RFF and EVI values for all galaxies when using a simple model (*left panel*; red – one-component galaxies, blue – complex galaxies), and the improvement from the simple to the final model for two-component galaxies, galaxies with lens, and barred galaxies (*right panel*). For both indices is  $\Delta\text{INDEX} = \text{INDEX}_{\text{simple}} - \text{INDEX}_{\text{final}}$ . The small panels show histograms of distributions on the corresponding axis.

## 4. RESULTS

## 4.1. Structural types

Following Janz et al. (2012) we group the galaxies into four structural types, based on the decompositions: (1) one-component galaxies that satisfy a simple model (with or without a nucleus, first two models in §3.4.2 and Fig. 5), (2) two-component galaxies that have an inner and outer component (with or without an additional nucleus), (3) galaxies with a lens component, and (4) barred galaxies (Fig. 7; more examples in Janz et al. 2012, their Fig. 2).

The concept of barred galaxies is clear: these galaxies have two or in some cases three components (not counting the nucleus), one of them being a bar. The galaxies with a lens can be considered as a special group of two-component galaxies. In the surface brightness profiles the lens-like component is fairly flat and has a rather steep truncation (Fig. 7, panel 3). While this profile shape is quite similar to the profile of a bar (Fig. 7, lower panels), the lens is not strongly elongated. As its shape clearly differs from that of an inner component with  $n > 1$ , galaxies with such a characteristic bump in the profile are considered as a separate group.

Most importantly, not all galaxies follow a simple model. In fact, a large fraction falls into one of the three complex groups.<sup>12</sup>

We briefly summarize the findings already presented in Janz et al. (2012) and provide an updated Table of the frequencies of structural types, with observations for 20 new galaxies (Table 3 = Table 4). Janz et al. found the fraction of one-component galaxies to be close to a quarter. The fraction is a strong function of galaxy brightness and increased with the observations of fainter galaxies. This is not expected to be a simple selection effect, since the fainter galaxies had longer integration times by design of the observations. With the updated sample a Kolmogorov-Smirnov (KS) test gives a statistically significant difference of the brightness distributions of simple and complex galaxies ( $p < 1\%$ ). The updated fraction of a third for the complete sample is still remarkably low. Even if we exclude galaxies classified as E or S0 as well as count less certain two-component galaxies as one-component galaxies the fraction is only 44%. The fraction is highest among the early-type dwarf galaxy subclasses where no disk feature or central star formation have been detected (Lisker et al. 2006b,a). The bar fraction drops towards fainter galaxies. The updated fraction is slightly smaller than in Janz et al. (2012) due to the increased sampling of fainter galaxies. With two small bars in galaxies with lenses, which were not fitted and therefore do not appear in the Table, the fraction is 16%. If only certain bars and galaxies with a dE or dS0 classification are considered, the bar fraction is 10%. The same is true for the fraction of galaxies with lenses (14% and 7%, respectively).

## 4.2. Profile shapes

The overall profile shapes of the galaxies in our sample are not much steeper than exponentials. They follow the known relation of Sérsic  $n$  and galaxy brightness (e.g. Caon, Capaccioli, & D’Onofrio 1993; Caon et al. 1994). However, we show with our two-dimensional multi-component decomposi-

<sup>12</sup> With a different type of analysis, several of our two-component galaxies may be modeled as a single component with varying position angle and ellipticity, which is the case in the ACS VCS (Advanced Camera for Surveys Virgo Cluster Survey; Ferrarese et al. 2006; L. Ferrarese, priv. comm.). This does, however, not touch the fact that they show a complex light distribution.

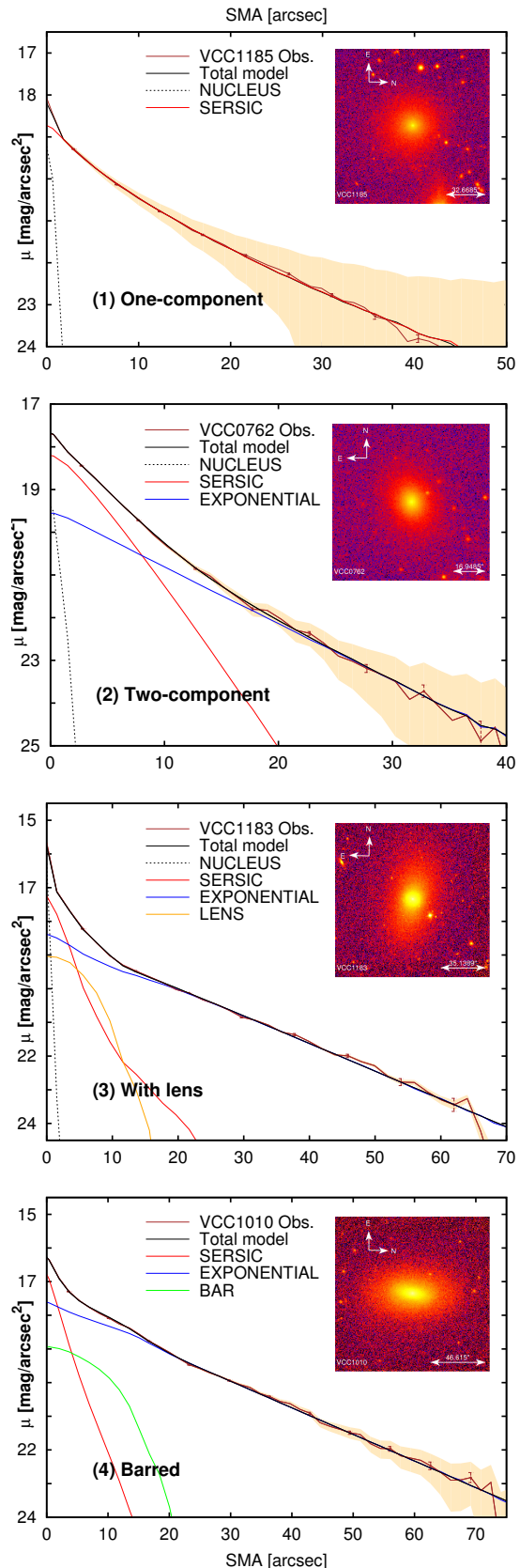


**Figure 7.** Representative galaxies for the structural groups (§4.1), from top to bottom: VCC1185 – single component, VCC0762 – two components, VCC1183 – with lens, and VCC1010 – barred. The shaded areas display the maximal systematic error caused by large-scale background variations and the error bars display the surface brightness uncertainties as measured by IRAF/ellipse.



**Table 4**  
Frequencies of structural types

Group	1		2		3		4		Total analyzed
	One-component		Two-component		With lens		Barred		
All	32	32% ± 4%	39	(8) 39% ± 4%	14	(5) 14% ± 3%	14	(5) 14% ± 3%	99
$-19 < M_r < -18$	1	6% ± 5%	8	(0) 47% ± 12%	4	(3) 24% ± 10%	4	(0) 24% ± 10%	17
$-18 < M_r < -17$	16	30% ± 6%	23	(5) 43% ± 6%	6	(0) 11% ± 4%	8	(5) 15% ± 4%	53
$-17 < M_r < -16$	15	52% ± 9%	8	(3) 28% ± 8%	4	(2) 14% ± 6%	2	(0) 7% ± 4%	29
dE(all)	31	37% ± 5%	33	(7) 39% ± 5%	9	(3) 11% ± 3%	11	(5) 13% ± 3%	84
dE(N)	20	49% ± 7%	11	(2) 27% ± 6%	7	(2) 17% ± 5%	3	(2) 7% ± 3%	41
dE(nN)	3	38% ± 17%	5	(1) 63% ± 17%	0	(0) 0%	0	(0) 0%	8
dE(di)	4	15% ± 7%	11	(2) 42% ± 9%	2	(1) 8% ± 5%	9	(3) 35% ± 9%	26
dE(bc)	4	33% ± 13%	8	(2) 67% ± 13%	0	(0) 0%	0	(0) 0%	12
E&S0	1	7% ± 6%	6	(1) 40% ± 12%	5	(2) 33% ± 12%	3	(0) 20% ± 10%	15
$D_{M87} < 1.5^\circ$	6	22% ± 7%	9	(3) 33% ± 9%	5	(2) 19% ± 7%	7	(3) 26% ± 8%	27
$1.5^\circ \leq D_{M87} < 4^\circ$	16	36% ± 7%	18	(4) 41% ± 7%	6	(2) 14% ± 5%	4	(1) 9% ± 4%	44
$D_{M87} \geq 4^\circ$	10	36% ± 9%	12	(1) 43% ± 9%	3	(1) 11% ± 5%	3	(1) 11% ± 5%	28

**Note.** — We list numbers and fractions of galaxies in each group binned over the brightness,  $dE$  subclass (dE(N) – nucleated, dE(nN) – no nucleus, dE(bc) – blue core, dE(di) – disk features; Lisker et al. 2006a,b, 2007), and angular distance to M87 ( $1^\circ = 0.284$  Mpc). The total sum in the subclass binning is larger than the total number of galaxies, since  $dEs$  can belong to multiple subclasses. The less certain cases in each group, shown in parenthesis, are included in the numbers and fractions. The uncertainties of the percentages are calculated according to the Poisson statistics. Additionally two small bars were visually identified but not fitted and are therefore not counted in this Table.

tion analysis that this view is oversimplified. Instead of simple Sérsic profiles becoming steeper with increasing galaxy brightness, the trend of the profile shape with galaxy brightness can be, at least partly, attributed to the more frequent multi-component structures in the brighter galaxies (Fig. 8, for more quantitative analysis see Appendix C).

In Fig. 8 we show all the profiles together, scaled to a common radius and surface brightness. While the choice of a fixed exponential shape for most outer components (see §3.4.2) could in principle influence the resulting parameter space, the figure shows that the assumption is justified for the vast majority of galaxies (see also e.g. Binggeli & Cameron 1991). We point out that also the inner component in the complex models is close to an exponential profile (most of the inner components have  $n < 1.2$ ). Bars and lenses have similar extents.

The profiles of the one-component or complex galaxies do not show systematic differences with the presence of a nucleus. We note that in Fig. 8 the nucleus is actually hard to see, since the plotted radial range of the profiles is much larger than the PSF. In some of the profiles of the one-component galaxies it is visible as a peak at a few central pixels. However, for the complex galaxies the profiles are scaled to even larger radii. For those, the inner excess of light is due to the inner component and not due to the nucleus.

### 4.3. Morphological parameters

For the early-type galaxies the Kormendy relation (Kormendy 1977) and its relatives, with interchanging either the mean effective surface brightness or the effective radius with brightness, are commonly studied. In Fig. 9 the obtained non-parametric photometric quantities are used to construct the brightness versus effective radius relation for the galaxies in our sample, whereas the Kormendy relation is shown in Appendix D.

For comparison we add Virgo cluster galaxies of different morphological types from the 2MASS extended source catalog, using the extrapolated total magnitudes. 2MASS is not very deep,<sup>13</sup> therefore the photometry for faint galaxies

should not be trusted: it misses a substantial fraction of the light so that both the radius and brightness are underestimated. Furthermore, the extended source catalog does not include all VCC galaxies, though the coverage of the Virgo cluster is complete. A comparison of the photometry in this study and the 2MASS measurements for galaxies common to both samples shows that the 2MASS photometry is consistent for the galaxies brighter than  $M_H < -20$  mag (lower panels in Fig. 9), and therefore considered robust for bright galaxies.

Furthermore, the additional comparison of the magnitudes measured by McDonald et al. (2011) shows consistently that 2MASS misses some of the flux for the fainter galaxies. The faintest galaxies are missing from the 2MASS extended source catalog. For a further comparison to the study of McDonald et al. see Appendix E. When using 2MASS  $10''$  aperture colors to transform the  $K$ -band magnitudes of Toloba et al. (2012, MAGPOP survey) into  $H$ -band, the median difference for the 17 galaxies in common is only 0.03 mag, with a semi-interquartile range of 0.12 mag.<sup>14</sup>

Fig. 9 shows that there is some overlap of the early-type dwarfs with the spiral galaxies (panel *b*), and that they apparently form a more simple continuous relation than with the bright elliptical galaxies that seem to fall on a different relation (panel *a*; see also Boselli et al. 2008b; Kormendy & Bender 2012; Toloba et al. 2012).

### 4.4. Flattening distributions

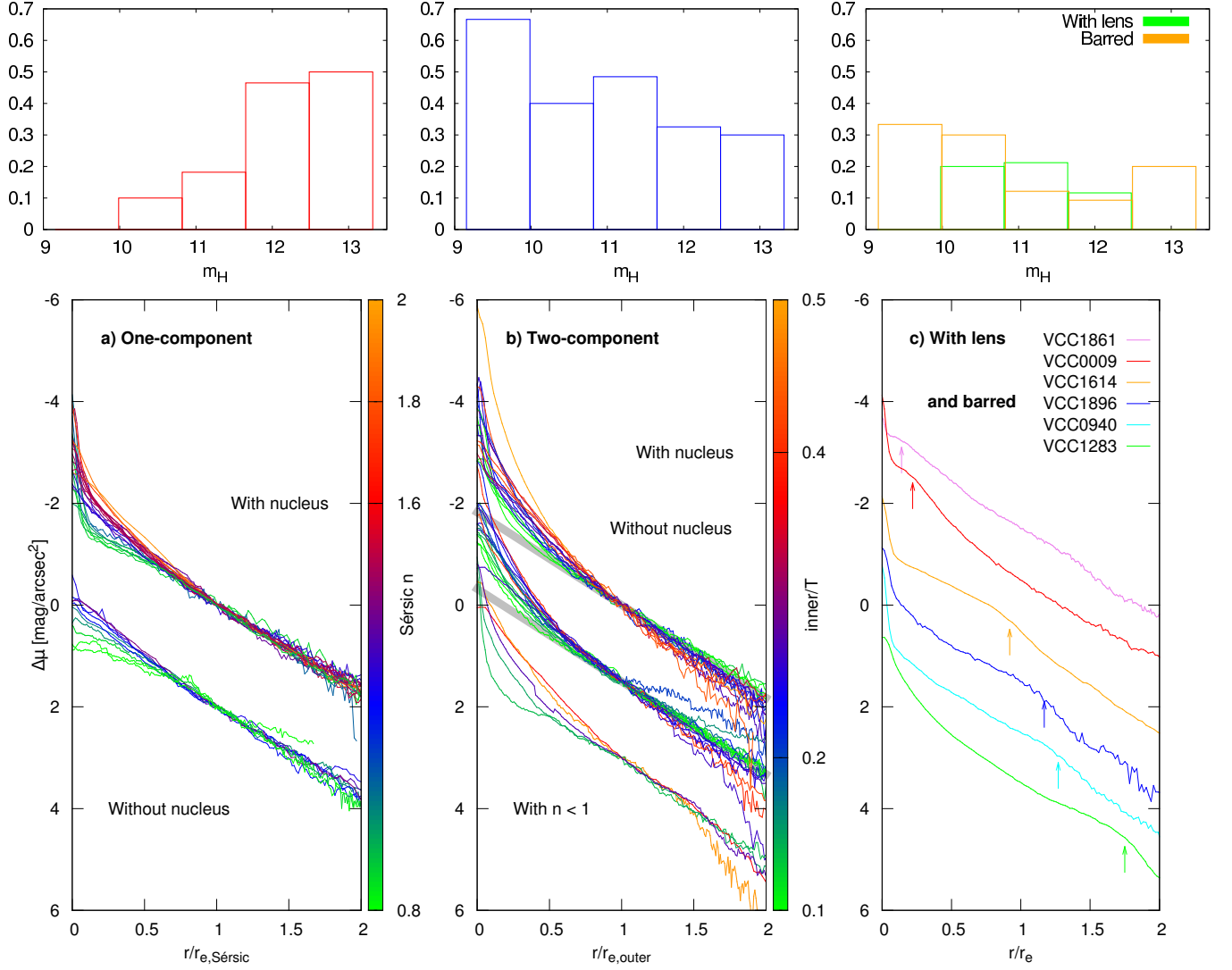
The flattening distributions of the components are of interest, since they are expected to be different for different distributions of intrinsic shapes (see e.g. Lisker et al. 2007).

Fig. 10 shows the distributions of the axis ratios of the one-component galaxies, and inner and outer components of complex galaxies. Our inclination limit falls into the second bin ( $b/a = 0.42$ ). The flattening distributions for the inner and outer components are very similar, so that they should have similar intrinsic shapes. The one-component galaxies may have a double peaked distribution, with some contribution of

ison of our data for one galaxy was shown in Janz et al. (2012), their Fig. 1.

<sup>14</sup> Note that we used the correct photometric values of Toloba et al. (2012) according to the erratum Toloba et al. (2013, in press).

<sup>13</sup> Note that 2MASS is much shallower than UKIDSS, to which a compar-



**Figure 8.** The top panels show from left to right the fractions of the one-component galaxies, two-component galaxies, and galaxies with lenses and bars in bins of galaxy brightness of 0.5 mag. The bottom panels display the azimuthally averaged profiles of the galaxies in the one-component and two-components groups, and a few examples of the groups of galaxies with lenses and barred galaxies. The radii are normalized to the effective radius of the Sérsic function (a), the outer component (b), and the whole galaxy’s half-light radius (c). The y-axis is normalized to the surface brightness at that radius, and for different galaxy groups or galaxies arbitrary offsets are applied. In panels a & b the Sérsic index ( $n$ ) and the ratio of flux in the inner component to that of the whole galaxy ( $inner/T$ ), respectively, are coded in color. In panel b the profiles are grouped from top to bottom: galaxies with nucleus, without nucleus, and galaxies with an outer Sérsic component with  $n < 1$ . The gray lines in the middle panel display an exponential profile. In the right panel examples for profiles of galaxies with lenses and bars are shown, from top to bottom the first three galaxies have lenses, while the last three have bars. The arrows indicate the radius where the lens or bar contributes most significantly to the light.

galaxies that may be as round as the bright early types. However, the small numbers make it impossible to firmly state that they have a flattening distribution different from the other early-type dwarfs. A KS-test cannot reject the null-hypothesis that both the one-component and complex galaxies are drawn from the same distribution.

For comparison we compiled axis ratios of other galaxy types from the SDSS (DR8, Aihara et al. 2011). We use the galaxies in RC3 (de Vaucouleurs et al. 1991) with measured redshifts (in SDSS) below  $z < 0.1$ . The axis ratio is calculated from the adaptive second moments  $E1$  and  $E2$ , measured by the SDSS pipeline in the  $r$ -band, with

$$b/a = \left( \frac{1-e}{1+e} \right)^{1/2}, \quad (10)$$

where  $e = \sqrt{E1^2 + E2^2}$  (Hirata & Seljak 2003). We do not correct for seeing effects, since the galaxies in RC3 are large compared to the SDSS seeing. The distributions of axis ratios of the early-type dwarfs and their inner and outer components is closer to that of spirals than to that of early-type galaxies, consistent with the findings of Binggeli & Popescu (1995). Fisher & Drory (2008) showed that in bright galaxies classical bulges are round, while pseudo-bulges have flattenings similar to the outer disk.

#### 4.5. Boxiness

In Fig. 11 we show the median values of the boxiness parameter,  $\bar{c}_4$ , at radii smaller than the effective radius,  $1''.25 < a < r_e$ , and between one and two effective radii,  $r_e < a <$

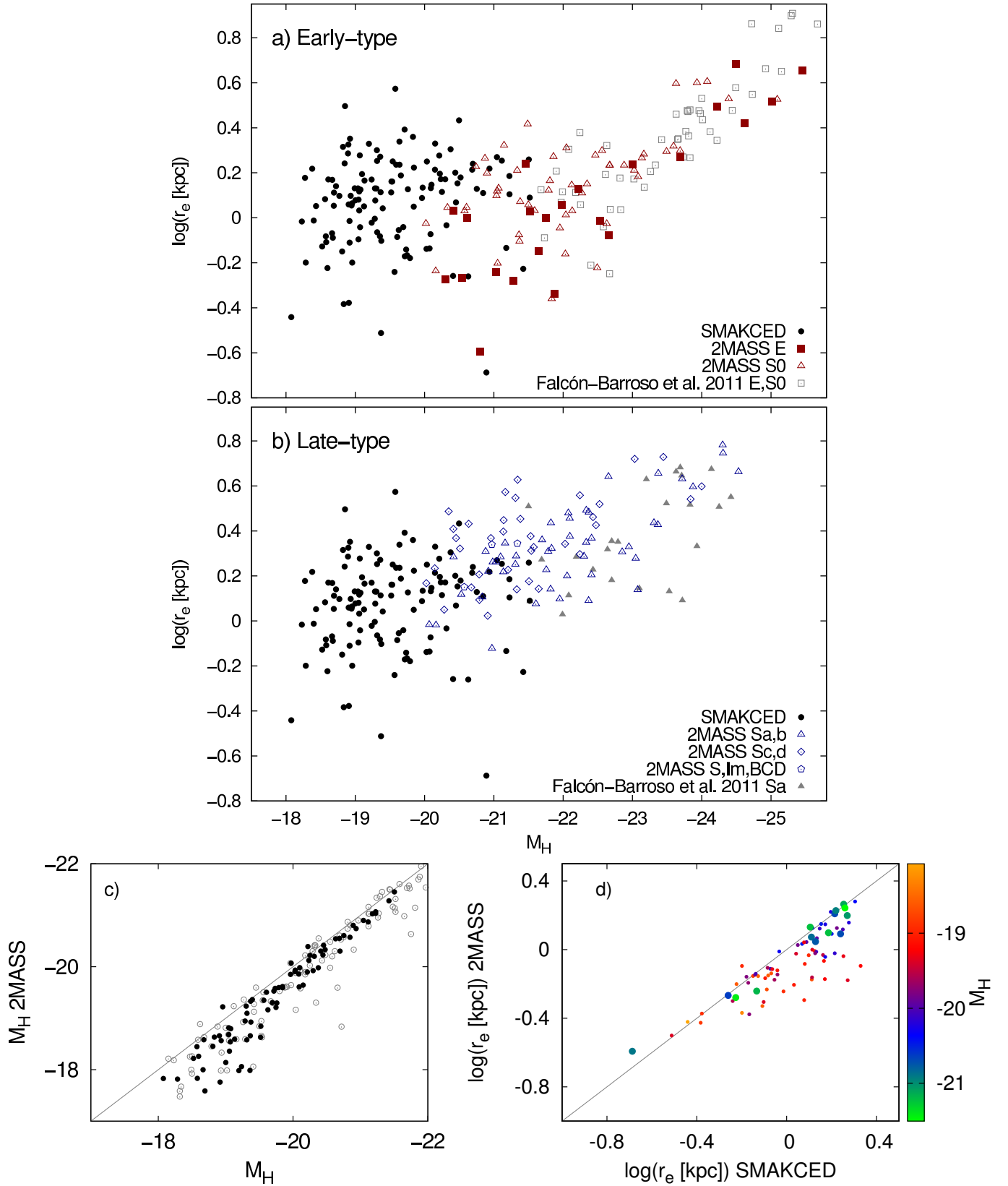


**Figure 9.** Effective radius  $r_e$  of the galaxy versus total galaxy brightness  $M_H$ . The SMAKCED sample galaxies are compared to bright ( $M_H < -20$  mag) early-type galaxies (a) and bright late-type galaxies (b) in the Virgo cluster. The data for the bright galaxies are taken from the 2MASS extended source catalog. Additionally, values for bright galaxies from  $3.6\mu$  Spitzer data (Falc3n-Barroso et al. 2011) are displayed with gray symbols (with  $K - [3.6] = 0.1$  mag, Falc3n-Barroso et al., and  $H - K = 0.21$  mag Peletier et al. 1999). Lower panels: comparison of photometry with 2MASS for our sample galaxies that are in the 2MASS extended source catalog. Note the good agreement for galaxies with  $M_H \lesssim -20$  mag. In the panel c the brightnesses are compared (black points), and for reference the same comparison is shown also for the McDonald et al. (2011) measurements (gray open circles). Panel d compares the size measurements of SMAKCED and 2MASS (for a comparison to McDonald et al. see Appendix E). In this panel the galaxy brightnesses are color-coded according to the colorbar, and galaxies brighter than  $M_H < -20.5$  mag are displayed with a larger symbol.



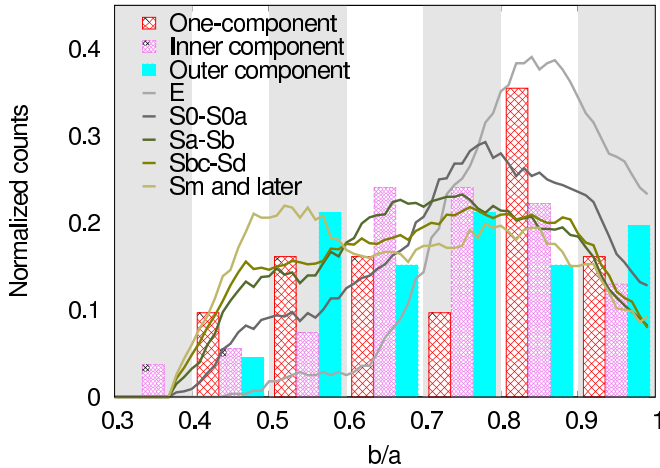


**Figure 10.** Distribution of projected axis ratios of the one-component galaxies and the inner and outer components in the more component galaxies. Our inclination limit falls into the second bin. For comparison the distributions for other galaxy types as found in the SDSS (see text) are shown with running bins of the same bin width of 0.1 and to the same limit of  $b/a = 0.42$ . The histograms are normalized to the number of galaxies in each group.

$2r_e$ . Both distributions have a larger scatter for galaxies with higher ellipticities (see also Bender et al. 1989). However, some more large boxy values occur in the outer parts of those galaxies, which have high ellipticity and are presumably more inclined (lower panel of Fig. 11).

As noted in Section §3.3 the median value of the boxiness parameter might not reveal all boxy or disk sections in the radial profiles. Therefore, Fig. 12 shows the  $\tilde{c}_4/r_e$  values for all sections in the profiles that deviate more than  $\sim 2\sigma$  from an elliptical shape. The measurements are shown with a symbol according to the structural type of the galaxy.

Our algorithm detected 198 such features in 86 of 121 galaxies. Apparently, the distributions of features are slightly skewed to disk shapes in the inner part within  $r_e$ , and to boxy shapes in the outer part beyond  $r_e$  until it becomes too noisy. Interestingly, also in barred galaxies both disk and boxy features appear. This can be understood as a superposition of two components with a large difference in axis ratios, or alternatively due to the intrinsic bar shape.

4.6. Positions and velocities within the cluster

Fig. 13 shows the projected distance to M87 and the line-of-sight velocities of the galaxies relative to M87 in the cluster center (in Appendix D the diagram is shown with the local projected galaxy density as an alternative parameter for the environment). The different groups do not clearly separate. The biggest difference is found between the one-component and barred galaxies. In the innermost bin of clustercentric distance ( $d_{M87} < 1^\circ$  or 0.284 Mpc), these groups strongly differ in their abundance. Furthermore, the velocities of one-component galaxies are peaked towards the cluster velocity, while the barred galaxies have a wider distribution. The two-component galaxies and galaxies with a lens fall somewhat in-between. A KS-test tells that the difference between the distance distributions of one-component and barred galaxies is not significant ( $p \sim 10\%$ ). However, if the one- and two-component galaxies on one hand, and galaxies with a lens or a bar on the other hand, are combined to two groups the test results in 3%, thus showing a significant difference of the two (combined) distributions.

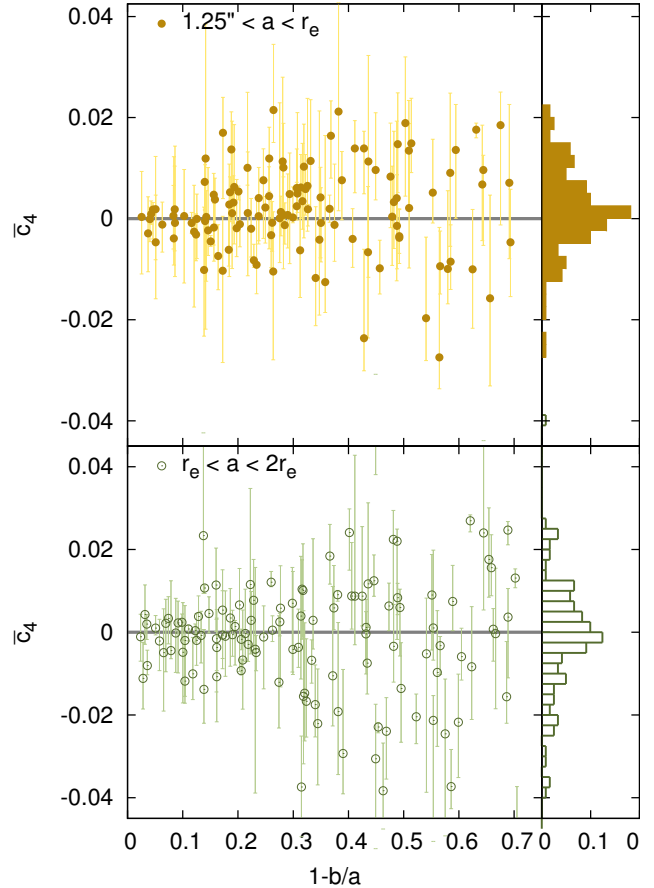


**Figure 11.** The median of the boxiness parameter inside the half-light SMA  $r_e$  and within  $r_e$  and  $2r_e$  versus the median ellipticity of the galaxy within the same region. The bars indicate the semi-inter-quartile ranges of the values. Values larger than 0 indicate disk, while those smaller than 0 mean boxy isophotes.

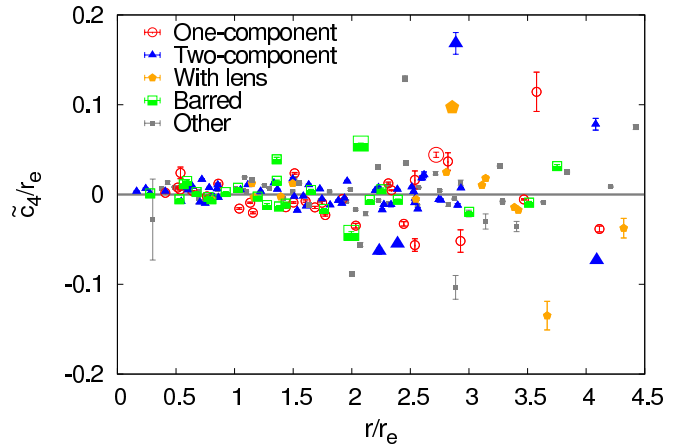


**Figure 12.** Integrated boxiness parameter divided by the effective radius  $\tilde{c}_4/r_e$  versus its position in the radial profile of the galaxy. The error bars indicate the formal uncertainties. Larger symbols are used for features that extend more than the effective radius  $r_e$  of that galaxy. Plotted are 198 features in 86 galaxies. Values larger than 0 indicate disk, while those smaller than 0 mean boxy isophotes.

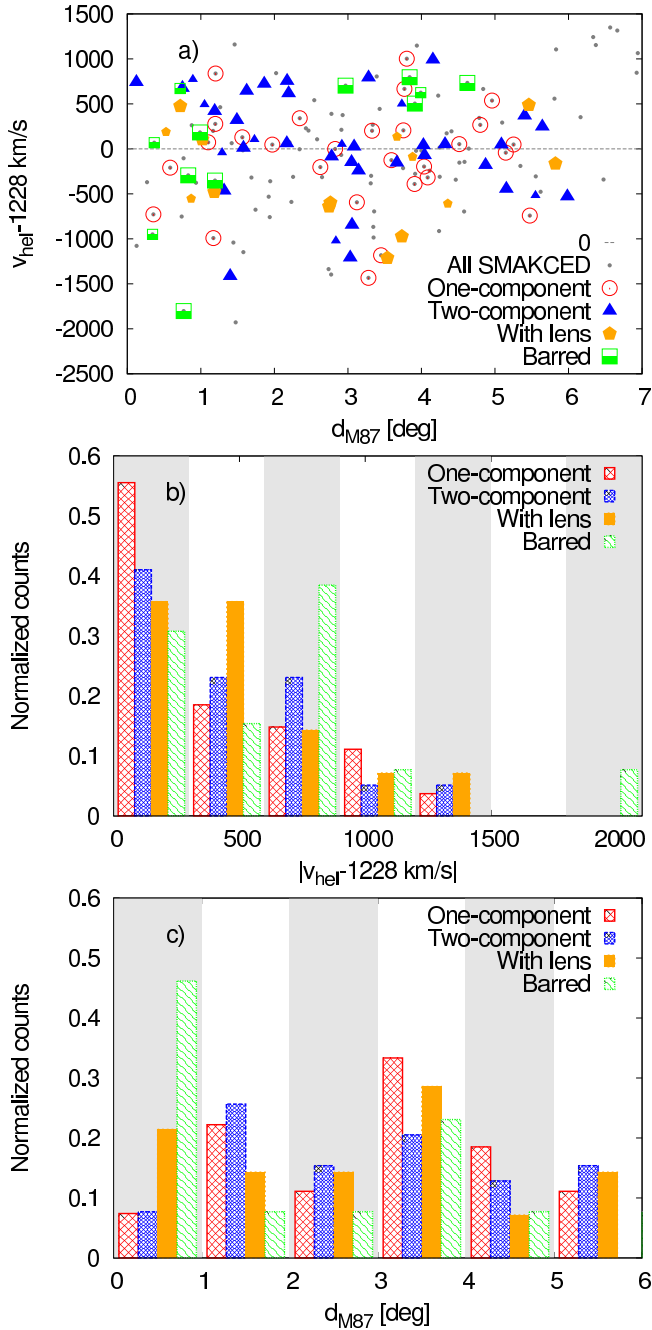


**Figure 13.** *Upper panel:* Projected clustercentric distance versus relative line-of-sight velocity (1228 km/s is the median velocity of all dE(N), Lisker et al. 2009). The smaller colored symbols indicate the galaxies with less certain decompositions. *Middle panel:* Normalized histogram of the relative line-of-sight velocities. *Lower panel:* Normalized histogram of the projected distances to M87. The histograms are normalized to the number of galaxies in each group.

## 5. COMPARISON WITH MORE MASSIVE GALAXIES

In order to judge whether the found components follow any of the scaling relations seen in bright galaxies, we use NIRS0S (Near-InfraRed S0 galaxy Survey, Laurikainen et al. 2011) and OSUBSGS (Ohio State University Bright Spiral Galaxy Survey, Eskridge et al. 2002, decompositions in Laurikainen et al. 2004) as comparison samples. NIRS0S is a magnitude limited ( $m_B \leq 12.5$  mag) survey of all galaxies

( $\sim 200$ ) in RC3 with a Hubble type  $-3 \leq T \leq 1$  and an inclination less than  $65^\circ$ . OSUBSGS is an optical and near-infrared imaging survey of 205 spiral galaxies, also selected from RC3. The sample was limited to  $m_B \leq 12$  mag, to Hubble types  $0 \leq T \leq 9$ , and inclinations less than  $65^\circ$ . The galaxies from these samples are located in many different environments. These studies have the advantage that their decompositions were done in a similar manner as in this study. However, the decompositions were carried out using a different code (BDBAR). In order to ensure the consistency in our comparison, we reran the decompositions of NIRS0S with GALFIT (Appendix F). Some of the galaxies were observed in the  $K$ -band, for which we use the 2MASS  $H-K$  colors to convert the brightnesses to the  $H$ -band.

In Fig. 14 we plot the inner and outer components of the SMAKCED early-type dwarf galaxies (see also Table 5), and compare them with the properties of bulges<sup>15</sup> and disks in the bright galaxies. Again, the photometric scaling relations are shown for the effective radii and galaxy brightnesses, and the corresponding figure with mean effective surface brightness instead of brightness can be found in Appendix D.

The bulges of bright S0–Sb galaxies form a rather steep relation in effective radius<sup>16</sup> versus brightness (Fig. 14a). The later types show more scatter, a few even fall into the region occupied by the inner components of the dwarfs. The latter follow a relation with a similar slope like the bulges in bright galaxies, but offset towards larger radii. However, this relation might partly be due to the limited range of total brightness: for galaxies with similar total brightness, the inner components of the complex galaxies have to be smaller and fainter than the one-component galaxies, i.e. whole galaxies. Interestingly, the one-component galaxies just seem to scatter, while for the two-component galaxies the size and brightness of the inner component are correlated (Spearman’s  $r$  and  $p$ :  $r = 0.07$  and  $p = 70\%$ ,  $r = -0.51$  and  $p = 0.7\%$ , respectively).

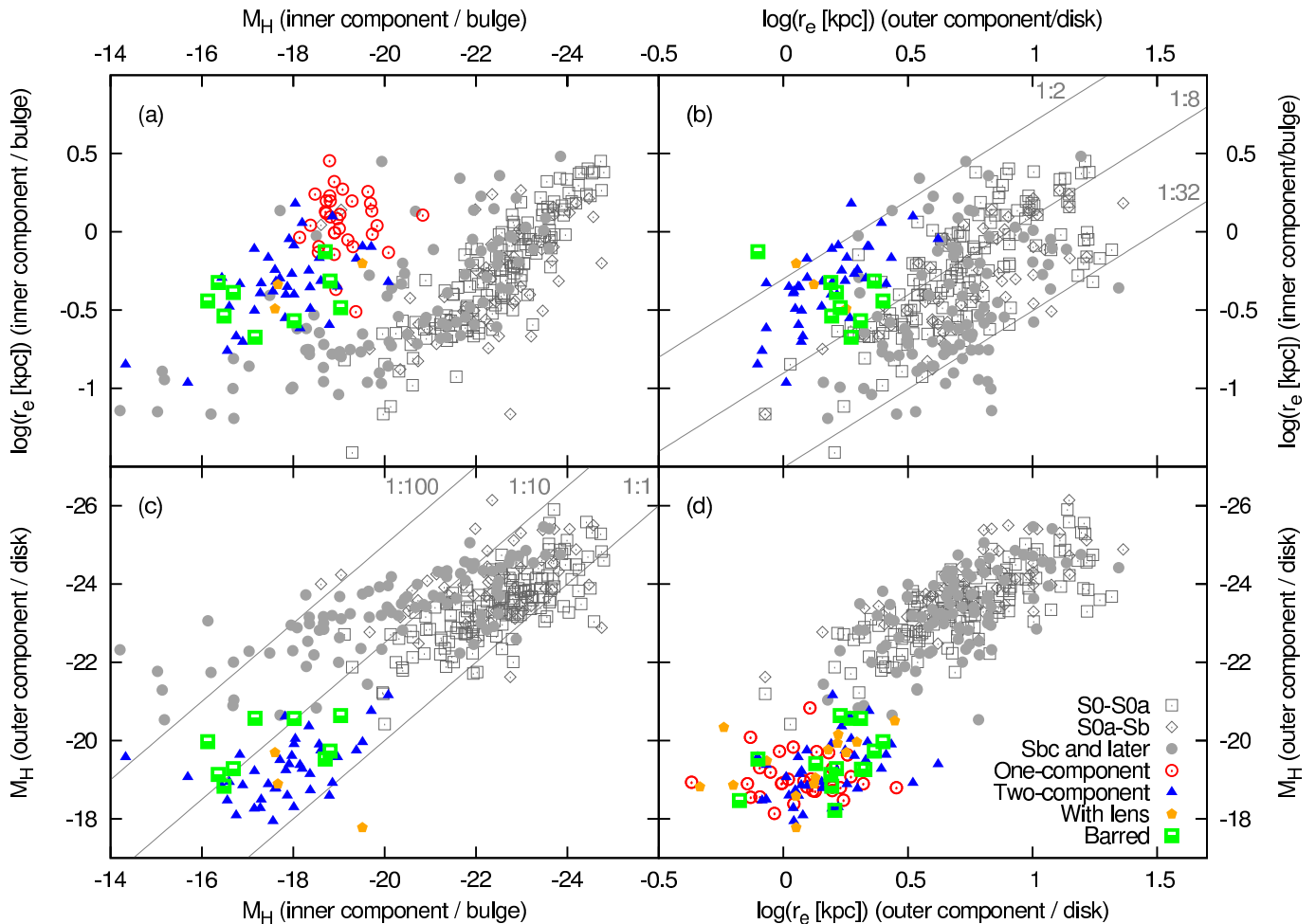
For the bright galaxies also the disk size scales with its brightness (Fig. 14d), although the relation is broader than for the bulges. If the relation of the bright galaxies is extrapolated the dwarfs do not fall on it. Their outer components are larger. However, the about 10 faintest non-dwarf galaxies might hint at some turn of the relation towards larger radii. Due to the sample selection faint late types do not form part of OSUBSGS. A different comparison sample would be needed to confidently judge whether or not the relation turns to the outer components of the dwarf galaxies.

Fig. 14b illustrates that the sizes of the bulges and disks of bright galaxies are correlated as well. The inner and outer components of the dwarfs show a similar relation but are offset towards a ratio of the sizes of the inner and outer component closer to unity. (The average value for the late-type spirals is consistent with the findings of Courteau, de Jong, & Broeils 1996). This could be a hint that the components are not of the same nature as the bulges and disks in bright galaxies.

In Fig. 14c the brightnesses are plotted, thus effectively illustrating the bulge to disk ratio, and the ratio of light in the inner and outer components. For the bright galaxies the Hubble sequence becomes visible: the later types have less prominent

<sup>15</sup> “Bulge” refers here to the bulge component in the photometric decomposition and does not imply any physical meaning.

<sup>16</sup> Note that, the effective radii (that is, half-light aperture SMAs) of components are also referred to by  $r_e$ , although they are obtained by fitting profiles to components and are not non-parametric quantities (§3.4).



**Figure 14.** The inner and outer components of the galaxies in our sample are shown in the scaling relations of the bulge and disk components of the bright galaxies. The earliest bin of Hubble types is taken from NIRS0S and the two other from OSUBSGS (see text). Panels (a) and (d) display the relations of brightness and radius of the inner/bulge or outer/disk components, respectively, versus the corresponding parameter of the other component. Panels (b) and (d) show the scalings for radius and brightness, respectively, versus the corresponding parameter of the other component. In panel (b) the gray lines show a ratio of the effective radii of bulge and disk (or of the inner and outer component) of 1:2, 1:8 and 1:32, while in panel (c) they show a bulge to disk (or inner to outer component) ratio of 1:1, 1:10 and 1:100. The one-component galaxies of our sample are plotted in both the bulge and disk panels, while the for galaxies with a lens in addition to only one ‘global’ component, we add that global component to the disk panel. Galaxies with lens or bar are plotted in the respective panels, if there was an inner Sérsic or outer component fitted in the decomposition.

bulges. The clearest relation exists for the bulges of the S0 galaxies. The later types are offset to smaller bulge-to-disk ratios. The ratio of inner-to-outer component in the dwarf galaxies fall about on the extension of the relation for early-type disk galaxies. Also here a comparison sample for the latest type galaxies is missing. We conclude that the common bulge-plus-disk picture of bright galaxies is not applicable to the combination of inner and outer components of early-type dwarfs.

## 6. DISCUSSION

### 6.1. Multicomponent structures

In this study nearly two thirds of the early-type dwarfs are found to have complex structures. The fraction of one-component galaxies is found to be highest in those early-type dwarf galaxies, where no disk features or central star formation was detected (Lisker et al. 2006a,b). This might not be so surprising, because of the way disk features were detected by

Lisker et al.. Their unsharp masking reveals spiral arms, bars, and possibly edge-on disk components. Some of the spiral arms that we see in our images are found in one-component galaxies. All the other features, however, are likely to be related to multi-component structures. The strongest correlation with the decomposition characterization is found with galaxy brightness: at the bright end of the sample the fraction of one-component galaxies is about 0% and it increases steadily towards fainter galaxies. The trend seems plausible, since the low mass galaxies are expected to be more easily affected by dynamical heating that can wash out structures or prohibit their formation.

Already Binggeli & Cameron (1991) defined 5 different surface brightness profile types (their Fig. 6). Their group I comprises profiles that deviate globally from an exponential shape. They did not consider the Sérsic function for the profiles at that time, and many of these may in fact be fitted with a single Sérsic function. Their groups IVa and IVb are profiles following an exponential function, with and without a nucleus, respectively. Therefore, the profiles of groups I,



IVa, and IVb correspond to our models using a single Sérsic function or a Sérsic function plus nucleus. The profiles in their groups II, IIIa, and IIIb show a break: the outer part can be described with an exponential function. However, the inner part does not follow this outer exponential. It either follows an exponential function with a shorter scale length (IIIa and IIIb with and without an additional nucleus) or is steeper than an exponential (which we would describe with a Sérsic function with  $n > 1$ ). Therefore, these three groups correspond to our two component galaxies. Additionally [Binggeli & Cameron](#) have a type V, which has a deficiency of flux in the center compared to an exponential profile (also see [Allen et al. 2006](#)). These models might be to some degree represented in our models with an outer component with  $n < 1$ . Thus [Binggeli & Cameron](#)'s results did already indicate part of the structural complexity of the early-type dwarf galaxies found in this study, but with the Sérsic profile becoming popular, their profile classifications were largely forgotten.

[Gavazzi et al. \(2001\)](#) fitted the near-infrared light profiles of over 1000 galaxies of all types, including galaxies in the Virgo cluster, with a de Vaucouleurs  $R^{1/4}$  law, an exponential function, or a bulge+disk combination. A handful of objects were early-type dwarf galaxies, and the authors found that not all of them follow a simple exponential profile. [Barazza, Binggeli, & Jerjen \(2003\)](#) studied Virgo cluster early-type dwarf galaxies in the optical ( $B$ - and  $R$ -band). They state in the abstract that ‘the observed profiles of the brightest cluster dwarfs [in the Virgo cluster] show significant deviations from a simple Sérsic model, indicating that there is more inner structure than just a nucleus.’ They stress that radial profiles of parameters like the ellipticity and position angle support this finding. The features in the profiles are not restricted to objects like IC3328, where unsharp masking or model subtraction can reveal spiral arms, but occur also in ‘many apparently normal dEs’. Based on HST data from the ACS VCS, [Ferrarese et al. \(2006\)](#) reported the detection of stellar disks on nuclear and kiloparsec scales, as well as bars, in more than half of the Virgo early-type galaxies with ‘intermediate luminosity’. More recently, [McDonald et al. \(2011\)](#) did profile decompositions using near-infrared images for 286 Virgo cluster galaxies, of which about 65 are early-type dwarfs. They find a similar fraction of galaxies that are fitted by simple exponential profiles as opposed to more complex galaxies with two-component profiles (see also Appendix E). For individual galaxies a different decomposition might be reported in the mentioned studies, since they use one-dimensional, sometimes automated profile fitting, different model assumptions such as the possibility of separately fitting nuclei or restricting the single component models to exponential profiles (as it is the case in [McDonald et al. 2011](#)). Also, the decompositions presented in this study rely on a higher image quality. However, qualitatively our results are consistent with theirs.

In the following we discuss studies in which the profiles and morphologies of early-type dwarfs in the Coma cluster are studied, mostly using HST data (for Fornax see e.g. [Smith et al. 2012b](#) and [Turner et al. 2012](#)). The Coma cluster is denser and richer than the Virgo cluster. [Graham & Guzmán \(2003\)](#) fitted light profiles and in obvious cases included an outer exponential component in addition to a Sérsic component (and a nucleus when present). They found 3 galaxies out of 18 to be complex. [Aguerri et al. \(2005\)](#) fitted about 100 light profiles of early-type galaxies within the magnitude range  $-18 \leq M_B \leq -16$  mag. Using the largest devia-

tion of the fit from the observed profile as a criterion, they found 34% of the galaxies, with reliable photometry, to be complex. [Méndez-Abreu et al. \(2010a\)](#) focused on detecting bars in early-type dwarf galaxies. Their bar fraction and its decrease towards lower galaxy brightnesses is consistent with our findings. [Marinova et al. \(2012\)](#) used unsharp masking to identify disk signatures like spiral arms and bars for a larger sample of 333 galaxies ( $M_V > -18$  mag). Only 13 galaxies host such features. However, they conclude that this is in good agreement with [Méndez-Abreu et al. \(2010a\)](#) and the decline of the bar fraction towards fainter galaxies. Interestingly, for bright S0 galaxies they find a similar bar fraction as in Virgo, despite the higher galaxy density. They suspect an interplay of two effects of the higher galaxy density to cause the similar bar fractions in the different clusters, similar to [Janz et al. \(2012\)](#)'s suggestion for the early-type dwarfs in the Virgo and the Coma cluster: encounters are more frequent, but the galaxies are more stable against bar instabilities. [Marinova et al.](#) argue that the higher stability of galaxies in the dense environment is due to a more effective dynamical heating of the galaxies, a smaller gas fraction, and encounters being less efficient due to higher relative velocities.

## 6.2. Isophotal shapes and kinematics

The isophotes of elliptical galaxies show small deviations from ellipses: galaxies with disky and/or boxy isophotes are common. [Bender \(1988\)](#) showed that disky galaxies ( $c_4 > 0$ ) are always consistent with being rotationally flattened, while boxy galaxies frequently are supported by anisotropic velocity distributions and rotating slowly. A larger dataset, based on SDSS data, later published by [Pasquali, van den Bosch, & Rix \(2007\)](#), shows the same effect, and that the fraction of rotating objects increases going to lower magnitudes. We find that this trend breaks down for  $M_r > -19$  mag, i.e. in the dwarf regime. Measuring the boxiness as indicated in Section §3.3 we find a considerable scatter in the boxiness at every magnitude, both inside  $r_e$  and between  $r_e$  and  $2r_e$  (Fig. 15).

[Toloba et al. \(2009\)](#) found that galaxies in the center of the Virgo cluster are less supported by rotation than galaxies in the outer regions. At the same time they were older and more boxy (see their Fig. 2, and see also [Toloba et al. 2011](#)). Here we try to reproduce the relation between kinematical support and boxiness.

For the kinematics we made a compilation of the available literature data ([Simien & Prugniel 2002](#); [Pedraz et al. 2002](#); [van Zee et al. 2004](#); [Chilingarian 2009](#); [Toloba et al. 2011](#)). For galaxies covered by more than one published dataset, we gave preference to [Toloba et al.](#) and choose the one with the largest radial extent of the rotational curve otherwise. These studies measure the velocity dispersion  $\sigma$  in different ways. One should realize that our literature compilation is a heterogeneous set of measurements, with in which  $\sigma$  has been determined in different ways, and which does not allow an in-depth investigation. For that reason the largest dataset, the one of [Toloba et al. \(2011\)](#), is indicated in larger symbols in Fig. 16, where the ratio of rotational velocity and central velocity dispersion is shown as a function of ellipticity. Since for most galaxies the rotation curves are still rising, the  $v/\sigma$  values should be considered as lower limits. Overall, we do not find any differences in the kinematical characteristics of the galaxies from different structural groups. This statement holds also when restricting the analysis to the homogeneous data of [Toloba et al.](#) Interestingly, also the one-component galaxies with kinematics show no evidence of being slow ro-

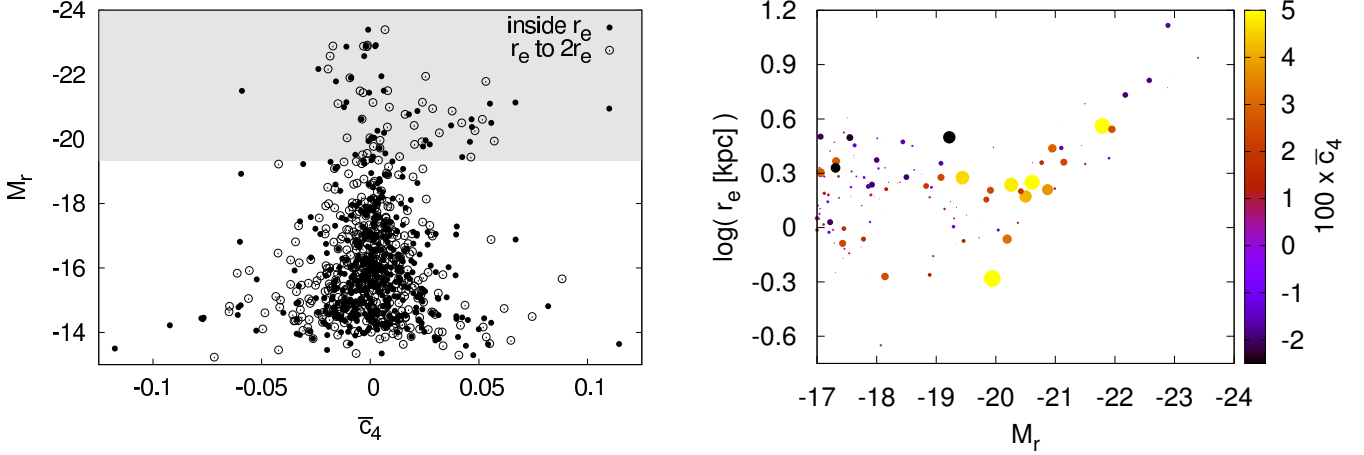


**Figure 15.** *Left panel:* boxiness versus galaxy brightness for all early types in Virgo, using  $r$ -band images from SDSS; data from profiles fits in Janz & Lisker (2008). The gray area indicates the bright galaxies, for which there is the trend of galaxies being more disky towards fainter galaxy brightness. Filled and open symbols mark the boxiness inside  $r_e$  and between  $r_e < r < 2r_e$ , respectively. Values larger than 0 indicate disky, while those smaller than 0 mean boxy isophotes. *Right panel:* the value of the boxiness is shown in the optical brightness versus radius relation (Janz & Lisker 2008) for early-type dwarfs and bright early types. The boxiness is color coded and the size of symbols reflects the absolute value so that the galaxies with nearly elliptical isophotes disappear.

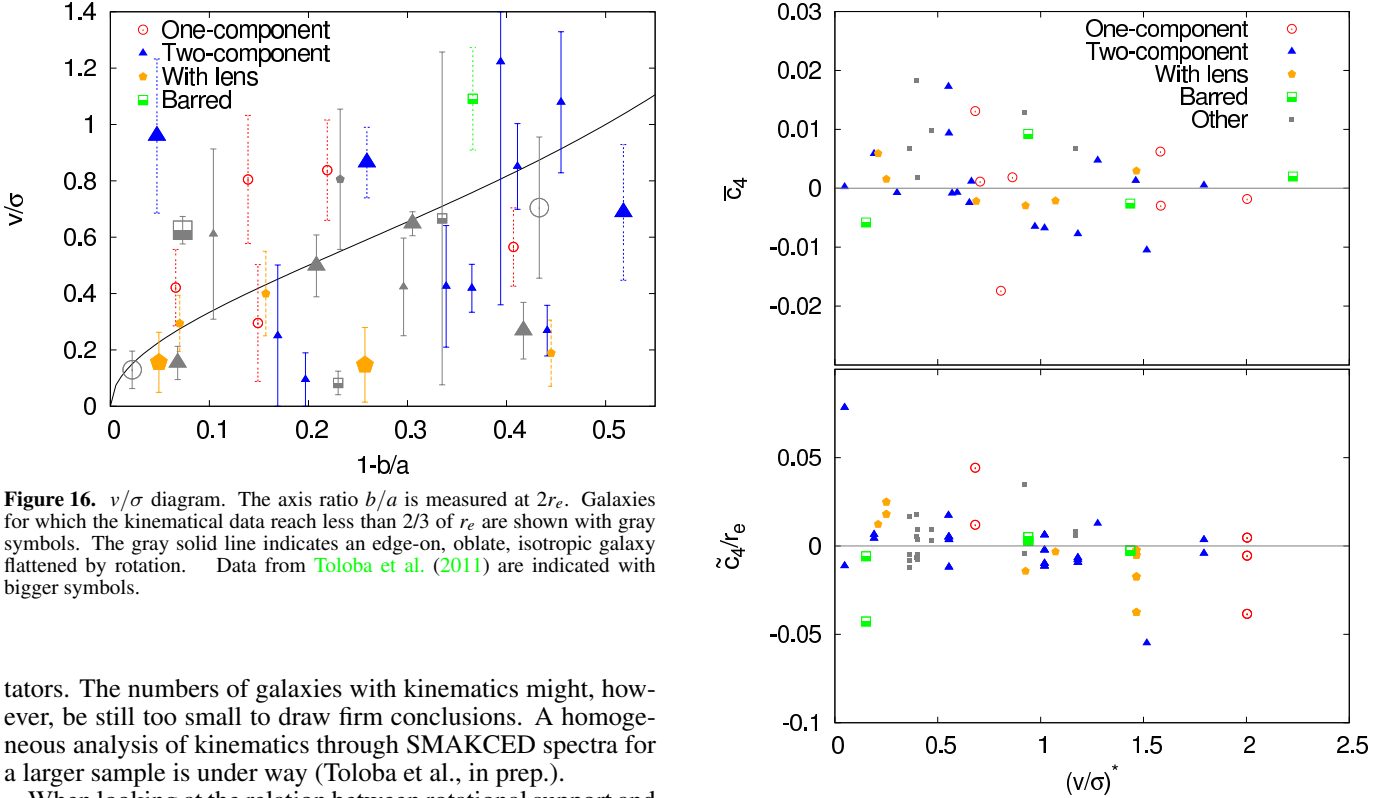


**Figure 16.**  $v/\sigma$  diagram. The axis ratio  $b/a$  is measured at  $2r_e$ . Galaxies for which the kinematical data reach less than  $2/3$  of  $r_e$  are shown with gray symbols. The gray solid line indicates an edge-on, oblate, isotropic galaxy flattened by rotation. Data from Toloba et al. (2011) are indicated with bigger symbols.

tators. The numbers of galaxies with kinematics might, however, be still too small to draw firm conclusions. A homogeneous analysis of kinematics through SMAKCED spectra for a larger sample is under way (Toloba et al., in prep.).

When looking at the relation between rotational support and boxiness we use  $(v/\sigma)^*$ , i.e.  $(v/\sigma)/\sqrt{\epsilon/(1-\epsilon)}$ . Although this parameter does not contain much information for galaxies with  $\epsilon \sim 0$ , it allows us to investigate in a rough way whether boxiness correlates with rotational support. Fig. 17 shows both the median boxiness and all the individual boxiness features identified in the radial profiles (see §3.3). For neither panel a correlation between disky isophotes and rotational support is seen. If any relation at all is present, it goes to the other direction. When trying to understand this, and why Toloba et al. (2011) do find a correlation between disky isophotes and rotational support, one has to realize that we determine  $c_4$  differently from Toloba et al.. They assigned

**Figure 17.** Boxiness versus  $(v/\sigma)^*$ , with kinematic values from literature. In the upper and lower panel the boxiness is quantified by the median boxiness ( $\bar{c}_4$ ) and the integrated values of boxy or disky features ( $\bar{c}_4/r_e$ ), respectively. Values larger than 0 indicate disky, while those smaller than 0 mean boxy isophotes.

galaxies with clear disky features in the profile the largest peak value for  $c_4$ , regardless of the behavior of the rest of the profile and of its median value. In case no significant disky feature was found, the median value of the profile was used even if there were boxy subsections. In our analysis here we treat boxy and disky profiles in the same way.

While the quality of the kinematic measurements (uncertainties shown in Fig. 16) only allow us to look for general trends, the same trend that is seen in Fig. 17 with  $(v/\sigma)^*$  would be seen when plotting instead  $v/\sigma$  or only  $v$  on the ordinate, and also when removing the faintest galaxies and the ones with low radial extent from the sample. At this point it should be mentioned that Ryś et al. (2013), using two-dimensional spectra for a small sample of Virgo early-type dwarfs, recently reported that kinematically the dwarfs form anything but a homogeneous group of objects. Furthermore, it can be noted that Emsellem et al. (2011) did not find the strong correlation between boxiness and rotational support of Bender (1988) for bright galaxies, using a sample spanning a larger range in galaxy brightness than Bender.

Generally, disk isophotes are thought to be related to disks. For boxy shapes in the dwarf systems one suggestion is that they are so-called naked bars (Mastropietro et al. 2005): a strong bar is induced in a disk by an encounter. Subsequent encounters harass the galaxy further and remove the outer disk so that only a bar-like shape remains, which might be boxy. In the most extreme case they might even be caused by mergers of two disk galaxies with appropriate orbital geometry (see discussion of the boxy shape in Graham et al. 2012). All these interpretations attribute the boxy shape to disk phenomena. As seen before, especially galaxies with high ellipticity, presumably inclined galaxies, have boxy sections in the outer parts of the profiles, which is consistent with the aforementioned explanations.

### 6.3. Are early-type dwarf galaxies dwarf versions of ellipticals?

It is still debated, whether it can be concluded from photometric scaling relations (e.g. Fig. 9a) that the early-type dwarfs and bright early-type galaxies are distinct galaxy types, or that they follow one curved relation. Kormendy et al. (2009) suggest that they are different, and that compact ellipticals like M32 are the true low brightness ellipticals (Wirth & Gallagher 1984). However, Graham & Guzmán (2003) show that scaling relations including the effective radius  $r_e$  or the effective surface brightness  $\langle\mu\rangle_e$  have to be curved, if the galaxy profiles follow Sérsic functions and the Sérsic parameters  $\log(n)$  and  $\mu_0$  form linear relations with the galaxy brightness. Janz & Lisker (2008) find deviations from this expected curved behavior in the size brightness diagram (their Fig. 2): the brightest dwarf galaxies are too large, while the faintest non-dwarf galaxies at a similar brightness are too small.

This is tentatively confirmed with our NIR data (see Fig. 9a). Our multi-component analysis gives a possible explanation for why the galaxies do not follow exactly the curved relation, even though Graham & Guzmán’s argument is a rigid, mathematical one. Namely, we find that the assumption that all the galaxies can be described with a single Sérsic profiles is not fulfilled. The multicomponent structures and their higher frequency in brighter galaxies cause a relation between the concentration parameter and the galaxy brightness (see Appendix D). When fitting with single Sérsic functions the higher concentration results in a higher Sérsic  $n$  (Fig. 8, see also Appendix C) and thus also to a relation between the effective Sérsic  $n$  and galaxy brightness. However, the multi-component nature by itself may not invalidate the existence of a general curved relation of effective radius versus galaxy brightness for the *global* galaxy properties.

A similar thing can be seen in Fig. 15 with the boxiness: from bright to fainter galaxies the bright early types change

from being boxy to becoming more and more disk. On the other hand, the early-type dwarfs have both boxy and disk shapes. We note that at intermediate brightness, where galaxies classified as dwarf and as bright early types overlap, the difference in radius is largest between early-type dwarf and E galaxies. In boxiness, the difference is instead largest between early-type dwarf and S0 galaxies. Also, the smallest elliptical galaxies scatter around zero boxiness. Thus we refrain from a statement about the true low-mass ellipticals. The compact ellipticals may be the extension of the elliptical galaxies towards lower mass (Kormendy et al. 2009). Alternatively, a population of true low mass ellipticals may exist and exhibit similar radii for a given brightness as the majority of early-type dwarf galaxies, as predicted if they have Sérsic profiles and follow the linear relations of the Sérsic parameters with the profiles (Graham & Worley 2008; Graham 2011). In this case the compact ellipticals may be tidally stripped galaxies in the vicinity of massive galaxies (e.g. Smith Castelli et al. 2008; Price et al. 2009; Chilingarian 2009, the latter two also report multi-component structure for the compact ellipticals, as it was found for M32 by Graham 2002). Huxor et al. (2011) found evidence of stripping for a number of compact ellipticals. Or, as a third possibility, true low-mass ellipticals might be rare objects.

In the context of comparing the early-type dwarfs with bright ellipticals and early types (E&S0) it should also be noted that the existence of structures beyond light distributions following simple Sérsic models alone does not make the dwarfs necessarily different from bright ellipticals. Recently, Huang et al. (2013) used three to four Sérsic functions to describe the overall light distributions of bright ellipticals. Also, it is noteworthy that the SAURON/ATLAS3D project found the red low-mass galaxies, despite their classification as ellipticals, to be relatively fast rotating in general ( $v/\sigma \sim 1$ ; Emsellem et al. 2011), similar to many early-type dwarfs. However, among those there are also slowly rotating ones (see e.g. Toloba et al. 2011).

### 6.4. Nature of inner components and one-component galaxies?

The inner components that we find in dwarf galaxies do not resemble bulges in bright galaxies. Their profiles are close to exponentials, i.e. the median value of the Sérsic index is  $n = 1.15$ , 75% of the inner components have  $n < 1.6$ . Their flattening distribution is similar to that of the outer components. In fact, the flattening distributions of the inner and outer components are similar to that of spiral galaxies. Also, the shapes of bulges and disks (identified with decompositions) in low mass late-type galaxies might be similar (see e.g. Méndez-Abreu et al. 2010b). Most of them are thought to arise in the secular evolution of the galaxy and are then called pseudobulges (Kormendy & Kennicutt 2004). However, the inner components in this study are clearly offset from the scaling relations of bulges in bright galaxies.

The photometric parameters of one-component galaxies are apparently more similar to those of the outer components of the complex galaxies. They are also not significantly rounder. The few one-component galaxies with kinematics show significant rotation. The last point may be a selection effect, since round galaxies might not have been the preferred objects in studies of rotation. If one assumes that some process causes the multi-component structure, then the galaxies with one component could either be not yet processed, or the multi-component structure could be destroyed. The flattening

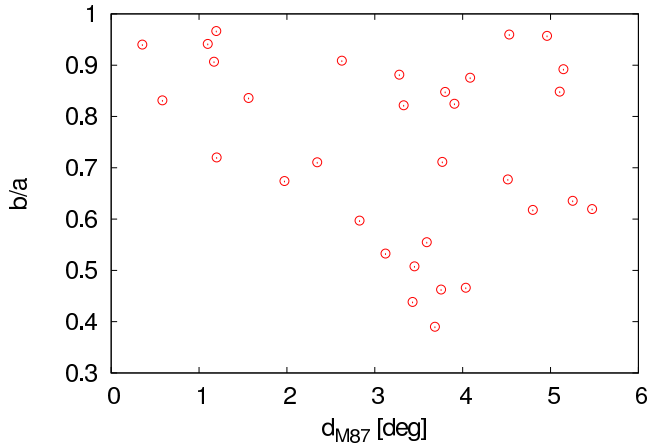


**Figure 18.** Axis ratio of one-component galaxies versus clustercentric distance. One-component galaxies with flat shapes do not exist in the cluster center.

distribution of one-component galaxies appears to be double-peaked (see Fig. 10). The flatter one-component galaxies are found only at larger projected clustercentric distances (Fig. 18; see also Lisker et al. 2009) and tend to have smaller concentration indices than the round ones. When selecting these one-component galaxies with large axis ratios, a trend is seen for them to have higher concentration indices in dense regions (which is not simply caused by a relation between the concentration and the galaxy brightness). While these statements about the one-component galaxies are clearly tentative, they hint at the population of one-component galaxies being complex.

The fact that the fraction of one-component galaxies strongly increases towards objects of fainter magnitude, i.e. lower stellar mass, may be interpreted in two ways. Either the continuous tidal influence has been so strong for lower-mass galaxies that most structures that had formed have already been smoothed out again, or they did not form in the first place. The latter could be due to a possibly thicker shape of the progenitor galaxy at lower masses (Kaufmann et al. 2007; Sánchez-Janssen et al. 2010), thus being dynamically hotter, or due to the lower binding energy that makes it less likely to develop internal structures. These scenarios could be tested with dedicated simulations, and would represent a striking example for the “fossil record” of galaxy evolution mechanisms that is imprinted in early-type dwarfs.

### 6.5. Late-type galaxies as possible progenitors

While a few of the latest types in the OSUBSGS comparison sample have bulges similar to the inner components in the dwarfs, the inner components are clearly offset from an extension of the bulge relation in bright galaxies (see Fig. 14). Given that the inner structures are so different, can the early-type dwarf galaxies be transformed late-type galaxies?

It is worth mentioning that the increasing number of multi-component galaxies towards higher brightness resembles the increasing complexity in the late-type galaxy mixture. Using profile decompositions, Gavazzi et al. (2001) found a similar trend from simple exponential galaxies to two-component late types towards brighter galaxies. The fraction of simple galaxies in their study is similar to that in this study: among Sc galaxies it is slightly larger, and smaller among Sd/Sm galaxies. This calls for a comparable multi-component study of low mass late-type galaxies, in order to see whether our results can

be reproduced by pre-existing multicomponent structures (see also Graham & Worley 2008) that survive the disk thickening during the transformation process (Gnedin 2003; Smith et al. 2010 – tidal heating, Smith et al. 2012a – gas depletion from ram pressure stripping). In this context it is worth noting that the old stellar population of the blue compact dwarf galaxies is morphologically similar to the more compact  $\sim$ half of the early-type dwarf galaxies (Meyer et al. 2013).

Another option is that the structures are created during the transformation process (for a review of various transformation processes, see e.g. Boselli & Gavazzi 2006). The complete transformation includes removal of the gas and dynamical heating of the galaxy. In a massive cluster the hot gas is assumed to effectively strip the internal gas of a galaxy via ram pressure. With the Gunn & Gott criterion (Gunn & Gott 1972) it can be shown that the more massive early-type dwarf galaxies should be able to retain some gas in the galaxy center, with typical numbers for a passage through the cluster avoiding the very center. The central star formation can continue for a longer time or might even be enhanced. Roediger (2009) shows that the Gunn & Gott criterion works reasonably well for most geometries. She also discusses that the ram pressure may or may not enhance the star formation in those regions of the galaxy, where the gas is not yet stripped (see also Vollmer et al. 2001; Bekki & Couch 2003). A few early-type dwarf galaxies in the Virgo cluster are detected in H I (Hallenbeck et al. 2012).

In case harassment is to play a role in the dynamical heating of the galaxy, the high speed encounters can induce bar formation in the perturbed galaxy (Mastropietro et al. 2005). If there is still gas in the galaxy, the bar can effectively transfer it to the central regions of the galaxy (Shlosman, Frank, & Begelman 1989; Shlosman, Begelman, & Frank 1990). Even without any gas the bar can redistribute the stellar mass and lead to a profile steepening, as illustrated by the simulations of Mastropietro et al. (2005). This also demonstrates that the different components that we found can simply be different parts of the disk.

In case the increase of concentration and changes to the light profile are inherent to the disk, no significant differences in the shapes and other parameters of the inner and outer components are expected. Also the similar flattening distributions of the early-type dwarf galaxies and their possible progenitors (see also Ferguson & Sandage 1989; Binggeli & Popescu 1995; Sung et al. 1998) are explained in such scenarios.

In this context the spiral structures and disk signatures detected with image enhancements in some of the early-type dwarf galaxies fit into the above picture (Jerjen et al. 2000; Lisker et al. 2006b; Lisker & Fuchs 2009 for the Virgo, Graham & Guzmán 2003 for the Coma cluster, de Rijcke et al. 2003 for the Fornax cluster). Recently, van den Bergh (1976)’s idea of parallel sequence classification was substantiated observationally (Laurikainen et al. 2010; Cappellari et al. 2011; Kormendy & Bender 2012). In particular, Kormendy & Bender place the early-type dwarf galaxies at the end of the S0 sequence on the side opposite to the bright ellipticals, with late Sc, Sd, and Im galaxies being their late-type relatives. This is in contrast to Sandage & Binggeli (1984), who categorized the early-type dwarf galaxies as low mass ellipticals (although they anticipated a possible evolutionary connection to late-type galaxies). Detailed models and observations still need to show that the multi-component structures in low mass late-type galaxies and early-type dwarfs are compatible or, alternatively, that the structures are created in



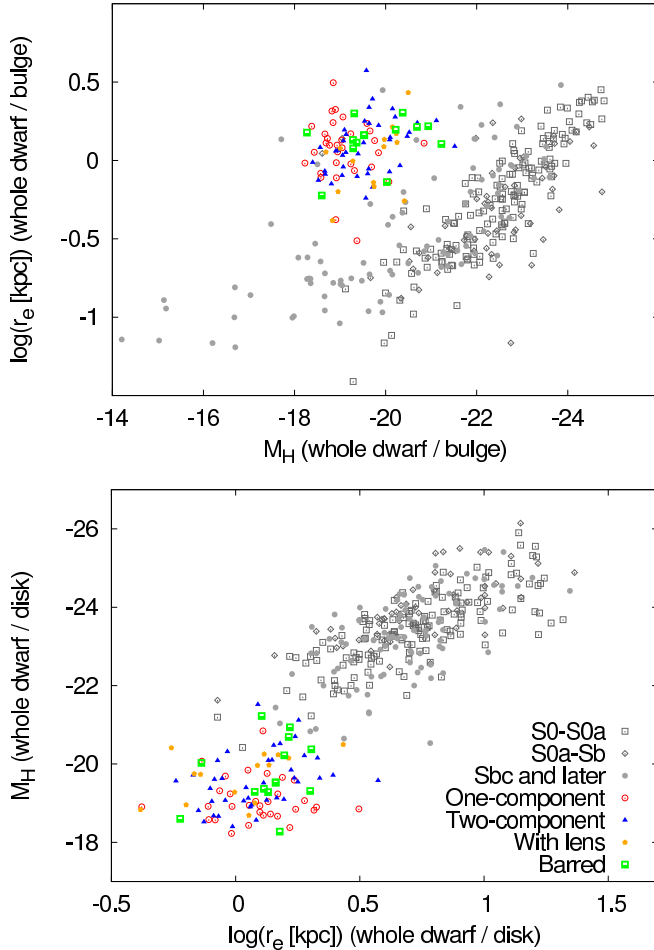


**Figure 19.** Same as Fig. 14 panels *a,d*, but plotting for the dwarf galaxies instead of the inner and outer components the photometry of the whole dwarf galaxy.

the transformation process. Additionally, it has to be shown that the abundance of nuclei (see e.g. Côté et al. 2007) and the larger number of globular clusters in the early-type dwarf galaxies are not a problem in the scenarios, in which late-type galaxies are transformed to early-type dwarfs. Boselli et al. (2008b) suggest that these two issues can be explained by the fading of the transformed galaxy relative to the unperturbed one (see however Sánchez-Janssen & Aguerri 2012 and Smith et al. 2013). Moreover, Lisker et al. (2013) point out that the progenitor galaxies, which were possibly transformed into the early-type dwarfs we observe today, are not necessarily similar to present-day late types.

If the whole galaxy photometry of the early-type dwarfs is compared to the bulge and disk scaling relations of the bright galaxies, they behave more like the disks than the bulges (Fig.

19), as also pointed out by Kormendy & Bender (2012). We conclude that the early-type dwarfs, based on their structural appearance, may be descendants of bulgeless starforming disk galaxies from earlier epochs.

## 7. SUMMARY

We presented the infrared imaging part of the SMAKCED survey of 121 early-type dwarf galaxies in the Virgo cluster. The images are deep, some are probably close to what can be achieved for a large number of galaxies from the ground with today’s instrumentation. The sample is a nearly complete sample of all early-type galaxies in the Virgo cluster in a brightness range of  $-19 < M_r < -16$  mag.

For the first time two-dimensional multi-component decompositions for the early-type dwarf galaxies in the Virgo cluster have been carried out. While the global profiles of most galaxies could be approximated with a single Sérsic functions, more detailed inspections revealed that most of them also show deviations from that, which potentially offers valuable insight in the galaxies’ past. The fraction of galaxies well described by a single Sérsic profile is only about one third. Furthermore, we find a fraction of galaxies with lenses of 14%, and a fraction of barred galaxies of 16%. This is qualitatively consistent with earlier profile decomposition studies, but more robust, since it is based on higher quality near-infrared images. Furthermore, the two-dimensional approach allowed for quantitative comparisons between the different structural components, and with the bulges and disks of bright galaxies.

The overall photometry places the galaxies in scaling relations as predicted by Graham & Guzmán (2003), but with the deviations described in Janz & Lisker (2008). If the dwarfs nonetheless relate to giants, they do so in a non-homologous fashion. However, dwarfs and spirals do show no sign of a discontinuous relation in the same diagram. Moreover, the frequent multi-component structures argue in favor of a disk-like nature of the early-type dwarf galaxies. Interestingly, we find that, while the brightest early types have on average boxy isophotes, contrary to the disky early types at intermediate brightness, the dwarfs show as often boxy as disky shapes, but have on average elliptical isophotes. We speculate that for the dwarf systems both disky and boxy shapes are probably related to disks.

In addition to the overlap with late-type galaxies in the photometric parameters of the whole galaxies, the outer components may fall on the extension of the late-type (Sbc and later) spiral disks. However, the inner components are offset from the relations of bulges in the bright galaxies. We argue that they are not likely to be bulges, but potentially from parts of initially exponential disks, which would have gained a higher concentration during the transformation process.

## APPENDIX

### A. FLUX CALIBRATION & ILLUMINATION CORRECTION

The flux calibrations were determined by comparing sources in the field-of-view to the entries in the 2MASS and UKIDSS catalogs (which did not show systematic offsets when transformed to the same photometric system). Additionally, we compared the galaxy photometry in circular apertures of 5, 7, 10, 15, and 20 arcsecs. The 2MASS values were taken directly from the extended source catalog, and the zeropoints obtained with the galaxy photometry are consistent with the stellar comparisons for the brightest galaxies. For fainter galaxies, both the scatter increases, and an increasing systematic offset due to the shallow image depth of 2MASS is found. The UKIDSS pipeline reduction has apparently a problem with the sky subtraction, since the galaxy photometry is clearly offset from the stellar photometry, and this offset increases systematically with larger galaxy apertures. The

situation has slightly improved, when determining the sky as a median of the pixel values after masking sources, instead of using the pipeline-provided value. However, a significant systematic offsets of the zeropoints in comparison to those obtained with the stars or 2MASS galaxy aperture values remains, including the systematic trend with the apertures size.

Therefore, we decided to use the stellar photometry for the calibration using both 2MASS and UKIDSS stars. UKIDSS is a bit deeper and the photometry of fainter stars is still reliable. However, the UKIDSS Virgo coverage is incomplete (and for some stars the combination offers multiple measurements, which decreases statistical uncertainties and makes the comparison less sensitive to systematic brightness variations). Each object was measured within an aperture appropriate to the FWHM of the PSF, and several apertures of sizes increased or decreased in steps of one pixel were used to assess the stability of the measurement against variations in the aperture size.

For the zeropoint determination the objects are required *(i)* to have a brightness fainter than  $m > 11$  mag in order to stay in the linear regime of the detectors. *(ii)* The uncertainty of the comparison needs to be small, which effectively introduces a lower brightness limit for the comparison objects. Furthermore, we exclude objects, *(iii)* for which the different aperture values are not consistent with each other, *(iv)* for which the star probability as given by SExtractor is smaller than 85%, *(v)* which are clipped away by a lower clipping 0.2 mag below the score at 75%,  $ZP_{75} - 0.2$  mag, or *(vi)* at a subsequent  $2.33 \sigma$ -clipping. The final zeropoint is calculated as the weighted average of the remaining comparison objects. The median value of the uncertainty is of the order of 2%, to first order independent of the airmass and the conditions of the observation. The errors are comparable to those quoted for the traditional method of observing standard stars (de Jong 1996; Gavazzi et al. 1996; MacArthur, Courteau, & Holtzman 2003), and similar to the uncertainties determined by McDonald et al. (2011) via Monte-Carlo simulations for their similar calibration method for a typical number of more than 10 comparison objects. We saw that this calibration accuracy is achieved only if the illumination corrections for two of the three detectors are taken into account, the coaddition process does not involve any  $\sigma$  clipping (see §2.3.4), and the photometry of the comparison objects relies on our sky subtraction instead of a local determination.

The illumination correction is illustrated in Fig. A2. It is derived from the brightness variation of a standard star across the field of view (*upper panels*) using aperture photometry. The standard star observations were done for TNG and NOT in 2012. For NTT we did not observe standard stars for that purpose. For the 13 galaxies observed with NTT (and for the archival data from NTT) no illumination correction was applied. However, archival illumination correction frames from ESO show that the illumination corrections for NTT are significantly smaller, only a few percent for the extremes. The illumination corrections might show long term evolutions. Therefore, we compare surfaces fitted to the variations to those determined on stars in the field of view in the science frames of two photometric nights two years earlier *lower panels*. These measurements are a lot noisier, but qualitatively follow the same patterns.

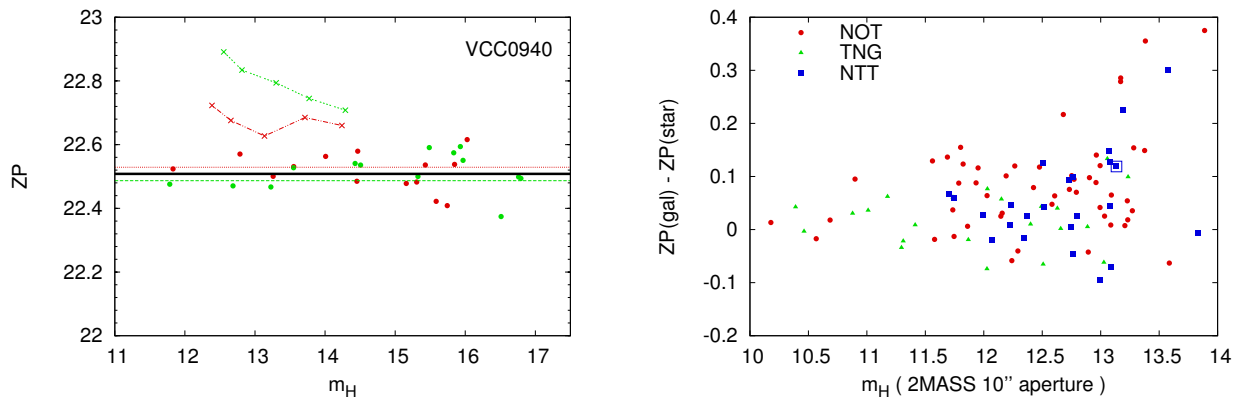


**Figure A1.** *Left panel:* Example for the zeropoint determination by comparison of point sources to 2MASS (red) and UKIDSS (green) brightnesses, shown for VCC0940. The points are the individual stars, while the crosses mark the zeropoints obtained from galaxy aperture photometry for comparison. The 2MASS galaxy measurements show a rather constant systematic offset for all apertures, while the UKIDSS values show an offset that systematically depends on the aperture size. The scatter of the zeropoints determined with the stars is 0.064 mag and the resulting formal error 0.012 mag. *Right panel:* Comparison between the star and galaxy aperture values for 2MASS, showing a systematic trend of larger offsets for fainter galaxies and the increasing galaxy aperture uncertainty. The highlighted point shows the field of VCC0940, which is shown in the left panel.

## B. FURTHER QUANTIFICATION OF FIT QUALITY

GALFIT uses the  $\chi^2$  in the fitting process. Therefore, we compare the  $\chi^2$  after fitting a simple model (single Sérsic + possible nucleus) to one-component and complex galaxies. We restrict the calculation of the  $\chi^2$  to an elliptical aperture with a SMA of  $1.5 r_e$ . At large radii both the model and the galaxy approach flux values of 0 and the signature of enhanced  $\chi^2$  can be diluted. The distributions of  $\chi^2$  for one-component and complex galaxies are different: 75% of the one-component galaxies have reduced  $\chi^2 < 1.1$ , while 65% of the complex galaxies have reduced  $\chi^2 > 1.1$ . Note that, a galaxy with spiral arms has an enhanced  $\chi^2$ , but is not necessarily significantly better fitted with a more complex model. If the improvement is marginal, we were satisfied with the simple model. However, the  $\chi^2$  is not an optimal measure of the quality of two-dimensional fits (e.g. Andrae, Schulze-Hartung,

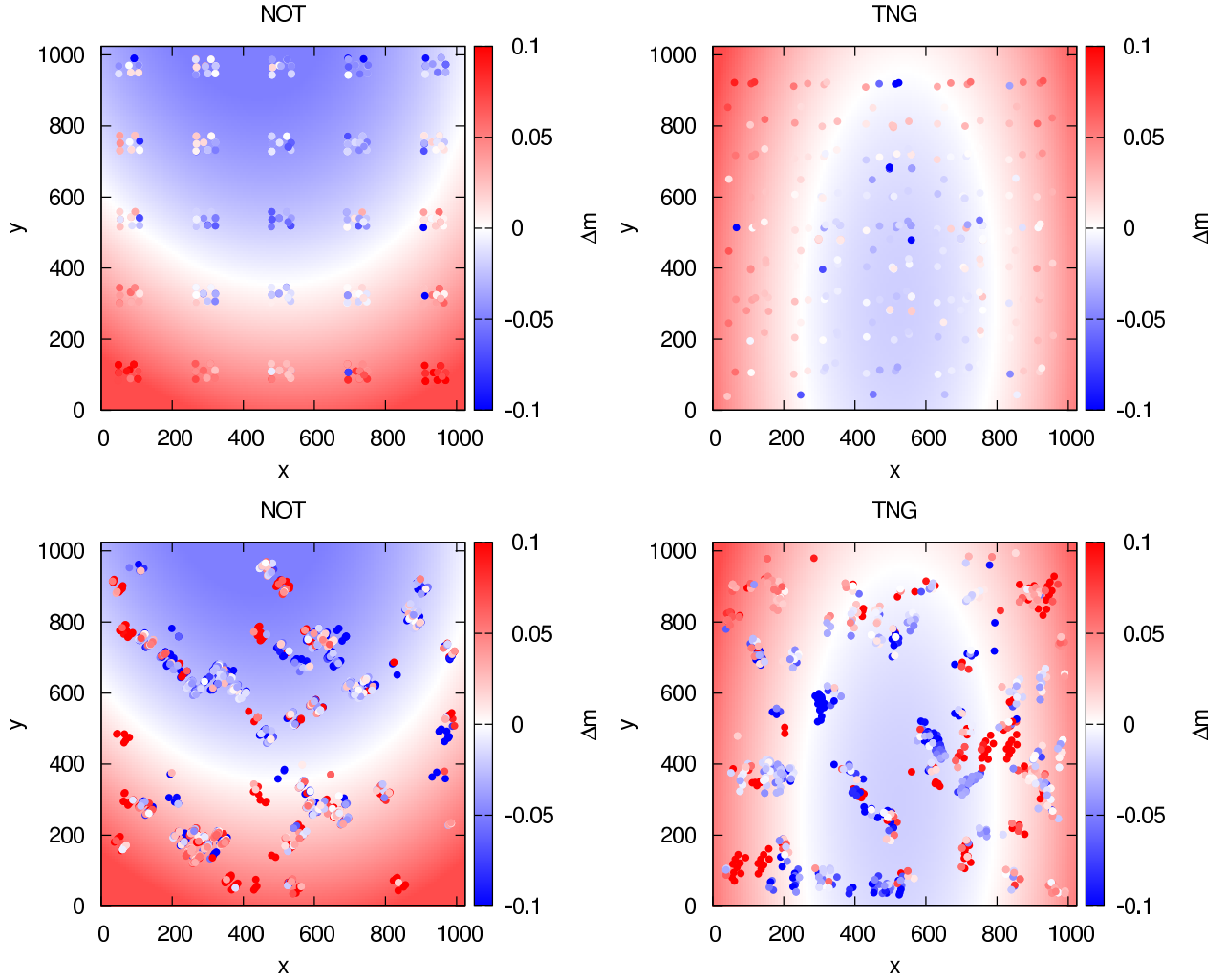


**Figure A2.** Variations of the brightness of stars measured across the field of view. The *upper panels* display the dedicated standard star measurements in 2012. The background color shows the fitted surface. The *lower panels* show the same surface and on top the measurements of stars in the science frames of two photometric nights in 2010. The *left and right panels* show the data for NOTCam and NICS, respectively.

& Melchior 2010).

Therefore, we use two other quantifications. The result of using the RFF and EVI indices were described in Section §3.4.3. Furthermore, we also calculate the tessellated excess residuals: the galaxy image is divided from a SMA of 10 pixel to the outermost isophote into 9 elliptical rings. Each of these rings we subdivide into 32 sectors. In these patches the mean residual in units of the noise is calculated:

$$R = \sum_i^{N_{\text{pix}}} \frac{(O_i - M_i)}{\sigma_i}, \quad (\text{B1})$$

with the observation  $O$ , the model  $M$ , the  $\sigma$ -image  $\sigma$  and summing over all unmasked pixels. If  $|R| > 1/\sqrt{N_{\text{pix}}}$  we consider this patch to be not well modeled, since on average the pixels deviate more than expected. Subsequently, we calculate the area of the galaxy for which this criterion is met:

$$A = \left( \sum_{\text{failed patches}} N_{\text{pix}} \right) / \left( \sum_{\text{all patches}} N_{\text{pix}} \right). \quad (\text{B2})$$

The obtained quantity measures how much of the galaxy a model can reproduce in terms of the solid angle. In the left panel of Fig. B1 we show a histogram of the fraction of a galaxy that is not well modeled by a simple model for simple and complex galaxies. The right panel indicates the improvement for the complex galaxies in the final model.

Both quantifications agree with our visual choices reasonably well. However, for a few individual galaxies, the parameters might argue in favor of a different model.

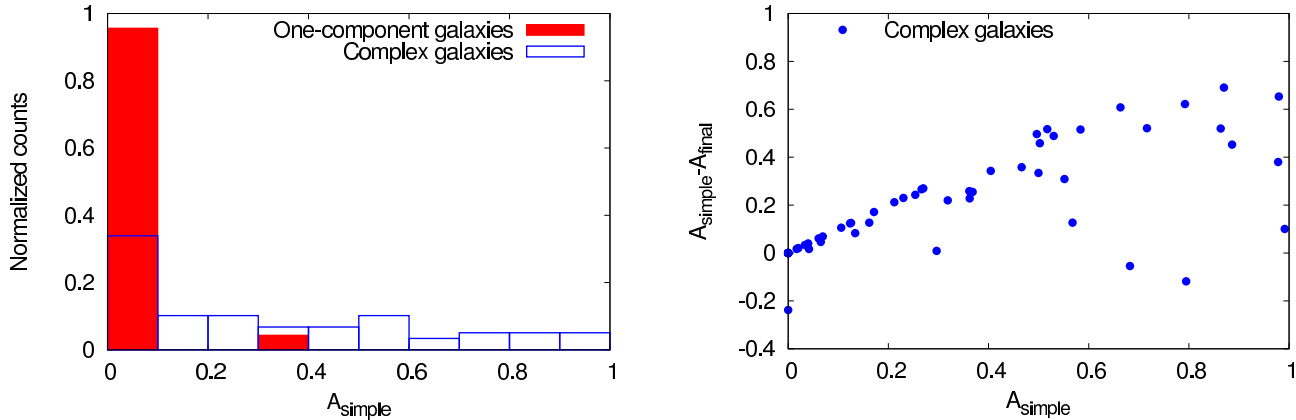


**Figure B1.** *Left panel:* Normalized histogram for the fractions of area that is not well modeled by a simple model for one-component and complex galaxies. *Right panel:* Improvement of the final model compared to a simple model versus the fraction of the galaxy that is not well reproduced in the simple model.

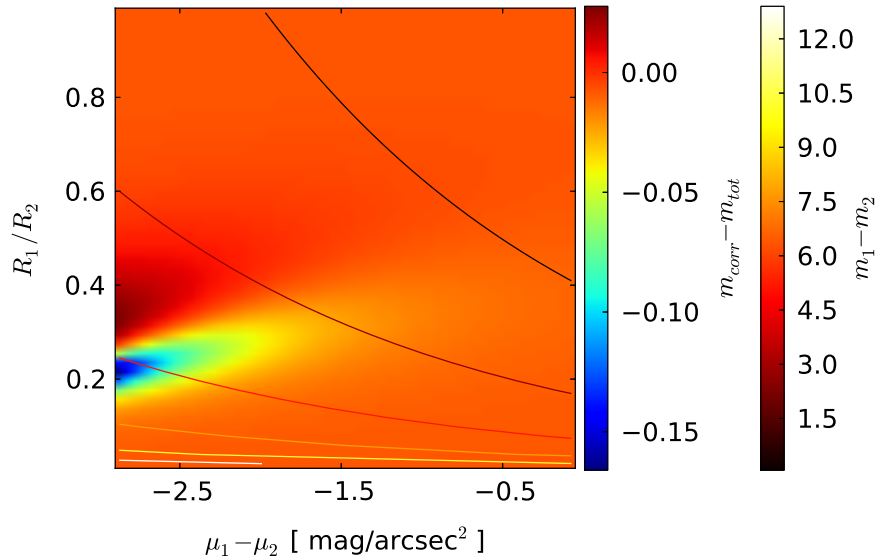


**Figure C1.** The error of the total brightnesses (colors, color bar in the middle), if the profiles do not follow Sérsic functions, but two exponentials, is shown as a function of the ratio of scale lengths of the two components and their difference of surface brightness at  $r_e$ . The lines indicate the difference in brightness of the two components (right color bar).

### C. NOTES ON SÉRSIC PROFILES & CONCENTRATIONS

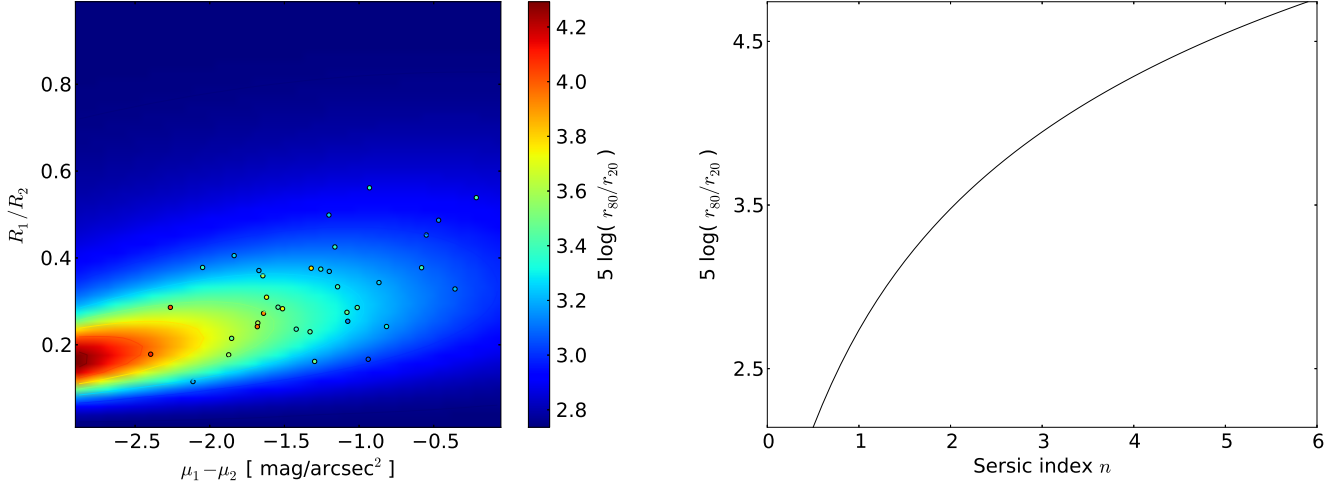
The non-parametric photometry uses concentration measurement to calculate the correction for missed flux outside the apertures of two Petrosian radii. This implicitly assumes that the profile follows a Sérsic function. If the profile is instead a superposition of two functions, there will be a small error introduced. In Fig. C1 this error for a superposition of two exponential functions is shown as a function of the ratio of their effective radii and the difference of their surface brightnesses at  $r_e$ . For most of the galaxies the introduced error is below 0.05 mag. If there is a bright inner component with a smaller size, the concentration increases (Fig. C2, left panel). The high concentration corresponds to a large Sérsic index  $n$  (Fig. C2, right panel, see also Graham & Driver 2005), which makes the assumed correction large, even though it should be small for the superposition of two exponentials. That can be seen as the feature in the lower left corner in Fig. C1.

Fig. C3 shows that the complex galaxies have higher concentrations. The fraction of one-component galaxies decreases and there is a trend of increasing concentration towards higher brightness

### D. FIGURES WITH LOCAL PROJECTED GALAXY DENSITY INSTEAD OF CLUSTERCENTRIC DISTANCE, AND WITH EFFECTIVE SURFACE BRIGHTNESS INSTEAD OF BRIGHTNESS

In Fig. D1 local projected galaxy density is shown as a measure of the local environment, alternatively to the clustercentric distance. The local projected galaxy number density at the position of a given galaxy is computed from the circular projected area  $A$  centered on that position and encompassing 10 neighbor galaxies brighter than  $M_r \leq -15.2$  mag (the  $r$ -magnitude completeness limit of the VCC, see Weinmann et al. 2011). Known background galaxies as well as likely members of the more distant M- and W-clouds (Gavazzi et al. 1999) are excluded. The resulting density is  $11/A$  in units of number per square degree.





**Figure C2.** The galaxy concentration (color) is shown as a function of the ratio of scale lengths of the two components and their difference of surface brightness at  $r_e$ . The points are the observed two-component galaxies. *Right panel:* in the case of a single Sérsic function, there is a one-to-one relation of Sérsic  $n$  and the concentration.

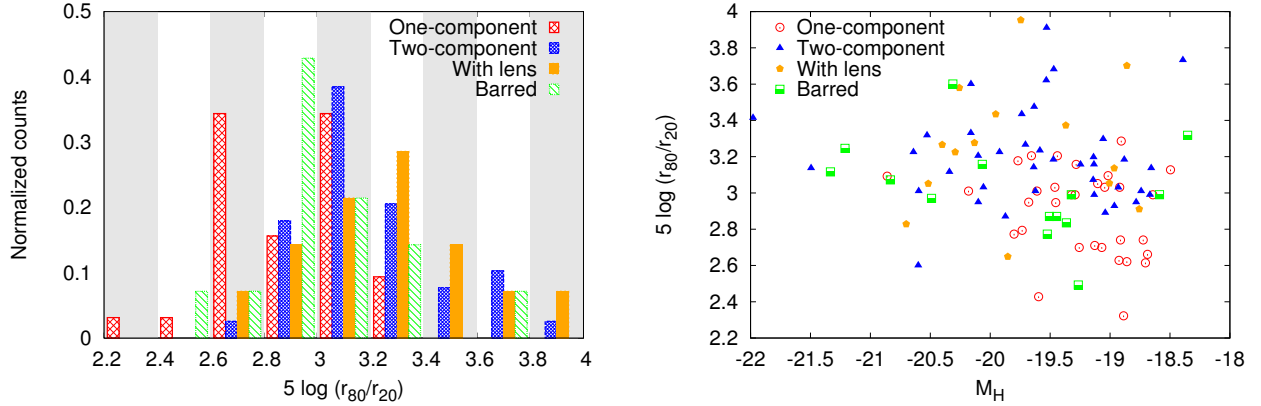


**Figure C3.** *Left panel:* histogram of concentrations normalized to the numbers of galaxies in the groups. *Right panel:* galaxy concentration as a function of galaxy brightness.

In Figs. D2&D3 the photometric scaling relations are shown with surface brightness instead of brightness. In Fig. D2 the Kormendy relation is shown for the whole galaxies, the data for the bright galaxies is taken from the 2MASS extended source catalog. Fig. D3 shows the scalings of the components in comparison to those of the galaxies in NIRS0S and OSUBSGS.

### E. COMPARISON TO MCDONALD ET AL. (2011) PROFILE FITS

McDonald et al. (2011) also studied galaxies in the Virgo cluster, and there is a substantial overlap of 88 galaxies with this study, as indicated in Table 3. They fitted the azimuthally averaged light profiles with one- or two-component models, possibly including an additional nucleus. We first list the main differences between the two studies, which may be responsible for the differences in the type of model chosen for individual galaxies (Janz et al. 2012), and subsequently compare parameters of models for galaxies that are fitted with similar models in both studies.

McDonald et al. adopt Sérsic+exponential models for two-component galaxies, as mostly done also in this study, but all their single component galaxies have exactly exponential profiles. This is a major restriction for the available parameter space for single component galaxies in comparison to this study. Furthermore, they employ an automated one-dimensional fitting algorithm, while our visual model selection makes use of all the available information, and is deliberated by subjective human minds. Also, two of our structural types, galaxies with bars and lenses, are not part of their model variety. Finally, the studies are based on different data sets.

McDonald et al.'s published light profiles extend to similar radii as in this study for 30 of the 88 galaxies in both samples, when requiring a similar surface brightness error at the outermost radii. For only two galaxies their data reach larger radii (VCC 1087 and 1549), while for the 56 remaining galaxies our images are deeper. The profiles of 14 of the galaxies with comparable radial extent show good agreement<sup>17</sup>, while 16 galaxies show differences in their profiles between the two studies<sup>18</sup>. For all but

<sup>17</sup> VCC 0523, 0856, 0917, 0951, 1036, 1183, 1261, 1431, 1491, 1499, 1545, 1695, 1871, and 1895.

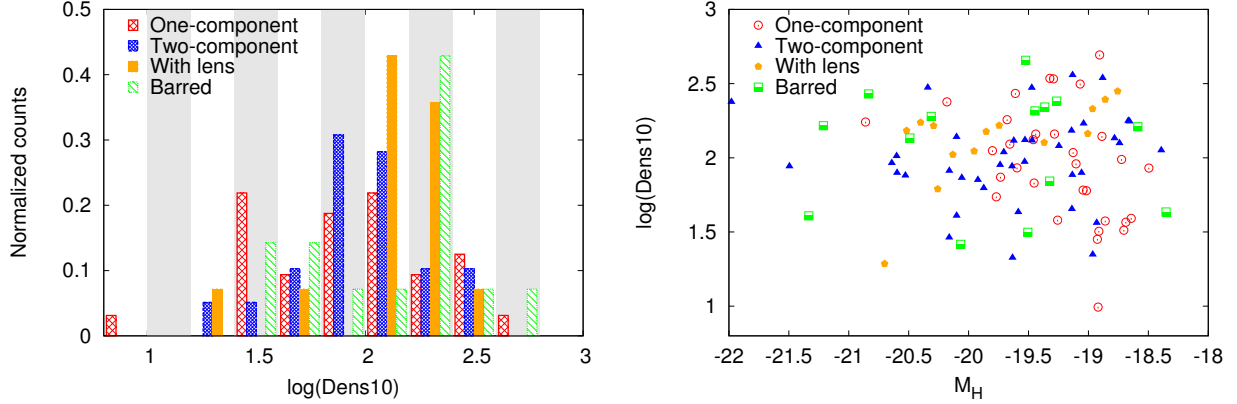


**Figure D1.** *Left panel:* Histogram of local galaxy density normalized by the number of galaxies in the groups. *Right panel:* Local galaxy density versus galaxy brightness.

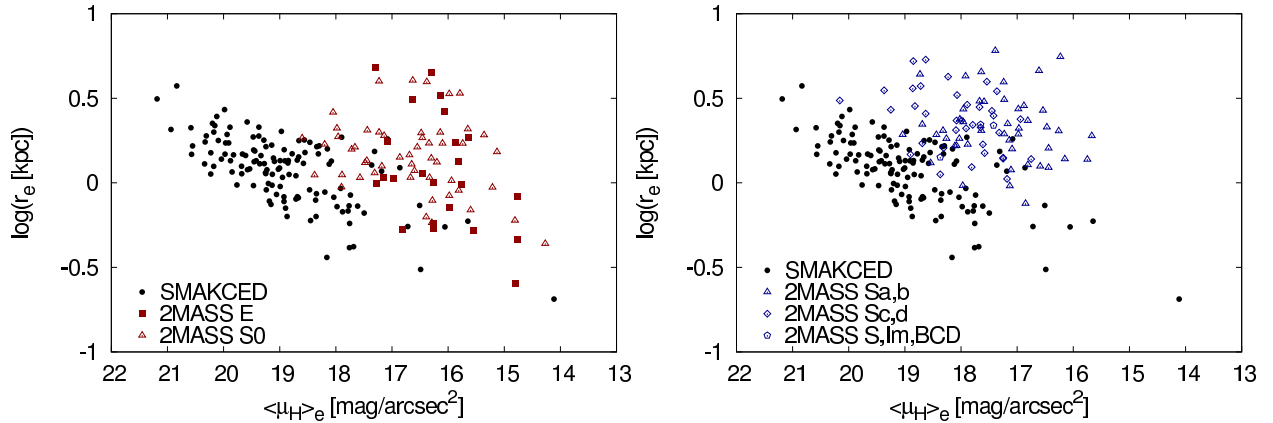


**Figure D2.** Same as Fig. 9, but showing the Kormendy relation instead of size versus brightness, both measured for the whole galaxy.

two of the deviant profiles, the McDonald et al. surface brightnesses are brighter at larger radii, and for at least six of those <sup>19</sup>, they show a visible break in the profile that is not present in our data. Several times this is accompanied with discrepancies of the profile in comparison to their optical SDSS profiles that go beyond a normal color gradient. Our profiles are displayed on our dedicated galaxy decomposition webpages, <http://www.smakced.net/data.html>, where links to the near-IR as well as the optical profiles of McDonald et al. (2011) are also provided.

In Fig. E1 we compare the decomposition parameters of this study (SMAKCED) to those determined by McDonald et al.. The comparison is restricted to galaxies that have comparable decompositions, i.e. galaxies that are fitted with one Sérsic function or two-component models in both studies. Also, galaxies with a less reliable fit in McDonald et al. and galaxies, for which the total magnitudes differ between the two studies, are omitted. As expected (see §3.4) the obtained parameters show a reasonable agreement.

#### F. GALFIT VS. BDBAR FOR NIRS0S GALAXIES AND SMAKCED

The original NIRS0S and OSUBSGS decompositions were done with BDBAR (Laurikainen et al. 2004). Moreover, instead of using  $\sigma$ -images as done in GALFIT, a weighting  $w = 1/F_{\text{model}}$  was used in BDBAR ( $F_{\text{model}}$  = flux of the pixel in the model). For an ideal model the weighting should not make a difference. However, in a real galaxy there are anomalies, or parts are not perfectly modeled. Therefore, a different weighting can bias the resulting fit parameters, though the effect is not expected to be large (Laurikainen et al. 2005). We rerun the NIRS0S decompositions with GALFIT. Since the automatic decompositions can not be used blindly for the comparison, we selected some of those galaxies, for which the same features in the data were fitted. The parameters derived with BDBAR and GALFIT are compared in Fig. F1. The scatter is reasonably small and no severe systematic bias is introduced. There are three outliers for the sizes of the components. This can happen, if there are only a few pixels for fitting the bulge and the resulting fit has an unreasonably high Sérsic index. In a manual decomposition one tries to avoid such pathological behavior.

<sup>18</sup> VCC 0437, 0543, 0698, 0751, 1283, 1392, 1422, 1512, 1528, 1567, 1614, 1627, 1743, 1910, 1945, and 2042.

<sup>19</sup> VCC 0437, 1567, 1614, 1743, 1910, and 1945.

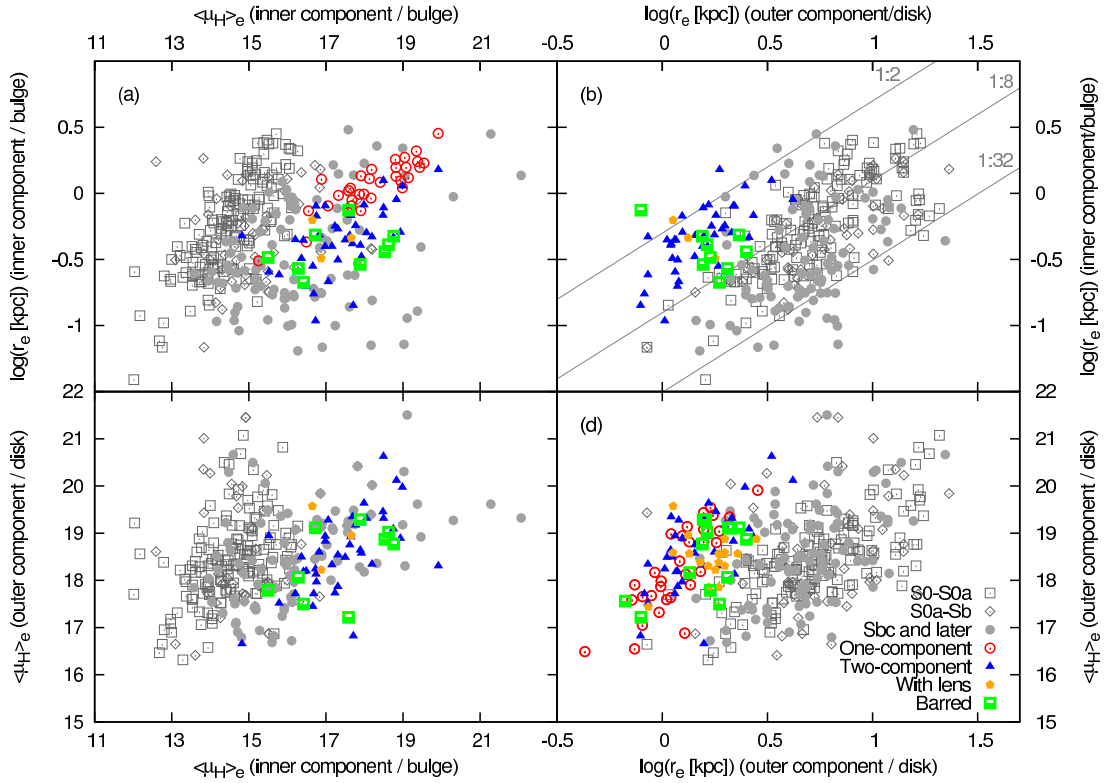


**Figure D3.** Same as Fig. 14, but showing the comparison to the NIRS0S and OSUBSGS with surface brightness instead of brightness; all quantities are measured for the individual components.

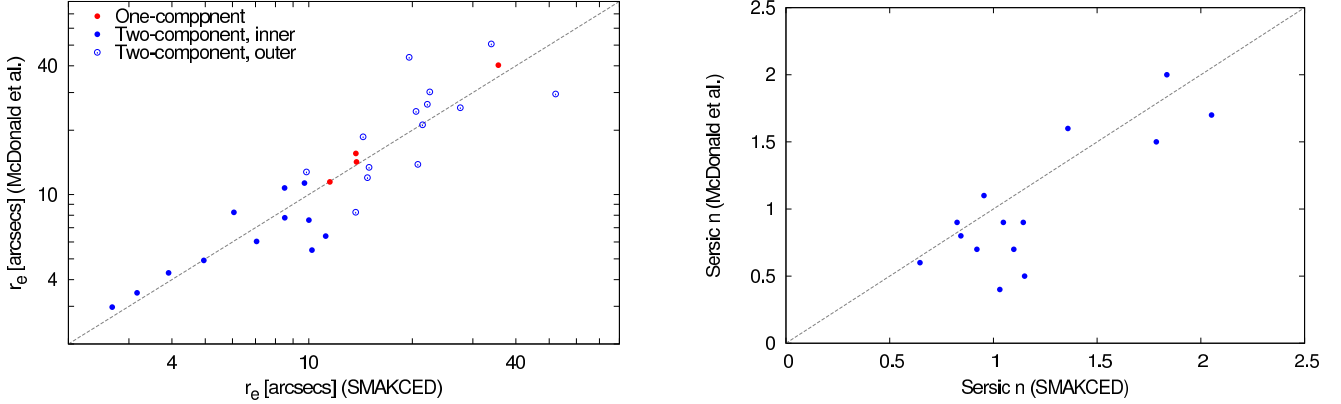


**Figure E1.** Comparison to the profile fits of McDonald et al. (2011). Shown are galaxies that were characterized in both studies with a one-component (red points) or two-component model (blue symbols, filled and open symbols for inner and outer components, respectively). Galaxies with a poorer quality flag for the fit in McDonald et al. are omitted, as well as galaxies with profile discrepancies (see text). The left and right panel show the radii and Sérsic indices, respectively. A generally good agreement is found.

The observations of this publication are based on proposals of the SMAKCED team (<http://www.smakced.net>).

We thank the referee for valuable comments that led to improvements of the paper. Furthermore, we thank A. Pasquali for useful discussions concerning the boxiness; as well as J. Laine and E. Busekool for help with the observations.

J.J. acknowledges the financial support of the Gottfried Daimler- and Karl Benz Foundation and the University of Oulu. J.J., T.L., K.S.A.H., H.T.M., and S.P. were supported within the framework of the Excellence Initiative by the German Research Foundation (DFG) through the Heidelberg Graduate School of Fundamental Physics (grant number GSC 129/1), by the DFG through grants LI 1801/2-1 (H.T.M.) and LI 1801/7-1 (K.S.A.H.), and by the IMPRS for Astronomy and Cosmic Physics at the University of Heidelberg (K.S.A.H. and S.P.). J.J. and H.S. acknowledge the support by the Academy of Finland. E.T. thanks the financial support of the Fulbright Program jointly with the Spanish Ministry of Education. J.F.-B. acknowledges support from the Ramón y Cajal Program and from grant AYA2010-21322-C03-02 by the Spanish Ministry of Science and Innovation, as well as financial support to the DAGAL network from the People Programme (Marie Curie Actions) of the European Union's Seventh Framework Programme FP7/2007-2013/ under REA grant agreement number PITN-GA-2011-289313. K.S.A.H. acknowledges

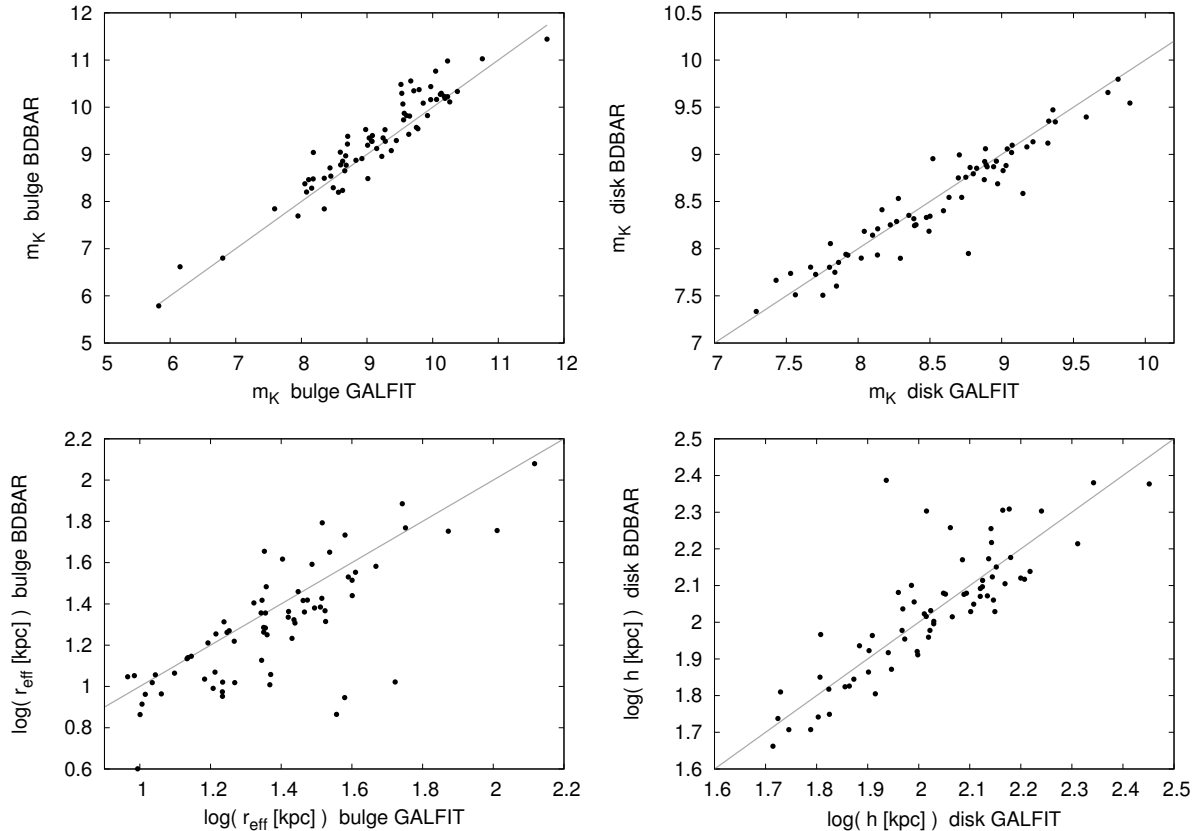


**Figure F1.** This figure compares the BDBAR and GALFIT decomposition parameters for NIRS0S: the brightnesses (*upper panels*) and the scale parameters (*lower panels*) for the bulge (*left*) and the disk (*right*) are shown. The agreement in this GALFIT/BDBAR comparison would be even better if barlenses, that form part of the bar, would have been fitted in our GALFIT decompositions, in a similar manner as in LAURIKAINEN:2010P4602 using BDBAR.

funding from the University of Heidelberg through a Landesgraduiertenförderung (LGFG) fellowship for doctoral training.

Based on observations made with the Italian Telescopio Nazionale Galileo (TNG) operated on the island of La Palma by the Fundación Galileo Galilei of the INAF (Istituto Nazionale di Astrofisica) at the Spanish Observatorio del Roque de los Muchachos of the Instituto de Astrofisica de Canarias.

Based on observations made with the Nordic Optical Telescope, operated on the island of La Palma jointly by Denmark, Finland, Iceland, Norway, and Sweden, in the Spanish Observatorio del Roque de los Muchachos of the Instituto de Astrofisica de Canarias.

This publication makes use of data products from the Two Micron All Sky Survey, which is a joint project of the University of Massachusetts and the Infrared Processing and Analysis Center/California Institute of Technology, funded by the National Aeronautics and Space Administration and the National Science Foundation.

This work is based in part on data obtained as part of the UKIRT Infrared Deep Sky Survey.

Funding for SDSS-III has been provided by the Alfred P. Sloan Foundation, the Participating Institutions, the National Science Foundation, and the U.S. Department of Energy Office of Science. The SDSS-III web site is <http://www.sdss3.org/>. SDSS-III is managed by the Astrophysical Research Consortium for the Participating Institutions of the SDSS-III Collaboration including the University of Arizona, the Brazilian Participation Group, Brookhaven National Laboratory, University of Cambridge, Carnegie Mellon University, University of Florida, the French Participation Group, the German Participation Group, Harvard University, the Instituto de Astrofisica de Canarias, the Michigan State/Notre Dame/JINA Participation Group, Johns Hopkins University, Lawrence Berkeley National Laboratory, Max Planck Institute for Astrophysics, Max Planck Institute for Extraterrestrial Physics, New Mexico State University, New York University, Ohio State University, Pennsylvania State University, University of Portsmouth, Princeton University, the Spanish Participation Group, University of Tokyo, University of Utah, Vanderbilt University, University of Virginia, University of Washington, and Yale University.

This research has made use of the NASA/IPAC Extragalactic Database (NED) which is operated by the Jet Propulsion Laboratory, California Institute of Technology, under contract with the National Aeronautics and Space Administration.



## REFERENCES

- Abraham, R. G., Valdes, F., Yee, H. K. C., & van den Bergh, S. 1994, *ApJ*, 432, 75
- Aguerri, J. A. L., Iglesias-Páramo, J., Vílchez, J. M., Muñoz-Tuñón, C., & Sánchez-Janssen, R. 2005, *AJ*, 130, 475
- Aihara, H., et al., 2011, *ApJS*, 193, 1
- Allen, P. D., et al. 2006, *MNRAS*, 371, 2
- Andersen, V. 1996, *AJ*, 111, 1805
- Andrae R., Schulze-Hartung T., & Melchior P. 2010, arXiv:1012.3754
- Barazza, F. D., Binggeli, B., & Jerjen, H. 2002, *A&A*, 391, 823
- Barazza, F. D., Binggeli, B., & Jerjen, H. 2003, *A&A*, 407, 121
- Barazza, F. D., et al. 2009, *A&A*, 497, 713
- Bell, E. F., & de Jong, R. S. 2001, *ApJ*, 550, 212
- Bender, R. 1988, *A&A*, 193, 107
- Bender, R., Surma, P., Doebereiner, S., Moellenhoff, C., & Madejsky, R. 1989, *A&A*, 217, 35
- Bekki, K. & Couch, W. J. 2003, *ApJ*, 596, L13
- Bershady, M. A., Jangren, A., & Conselice, C. J. 2000, *AJ*, 119, 2645
- Bertin, E. & Arnouts, S. 1996, *A&A Supplement* 317, 393
- Binggeli, B., & Cameron, L. M. 1991, *A&A*, 252, 27
- Binggeli, B., Sandage, A., & Tammann, G. A. 1985, *AJ*, 90, 1681
- Binggeli, B. & Popescu, C. C. 1995, *A&A*, 298, 63
- Binney, J., & Tremaine, S. 1987, *Galactic dynamics* (Princeton, NJ: Princeton University Press, 1987
- Blakeslee, J., et al. 2006, *ApJ*, 644, 30
- Boselli, A., Boissier, S., Cortese, L., & Gavazzi, G. 2008, *A&A*, 489, 1015
- Boselli, A., Boissier, S., Cortese, L., & Gavazzi, G. 2008, *ApJ*, 674, 742
- Boselli, A., & Gavazzi, G. 2006, *PASP*, 118, 517
- Byun, Y. I., & Freeman, K. C. 1995, *ApJ*, 448, 563
- Caon, N., Capaccioli, M., D'Onofrio, M., & Longo, G. 1994, *A&A*, 286, L39
- Caon, N., Capaccioli, M., & D'Onofrio, M. 1993, *MNRAS*, 265, 1013
- Capaccioli, M. 1989, in *The World of Galaxies*, ed. H. G. Corwin, L. Bottinelli (Berlin: Springer-Verlag), 208
- Cappellari, M., et al. 2011, *MNRAS*, 416, 1680
- Carter, D. 1978, *MNRAS*, 182, 797
- Ciotti, L. 1991, *A&A*, 249, 99
- Chen, C.-W., Côté, P., West, A. A., Peng, E. W., & Ferrarese, L. 2010, *ApJS*, 191, 1
- Chilingarian, I. V. 2009, *MNRAS*, 394, 1229
- Conselice, C. J., Gallagher, J. S., III, & Wyse, R. F. G. 2002, *AJ*, 123, 2246
- Conselice, C. J. 2003, *ApJS*, 147, 1
- Conselice, C. J., et al. 2003, *AJ*, 125, 66
- Côté, P., et al. 2006, *ApJS*, 165, 57
- Côté, P., et al. 2007, *ApJ*, 671, 1456
- Courteau, S., de Jong, R. S., & Broeils, A. H. 1996, *ApJ*, 457, 73
- Dehnen W., & Binney J. J., 1998, *MNRAS*, 298, 387
- de Grijs, R. 1998, *MNRAS*, 299, 595
- de Jong, R. S., 1996, *A&A*, 313, 45
- de Jong, R. S., et al. 2004, *MNRAS*, 355, 1155
- de Looze, I., et al. 2010, *A&A*, 518, 54
- De Lucia, G., Fontanot, F., & Wilman, D. 2012, *MNRAS*, 419, 1324
- de Rijcke, S., Dejonghe, H., Zeilinger, W. W., & Hau, G. K. T. 2003, *A&A*, 400, 119
- de Rijcke, S., Michielsen, D., Dejonghe, H., Zeilinger, W. W., & Hau, G. K. T. 2005, *A&A*, 438, 491
- de Rijcke, S., van Hese, E., & Buyle, P. 2010, *ApJ*, 724, L171
- de Vaucouleurs, G., de Vaucouleurs, A., Corwin, H. G., Buta, R., Paturel, G., & Fouqué, P. 1991, *Third Reference Catalogue of Bright Galaxies*, New York, Springer (RC3)
- Dressler, A. 1980, *ApJ*, 236, 351
- Fisher, D. B., & Drory, N. 2008, *AJ*, 136, 773
- Eskridge, P. B., et al. 2002, *ApJS*, 143, 73
- Emsellem, E., et al. 2011, *MNRAS*, 414, 888
- Falcón-Barroso, J., et al. 2011, *MNRAS*, 417, 1787
- Ferrarese, L., et al. 2006, *ApJS*, 164, 334
- Ferguson, H. C., & Binggeli, B. 1994, *A&ARv*, 6, 67
- Ferguson, H. C., & Sandage, A. 1989, *ApJ*, 346, L53
- Gadotti, D. A. 2008, *MNRAS*, 384, 420
- Gavazzi, G., Boselli, A., Scodreggio, M., Pierini, D., & Belsole, E. 1999, *MNRAS*, 304, 595
- Gavazzi G., et al. 1996, *A&AS*, 120, 521
- Gavazzi, G., Zibetti, S., Boselli, A., Franzetti, P., Scodreggio, M., & Martocchi, S. 2001, *A&A*, 372, 29
- Gerssen, G., & Shapiro Griffin, K. 2012, *MNRAS*, 423, 2726
- Graham, A. W. 2002, *ApJ*, 568, L13
- Graham, A. W. 2011, arXiv:1108.0997
- Graham, A. W., & Driver, S. P. 2005, *PASA*, 22, 118
- Graham, A. W., et al. 2012, *ApJ*, 750, 121
- Graham, A. W., et al. 2005, *AJ*, 130, 1535
- Graham, A. W., & Guzmán, R. 2003, *AJ*, 125, 2936
- Graham, A. W., Worley, C. C., 2008, *MNRAS*, 388, 1708
- Gnedin, O. Y. 2003, *ApJ*, 589, 752
- Gunn, J. E., & Gott, J. R. III 1972, *ApJ*, 176, 1
- Guo, Q., et al. 2011, *MNRAS*, 413, 101
- Hallenbeck, G., et al. 2012, *AJ*, 144, 87
- Hewett, P. C., Warren, S. J., Leggett, S. K., & Hodgkin, S. T. 2006, *MNRAS*, 367, 454
- Hirata, C., & Seljak, U. 2003, *MNRAS*, 343, 459
- Hodgkin, S. T., Irwin, M. J., Hewett, P. C., Warren, S. J., 2009, *MNRAS*, 394, 675
- Hoyos, C., et al. 2011, *MNRAS*, 411, 2439
- Huang, S., Ho, L. C., Peng, C. Y., Li, Z.-Y., & Barth, A. J. 2013, *ApJ*, 766, 47
- Huxor, A. P., Phillipps, S., Price, J., & Harniman, R. 2011, *MNRAS*, 414, 3557
- Janz, J., et al. 2012, *ApJ*, 745, L24
- Janz, J., & Lisker, T. 2008, *ApJ*, 689, L25
- . 2009, *ApJ*, 696, L102
- Jerjen, H., Kalnajs, A., & Binggeli, B. 2000, *A&A*, 358, 845
- Kaufmann, T., Wheeler, C., & Bullock, J. S. 2007, *MNRAS*, 382, 1187
- King, I. R. 1966, *AJ*, 71, 64
- Koleva, M., Prugniel, P., de Rijcke, S., & Zeilinger, W. W. 2011, *MNRAS*, 417, 1643
- Kormendy, J. 1977, *ApJ*, 218, 333
- Kormendy, J. 1979, *ApJ*, 227, 714
- Kormendy, J. 1985, *ApJ*, 295, 73
- Kormendy, J., & Bender, R. 2012, *ApJS*, 2012, 198, 2
- Kormendy, J., Fisher, D. B., Cornell, M. E., & Bender, R. 2009, *ApJS*, 182, 216
- Kormendy, J. & Kennicutt Jr., R. C. 2004, *ARA&A*, 42, 603
- Krajinović, D., et al. 2011, *MNRAS*, 414, 2923
- Kuijken, K., & Dubinski, J. 1995, *MNRAS*, 277, 1341
- Lauer, T. R., et al. 1996, *ApJ*, 471, L79
- Laurikainen, E., Salo, H., Buta, R., & Vasylyev, S. 2004, *MNRAS*, 355, 1251
- Laurikainen, E., Salo, H., & Buta, R. 2005, *MNRAS*, 362, 1319
- Laurikainen, E., et al. 2006, *AJ*, 132, 2634
- Laurikainen, E., Salo, H., Buta, R., & Knapen, J. H. 2009, *ApJ*, 692, L34
- Laurikainen, E., Salo, H., Buta, R., Knapen, J. H., & Comerón, S. 2010, *MNRAS*, 405, 1089
- Laurikainen, E., Salo, H., Buta, R., & Knapen, J. H. 2011, *MNRAS*, 418, 1452
- Laurikainen, E. et al. 2013, *MNRAS*, 430, 3489
- Laurikainen, E. & Salo, H. 2001, *MNRAS*, 324, 685
- Lawrence, A., et al. 2006, *MNRAS*, 379, 1599
- Lisker, T. 2009, *AN* 330, 1043
- Lisker, T., Brunngräber, R., & Grebel, E. K. 2009, *AN* 330, 966
- Lisker, T., & Fuchs, B., *A&A*, 501, 429
- Lisker, T., Glatt, K., Westera, P., & Grebel, E. K. 2006a, *AJ*, 132, 2432
- Lisker, T., Grebel, E. K., & Binggeli, B. 2006b, *AJ*, 132, 497
- . 2008, *AJ*, 135, 380
- Lisker, T., Grebel, E. K., Binggeli, B., & Glatt, K. 2007, *ApJ*, 660, 1186
- Lisker, T., et al. 2009, *ApJ*, 706, L124
- Lisker, T., Weinmann, S. M., Janz, J., & Meyer, H. T. 2013, *MNRAS*, in press, arXiv:1303.0928
- Lotz, J. M., Primack, J., & Madau, P. 2004, *AJ*, 128, 163
- MacArthur, L. A., Courteau S., & Holtzman J. A. 2003, *ApJ*, 582, 689
- Marinova, I., et al. 2012, *ApJ*, 746, 136
- Martinez-Delgado, D., et al. 2012, *ApJ*, 748, L24
- Mastropietro, C., et al. 2005, *MNRAS*, 364, 607
- McDonald, M., Courteau, S., Tully, R. B., & Roediger, J. 2011, *MNRAS*, 414, 2055
- Mei, S., et al. 2007, *ApJ*, 655, 144
- Méndez-Abreu, J., Sánchez-Janssen, R., Aguerri, J. A. L. 2010, *ApJ*, 711, L61
- Méndez-Abreu, J., Simonneau, E., Aguerri, J. A. L., & Corsini, E. M. 2010, *A&A*, 521, 71
- Meyer, H. T., Lisker, T., Janz, J., & Papaderos, P. 2013, *A&A*, submitted
- Michielsen, D., et al. 2008, *MNRAS*, 385, 1374
- Mieske, S., Hilker, M., Infante, L., & Mendes de Oliveira, C. 2007, *A&A*, 463, 503
- Misgeld, I., Mieske, S., & Hilker, M. 2008, *A&A*, 486, 697
- Moore, B., Lake, G., & Katz, N. 1998, *ApJ*, 495, 139
- Navarro, J. F., Frenk, C. S., & White, S. M. 1997, *ApJ*, 490, 493
- Noordermeer, E., & van der Hulst, J. M. 2007, *MNRAS*, 376, 1480
- Pasquali, A., van den Bosch, F. C., & Rix, H.-W. 2007, *ApJ*, 664, 738
- Paudel, S., Lisker, T., Kuntschner, H., Grebel, E. K., & Glatt, K. 2010, *MNRAS*, 405, 800
- Pedraz, S., Gorgas, J., Cardiel, N., Sánchez-Blázquez, P., & Guzmán, R. 2002, *MNRAS*, 332, L59
- Peletier, R. F. 1993, *A&A*, 271, 51
- Peletier, R. F., et al. 1999, *MNRAS*, 310, 703
- Peng, C. Y., Ho, L. C., Impey, C. D., & Rix, H.-W. 2010, *AJ*, 139, 2097
- Peng, E. W., et al. 2008, *ApJ*, 681, 197
- Petrosian, V. 1976, *ApJ*, 209, L1
- Price, J., et al. 2009, *MNRAS*, 397, 1816
- Roediger, E. 2009, *AN*, 330, 888
- Ryś, A., Falcón-Barroso, J., & van de Ven, G. 2013, *MNRAS*, 428, 2980
- Sánchez-Janssen, R., & Aguerri, J. A. L. 2012, *MNRAS*, 424, 2614
- Sánchez-Janssen, R., Méndez-Abreu, J., & Aguerri, J. A. L. 2010, *MNRAS*, 406, L65
- Sandage, A., & Binggeli, B. 1984, *AJ*, 89, 919

- Scannapieco, C., White, S. D. M., Springel, V., & Tissera, P. B. 2011, MNRAS, 417, 154
- Schlegel, D. J., Finkbeiner, D. P., & Davis, M. 1998, ApJ, 500, 525
- Sérsic, J. L. 1963, Bol. Asoc. Argentina Astron. La Plata Argentina, 6, 41
- Shapiro K. L., Gerssen J., van der Marel R. P., 2003, AJ, 126, 2707
- Shlosman, I., Frank, J., & Begelman, M. C. 1989, Nature, 338, 45
- Shlosman, I., Begelman, M. C., & Frank, J. 1990, Nature, 345, 679
- Simien, F., & Prugniel, P. 2002, A&A, 384, 371
- Skrutskie, M. F., et al. 2006, AJ, 131, 1163
- Smith, R., Davis, J. I., & Nelson, A. H. 2010, MNRAS, 405, 1723
- Smith, R., Fellhauer, M., & Assmann, P. 2012a, MNRAS, 420, 1990
- Smith, R., Phillipps, S., Jones, J. B., Morris, R. A. H., Smith, R. M., Drinkwater, M. J., & Karick, A. M. 2012b, MNRAS, 420, 3412
- Smith, R., et al. 2013, MNRAS, 429, 1066
- Smith Castelli, A. V., et al. 2008, MNRAS, 386, 2311
- Smith Castelli, A. V., Faifer, F. R., Richtler, T., & Bassino, L. P. 2008, MNRAS, 391, 685
- Springel, V. 2005, MNRAS, 364, 1105
- Sung, E.-C., Han, C., Ryden, B. S., Chun, M.-S., & Kim, H.-I. 1998, ApJ, 499, 140
- Thompson, L. A. 1981, ApJ, 244, L43
- Tinney, C. G., Burgasser, A. J., & Kirkpatrick J. D. 2003, ApJ, 126, 975
- Toloba, E., et al. 2011, A&A, 526, 114
- , 2009, ApJ, 707, L17
- Toloba, E., et al. 2012, A&A, 548, A78
- Toomre, A. 1964, ApJ, 139, 1217
- Turner, M. L., et al. 2012, ApJS, 203, 5
- Tutukov, A. V. & Fedorova, A. V. 2006, A. Rep., 50, 785
- van den Bergh, S. 1976, ApJ, 206, 883
- van Zee, L., Skillman, E. D., & Haynes, M. P. 2004, AJ, 128, 121
- Vollmer, B., Cayatta, V., Balkowski, C., & Duschl, W. J. 2001, ApJ, 561, 708
- Weinmann, S. M., Lisker, T., Guo, Q., Meyer, H. T., & Janz, J. 2011, MNRAS, 416, 1197
- Weinzirl, T., Jogee, S., Khochfar, S., Burkert, A., & Kormendy, J. 2009, ApJ, 696, 411
- Wirth, A. & Gallagher, III, J. S. 1984, ApJ, 282, 85

**Table 3**  
Observations and global galaxy parameters

Galaxy	Right ascension	Declination	Telescope	Campaign	$t_{\text{exp}}$	Seeing	$S/N$	$m_H$	$r_e$ ["]	$b/a$	$C$	$\log \rho_{10}$	Add. information
VCC0009	12:09:22.3	+13:59:22	TNG	2010/Mar	222	0.88	1.3	10.59	33.9	0.83	2.83	1.29	F06
VCC0021	12:10:23.1	+10:11:23	NTT	Archive	12	0.74	-	12.14	14.2	0.58	3.03	0.99	F06
VCC0033	12:11:07.7	+14:16:08	NTT	Archive	12	0.81	-	12.17	9.7	0.94	2.74	1.5	F06
VCC0140	12:15:12.5	+14:25:13	TNG	2010/Apr	30	0.81	4.7	11.0	10.6	0.71	3.03	1.86	F06
VCC0165	12:15:53.3	+13:12:53	TNG	2010/Apr	30	0.94	3.4	11.34	8.5	0.89	3.95	2.22	
VCC0170	12:15:56.4	+14:25:56	NTT	2010/Mar	172	1.03	1.5	11.45	27.3	0.65	3.14	1.94	
VCC0173	12:16:00.4	+08:12:00	NTT	2010/Mar	70	1.05	0.9	12.14	14.5	0.92	2.93	1.35	
VCC0178	12:16:09.1	+12:41:09	TNG	2012/Mar	84	1.45	1.6	12.52	10.3	0.57	2.74	1.99	
VCC0200	12:16:33.7	+13:01:34	NOT	2010/Apr	59	0.75	1.5	11.81	12.4	0.97	3.37	2.1	F06
VCC0209	12:16:52.3	+14:30:52	NOT	2011/Mar	76	0.97	1.5	12.1	16.9	0.31	2.83	1.87	
VCC0216	12:17:01.1	+09:24:01	NTT	Archive	15	0.97	-	12.17	12.1	0.65	2.63	1.45	sp, b
VCC0218	12:17:05.4	+12:17:05	TNG	2010/Apr	58	0.92	1.1	11.78	22.4	0.31	3.12	1.79	
VCC0227	12:17:14.5	+08:56:14	NTT	Archive	18	1.12	-	12.37	17.3	0.61	2.61	1.51	
VCC0230	12:17:19.7	+11:56:20	NOT	2010/Apr	78	0.8	1.4	12.51	9.7	0.81	2.99	1.59	F06
VCC0308	12:18:51.0	+07:51:51	NTT	Archive	12	0.72	-	10.99	17.5	0.94	2.95	1.61	sp
VCC0319	12:19:02.0	+13:58:02	TNG	2012/Mar	180	1.99	0.3	12.27	25.8	0.85	2.95	1.83	
VCC0389	12:20:03.1	+14:57:03	TNG	2010/Apr	30	0.79	2.5	10.84	16.3	0.71	3.58	1.79	M11
VCC0407	12:20:18.8	+09:32:19	NOT	Archive	12	0.95	0.6	11.56	18.1	0.72	2.87	1.5	
VCC0437	12:20:48.8	+17:29:49	NTT	Archive	18	0.82	-	10.94	26.7	0.57	3.33	1.46	F06, M11
VCC0490	12:21:38.8	+15:44:39	NOT	Archive	42	0.93	0.7	10.88	23.6	0.76	2.6	2.01	M11, sp
VCC0510	12:21:53.7	+15:38:54	NOT	2011/Mar	179	0.95	1.1	11.85	18.5	0.8	3.03	2.12	M11
VCC0523	12:22:04.1	+12:47:04	NOT	2010/Jan	18	0.9	1.0	10.57	18.9	0.72	3.01	1.9	G00, M11, b, sp
VCC0543	12:22:19.5	+14:45:20	TNG	2010/Apr	63	0.9	1.7	11.24	20.9	0.53	3.23	1.85	F06, M11
VCC0571	12:22:41.1	+07:57:41	NOT	2011/Apr	78	0.81	1.4	12.03	13.5	0.51	3.3	1.9	F06
VCC0575	12:22:43.4	+08:11:43	TNG	2010/Apr	30	0.79	18.6	10.46	6.9	0.61	3.6	1.79	G00, F06
VCC0608	12:23:01.7	+15:54:02	NOT	2010/Jan	36	1.01	0.7	11.72	16.2	0.57	2.87	2.32	M11
VCC0634	12:23:20.0	+15:49:20	NOT	2011/Mar	180	0.76	2.4	10.94	20.5	0.84	3.23	2.22	M11
VCC0698	12:24:05.1	+11:13:05	NOT	2011/Mar	77	0.91	7.9	9.87	19.2	0.43	3.75	1.94	G00, F06, M11
VCC0745	12:24:47.0	+07:21:47	TNG	2010/Mar	26	0.86	1.0	11.77	10.8	0.62	2.99	2.54	
VCC0750	12:24:49.6	+06:45:50	NTT	Archive	18	0.86	-	12.09	15.0	0.72	3.05	2.16	
VCC0751	12:24:48.3	+18:11:48	NTT	2010/Mar	12	0.86	1.3	11.46	11.0	0.62	3.48	1.33	F06, M11
VCC0758	12:24:54.9	+07:26:55	TNG	2012/Mar	84	1.43	6.1	9.57	15.4	0.56	3.41	2.38	G00
VCC0762	12:25:03.0	+07:30:03	TNG	2012/Mar	79	1.38	1.0	12.57	9.3	0.85	2.99	2.25	
VCC0781	12:25:15.2	+12:42:15	NTT	2010/Mar	6	1.87	0.7	11.69	13.8	0.57	3.18	2.47	G00, M11
VCC0786	12:25:14.5	+11:50:15	NOT	2011/Mar	79	0.78	1.2	11.89	26.7	0.42	2.97	2.19	M11
VCC0794	12:25:21.6	+16:25:22	TNG	2010/Mar	183	1.11	1.4	12.17	28.1	0.36	3.16	1.97	M11
VCC0816	12:25:36.1	+15:50:36	NOT	2012/Mar	163	1.6	1.1	12.71	20.7	0.59	2.32	2.14	M11
VCC0817	12:25:36.4	+15:49:36	NOT	2012/Mar	163	1.6	0.7	11.45	21.5	0.86	3.2	2.14	M11
VCC0856	12:25:57.9	+10:03:58	NTT	Archive	12	0.8	-	11.25	14.0	0.89	2.77	2.05	F06, M11, sp
VCC0870	12:26:05.3	+11:48:05	NOT	2010/Apr	96	0.78	1.1	12.02	16.7	0.55	3.07	2.18	
VCC0916	12:26:33.2	+12:44:33	NOT	2012/Mar	74	0.59	3.3	12.18	5.2	0.93	3.29	2.69	
VCC0917	12:26:32.4	+13:34:32	TNG	2010/Apr	26	0.83	0.7	12.41	10.2	0.55	3.14	2.25	M11
VCC0929	12:26:40.5	+08:26:41	NOT	2011/Mar	88	0.76	3.1	10.25	16.1	0.88	3.09	2.24	G00
VCC0940	12:26:47.1	+12:27:47	NTT	2010/Mar	174	1.0	1.4	11.57	18.1	0.73	2.77	2.66	M11, <sup>a</sup>
VCC0949	12:26:54.6	+10:39:55	TNG	2012/Mar	190	1.54	0.6	12.24	21.8	0.63	3.05	1.96	M11
VCC0951	12:26:54.3	+11:39:54	NTT	Archive	6	0.81	-	11.43	19.3	0.71	2.95	2.26	M11
VCC0990	12:27:17.0	+16:01:17	NOT	2010/Jan	8	0.89	1.0	11.48	10.3	0.62	3.27	2.04	M11
VCC1010	12:27:27.4	+12:17:27	NOT	2010/Jan	8	1.21	0.9	10.4	20.4	0.58	3.07	2.43	G00, M11, b, sp
VCC1036	12:27:41.3	+12:18:41	NTT	Archive	6	0.74	-	10.65	19.8	0.43	3.49	2.4	M11
VCC1049	12:27:54.8	+08:05:55	TNG	2010/Mar	10	0.97	1.5	12.13	7.9	0.85	3.14	2.33	F06
VCC1073	12:28:08.6	+12:05:09	TNG	2010/Apr	44	1.0	1.6	10.87	19.6	0.66	3.6	2.28	M11
VCC1075	12:28:12.3	+10:17:12	NOT	2011/Mar	181	0.79	1.2	11.96	18.3	0.65	3.16	2.08	F06, M11
VCC1087	12:28:14.9	+11:47:15	NOT	2011/Mar	72	0.94	1.6	10.86	18.6	0.7	3.05	2.18	F06, M11
VCC1104	12:28:28.1	+12:49:28	TNG	2010/Apr	90	0.83	1.2	12.4	14.1	0.68	2.91	2.45	M11
VCC1122	12:28:41.7	+12:54:42	TNG	2010/Apr	60	0.92	3.3	11.79	16.9	0.43	3.05	2.5	M11
VCC1148	12:28:58.2	+12:39:58	TNG	2010/Apr	24	0.8	2.0	12.26	5.2	0.97	3.7	2.39	M11

Table 3 — *Continued*

Galaxy	Right ascension	Declination	Telescope	Campaign	$t_{\text{exp}}$	Seeing	$S/N$	$m_H$	$r_e$ ["]	$b/a$	$C$	$\log \rho_{10}$	Add. information
VCC1167	12:29:14.7	+07:52:15	NOT	2012/Mar	180	1.7	0.9	12.32	15.6	0.97	2.99	2.53	
VCC1178	12:29:21.3	+08:09:21	NOT	2011/Mar	76	0.67	32.5	9.67	7.4	0.71	3.93	2.41	G00, F06
VCC1183	<i>12:29:22.5</i>	<i>+11:26:02</i>	NTT	Archive	12	0.87	-	11.12	17.0	0.61	3.43	2.04	M11, b
VCC1185	12:29:23.5	+12:27:24	NOT	2012/Mar	185	1.26	0.7	12.4	16.2	0.91	3.01	2.43	F06, M11
VCC1196	12:29:30.9	+14:02:31	TNG	2010/Mar	30	0.9	5.9	10.34	16.8	0.73	3.71	2.15	G00, M11
VCC1254	12:30:05.1	+08:04:05	NOT	2011/Mar	78	1.13	2.0	12.02	11.4	0.98	2.99	2.56	
VCC1261	12:30:10.3	+10:46:10	NOT	2011/Apr	63	0.89	2.2	10.39	21.7	0.58	3.23	1.97	G00, F06, M11
VCC1283	12:30:18.4	+13:34:18	TNG	2010/Mar	29	1.78	7.0	9.86	15.9	0.55	3.25	2.22	G00, F06, M11
VCC1297	12:30:31.9	+12:29:32	TNG	2010/Mar	34	0.97	90.9	10.2	2.6	0.84	3.51	2.61	F06, M11
VCC1304	12:30:39.8	+15:07:40	NOT	2010/Apr	72	0.79	1.7	12.03	16.4	0.33	2.67	2.07	M11
VCC1308	12:30:45.9	+11:20:46	NOT	2012/Mar	82	0.91	0.9	12.43	10.7	0.67	3.01	2.1	M11
VCC1348	12:31:15.7	+12:19:16	NOT	2011/Mar	108	0.74	2.4	12.28	8.9	0.93	3.18	2.54	M11
VCC1355	12:31:20.3	+14:06:20	NOT	2011/Mar	180	0.9	1.1	11.55	22.3	0.76	3.01	2.12	F06
VCC1386	12:31:51.4	+12:39:51	NOT	2011/Apr	43	0.89	0.9	11.78	25.0	0.63	2.83	2.34	M11
VCC1392	12:31:55.9	+12:10:56	NTT	Archive	18	0.68	-	11.81	16.9	0.95	2.49	2.38	M11
VCC1407	12:32:02.7	+11:53:03	NOT	2010/Apr	52	0.86	0.9	11.85	11.9	0.82	3.16	2.16	F06, M11
VCC1422	12:32:14.2	+10:15:14	NOT	2010/Jan	23	1.0	1.3	10.61	17.8	0.86	3.32	1.88	F06, M11, b
VCC1431	12:32:23.5	+11:15:23	NOT	2012/Mar	75	0.91	3.8	11.02	9.1	0.97	3.01	2.38	F06, M11
VCC1440	12:32:33.5	+15:24:34	TNG	2010/Apr	30	0.82	3.8	11.52	7.2	0.97	3.91	2.12	F06, M11
VCC1453	12:32:44.2	+14:11:44	NOT	2010/Apr	47	0.69	1.5	11.0	16.9	0.77	3.6	1.91	M11
VCC1475	12:33:05.0	+16:15:05	NOT	2011/Mar	80	0.92	11.8	9.91	9.2	0.81	3.93	1.87	G00, F06, M11
VCC1479	12:33:07.5	+14:34:08	TNG	2010/Mar	60	1.23	4.7	10.05	23.3	0.4	3.22	2.03	G00, M11
VCC1488	12:33:13.4	+09:23:13	NOT	2011/Mar	75	0.78	1.4	11.96	14.0	0.6	3.16	1.89	F06, M11
VCC1491	12:33:14.0	+12:51:14	NTT	Archive	8	0.8	-	12.04	10.0	0.79	2.89	2.23	M11
VCC1499	12:33:19.8	+12:51:20	NTT	Archive	8	0.8	-	12.49	7.5	0.63	2.99	2.21	F06, M11
VCC1501	12:33:24.7	+08:41:25	TNG	2012/Mar	94	1.54	0.6	12.86	12.0	0.45	3.13	1.93	M11
VCC1512	12:33:34.6	+11:15:35	NTT	2010/Mar	57	0.86	0.9	12.69	12.1	0.74	3.73	2.05	F06, M11
VCC1514	12:33:37.7	+07:52:38	NTT	2010/Mar	180	1.01	1.3	12.19	24.1	0.32	2.89	1.88	M11
VCC1521	12:33:45.0	+10:59:45	TNG	2010/Apr	26	1.19	5.6	10.64	14.6	0.32	3.46	2.17	G00, M11
VCC1528	12:33:51.6	+13:19:52	NTT	Archive	6	0.81	-	11.37	8.4	0.9	3.43	1.95	F06, M11
VCC1545	12:34:11.5	+12:02:12	NOT	2010/Apr	33	0.69	0.7	11.72	9.9	0.77	3.68	2.12	F06, M11
VCC1549	12:34:14.8	+11:04:15	NTT	Archive	12	0.6	-	11.4	11.4	0.81	3.2	2.09	M11
VCC1567	12:34:31.2	+09:37:31	NTT	2010/Mar	104	1.11	0.7	11.26	28.6	0.34	2.89	1.79	M11
VCC1614	12:35:27.3	+12:45:27	NOT	2011/Mar	93	0.78	4.9	11.36	9.0	0.86	2.65	2.18	M11
VCC1627	12:35:37.3	+12:22:37	TNG	2010/Apr	27	1.03	2.0	11.72	3.8	0.89	3.2	2.16	F06, M11
VCC1684	<i>12:36:39.4</i>	<i>+11:06:07</i>	NTT	2010/Mar	167	0.97	1.1	12.48	18.5	0.29	2.97	1.89	M11
VCC1695	12:36:54.8	+12:31:55	NTT	Archive	12	0.63	-	11.57	16.2	0.79	3.62	1.97	F06, M11, sp, b
VCC1743	12:38:06.8	+10:04:07	NOT	2012/Mar	150	0.9	1.1	12.53	15.1	0.39	2.95	2.13	F06, M11
VCC1779	12:39:04.7	+14:43:05	NTT	2010/Mar	67	0.95	1.1	11.99	19.6	0.41	3.2	1.66	F06, M11
VCC1827	12:40:11.9	+08:23:12	NOT	2012/Mar	75	1.65	1.6	10.15	20.7	0.6	3.12	1.61	G00, M11
VCC1828	12:40:13.5	+12:52:13	NOT	2011/Mar	151	0.81	1.4	12.16	15.7	0.7	3.1	1.78	F06, M11
VCC1833	12:40:19.8	+15:56:20	NOT	2011/Mar	65	0.89	4.0	11.3	8.3	0.68	3.31	1.35	F06, M11
VCC1836	12:40:19.6	+14:42:20	NTT	2010/Mar	150	0.98	0.6	11.51	46.8	0.47	3.23	1.63	M11, sp
VCC1857	12:40:53.0	+10:28:53	NOT	2012/Mar	167	1.7	0.2	12.19	26.5	0.52	2.43	1.93	F06, M11
VCC1861	12:40:58.6	+11:11:59	NOT	2011/Mar	76	0.84	1.9	11.13	15.3	0.97	3.28	2.02	F06, M11
VCC1871	12:41:15.8	+11:23:16	TNG	2010/Apr	29	0.86	11.7	10.68	6.9	0.87	3.27	2.24	F06, M11
VCC1876	12:41:20.6	+14:42:21	NOT	2011/Mar	112	0.87	1.4	12.05	16.9	0.51	2.7	1.58	M11
VCC1890	12:41:46.7	+11:29:47	NOT	2011/Mar	193	0.79	0.8	12.03	23.7	0.6	2.7	2.5	M11
VCC1895	12:41:51.9	+09:24:52	NTT	Archive	12	1.01	-	12.04	15.0	0.48	3.03	1.78	F06, M11
VCC1896	12:41:54.6	+09:35:55	NOT	Archive	14	1.17	0.5	11.8	14.9	0.55	2.99	1.84	M11, b, sp
VCC1897	12:41:54.3	+13:46:54	NOT	2011/Apr	107	0.85	0.7	11.38	30.8	0.55	2.87	1.8	M11
VCC1902	12:41:59.5	+12:56:59	NOT	2012/Mar	82	1.55	1.2	9.97	22.4	0.87	3.14	1.94	G00, M11
VCC1910	12:42:08.7	+11:45:09	NOT	2010/Jan	8	1.0	1.0	10.77	11.6	0.81	3.12	2.47	F06, M11, b
VCC1912	12:42:09.1	+12:35:09	NOT	2010/Jan	8	1.16	0.6	11.06	22.2	0.37	3.23	1.97	M11, b
VCC1945	12:42:54.1	+11:26:54	NOT	2011/Mar	96	0.99	0.8	11.73	23.4	0.37	2.64	2.42	M11
VCC1947	12:42:56.3	+03:40:56	NTT	Archive	12	0.93	-	11.06	9.1	0.76	3.16	1.42	b
VCC1949	12:42:57.8	+12:17:58	NOT	2011/Apr	142	1.13	1.9	10.72	25.2	0.44	2.97	2.13	M11, b
VCC2008	12:44:47.4	+12:03:47	TNG	2012/Mar	185	1.61	0.3	12.24	39.2	0.41	2.71	2.04	M11
VCC2012	12:45:05.7	+10:54:06	NOT	2011/Mar	180	1.04	1.2	11.5	21.5	0.83	2.79	1.87	M11
VCC2019	12:45:20.4	+13:41:20	NOT	Archive	20	1.05	0.7	11.33	16.7	0.69	3.18	1.74	F06, M11, sp
VCC2042	12:46:38.3	+09:18:38	NTT	Archive	18	0.69	-	12.42	18.4	0.84	2.66	1.57	M11, sp
VCC2048	12:47:15.3	+10:12:15	NOT	2010/Jan	8	1.22	1.0	10.79	18.5	0.51	3.43	1.7	G00, F06, M11, b
VCC2050	12:47:20.6	+12:09:21	NTT	2010/Mar	44	1.13	0.9	12.19	14.3	0.48	3.03	1.56	F06, M11
VCC2080	12:48:58.4	+10:35:58	NTT	2010/Mar	96	1.1	0.8	12.82	18.8	0.42	3.32	1.64	
VCC2083	12:50:14.5	+10:32:14	NOT	2012/Mar	168	1.54	0.3	12.66	14.1	0.84	2.62	1.57	M11

**Note.** — The coordinates give the position of the galaxy centers of the galaxy as found by the asymmetry centering and by identification of 2MASS stars (the coordinates printed in italics list the NED values). The total on target integration times ( $t_{\text{exp}}$ ) are given in minutes, and the seeing is specified as the full width at half maximum (FWHM) in arcsecs, and the signal-to-noise is given per pixel at  $2r_e$  ( $S/N$ ). The next columns are total brightness ( $m_H$ ), effective radius ( $r_e$ ), the axis ratio  $b/a$  at  $2r_e$ , the concentration index  $C$  (see §3.1), and the local projected density ( $\rho_{10}$ , see Appendix D). The references given in the column with additional information are: G01 – Gavazzi et al. (2001), F06 – Ferrarese et al. (2006), and M11 – McDonald et al. (2011). Furthermore, b and sp indicate that Lisker et al. (2006a) found a bar or spiral arms, or indications for those when printed with italics.

<sup>a</sup>While Lisker et al. (2006a) did not find the bar in VCC0940 with SDSS images, it was reported by Barazza, Binggeli, & Jerjen (2002) using VLT data.

**Table 5**  
Parameters from the decompositions

Galaxy	Group	Simple model				Inner component				Global / outer component				Simple decomposition		Final decomposition		Nucleus	Additional information
		$m$	$r_e$	$n$	$b/a$	$m$	$r_e$	$n$	$b/a$	$m$	$r_e$	$n$	$b/a$	RFF	EVI	RFF	EVI		
VCC0009	L	-	-	-	-	-	-	-	-	10.58	35.0	0.93	0.85	0.019	0.112	-0.001	0.05	N	
VCC0021	1	12.19	12.3	1.24	0.62	-	-	-	-	-	-	-	-	-	-	-	-	-	
VCC0033	1	12.2	8.8	0.98	0.89	-	-	-	-	-	-	-	-	-	-	-	-	-	
VCC0140	2	-	-	-	-	12.12	5.6	0.96	0.69	11.52	14.3	0.72	0.73	0.02	0.26	-0.012	-0.069	N	
VCC0165	L	11.27	9.6	3.4	0.87	11.58	7.8	3.54	0.87	13.31	14.1	0.27	0.81	0.012	0.495	0.001	0.315	-	
VCC0170	2	-	-	-	-	12.23	15.6	1.14	0.65	12.17	41.4	0.41	0.7	-	-	0.025	0.142	N	
VCC0173	2	12.06	15.7	1.48	0.89	14.66	6.3	1.63	0.64	12.25	15.6	1.0	0.93	0.018	0.083	0.012	0.048	-	sp
VCC0178	1	12.53	10.1	0.95	0.55	-	-	-	-	-	-	-	-	-0.006	-0.043	-	-	N	
VCC0200	L	11.8	12.3	1.82	0.91	13.43	5.8	1.6	0.74	12.2	16.6	1.0	0.92	0.017	0.111	0.009	0.055	-	
VCC0216	1	12.18	12.5	0.87	0.67	-	-	-	-	-	-	-	-	-	-	-	-	-	sp
VCC0227	1	12.37	17.5	0.87	0.62	-	-	-	-	-	-	-	-	-	-	-	-	N	
VCC0230	1	12.54	9.2	1.25	0.82	-	-	-	-	-	-	-	-	0.011	0.595	-	-	N	
VCC0308	2	10.81	21.1	1.85	0.94	13.07	5.0	1.14	0.88	11.18	19.4	0.63	0.96	-0.011	-0.028	-0.029	-0.087	N	sp
VCC0319	1	12.29	21.2	1.26	0.88	-	-	-	-	-	-	-	-	-0.057	-0.147	-	-	N	
VCC0389	L	10.85	15.8	1.91	0.79	-	-	-	-	11.16	20.6	0.89	0.85	0.025	0.652	0.012	0.584	N	
VCC0407	B	11.64	14.5	0.99	0.71	-	-	-	-	11.68	16.9	1.0	0.69	0.026	0.069	0.02	0.048	-	
VCC0437	2	10.88	24.6	1.72	0.64	12.52	8.5	1.14	0.78	11.19	33.9	1.0	0.54	-	-	-	-	N	
VCC0490	2	10.86	23.0	0.94	0.78	13.05	18.9	3.38	0.78	11.05	23.4	0.67	0.73	0.031	0.78	0.019	0.388	-	sp
VCC0510	1	11.8	19.7	1.51	0.83	-	-	-	-	-	-	-	-	0.017	0.128	-	-	N	
VCC0523	2	10.53	18.5	1.5	0.77	12.75	7.1	1.15	0.63	10.73	21.4	1.0	0.69	0.015	0.051	0.0	-0.013	-	
VCC0543	2	11.25	19.9	1.65	0.54	13.12	6.7	0.92	0.53	11.49	24.1	1.0	0.57	0.017	0.164	0.009	0.059	-	
VCC0571	2	11.83	17.2	2.78	0.57	14.2	2.5	1.62	0.68	12.24	14.7	1.0	0.56	0.038	0.332	0.018	0.119	-	
VCC0608	B	11.73	17.1	1.2	0.64	14.73	5.9	1.77	0.58	11.96	19.4	0.9	0.71	0.012	0.057	0.005	0.011	-	
VCC0634	L	10.95	19.4	1.51	0.81	-	-	-	-	11.13	24.7	1.0	0.78	0.03	0.453	0.017	0.268	N	
VCC0745	1	11.78	10.1	1.34	0.63	-	-	-	-	-	-	-	-	-0.001	0.007	-	-	N	
VCC0750	L	11.98	16.1	1.51	0.77	-	-	-	-	12.04	16.8	1.29	0.72	-	-	-	-	N	
VCC0751	2	11.46	12.2	2.04	0.58	12.73	5.5	1.38	0.49	11.95	14.5	1.0	0.74	0.012	0.058	0.003	0.004	N	
VCC0758	2	9.56	15.4	2.04	0.54	11.01	6.0	1.04	0.47	9.93	19.7	1.0	0.63	0.032	3.045	0.023	1.573	-	
VCC0762	2	12.62	8.3	1.27	0.83	13.53	5.2	0.87	0.86	13.15	13.8	1.0	0.8	0.002	0.015	-0.001	-0.007	N	
VCC0781	2	11.68	12.8	1.52	0.59	13.94	3.9	0.65	0.73	11.87	14.8	1.0	0.57	0.006	-0.003	0.003	-0.015	N	
VCC0816	1	12.61	21.8	0.73	0.54	-	-	-	-	-	-	-	-	0.008	0.031	-	-	-	
VCC0817	2	11.44	19.6	1.52	0.91	13.38	6.3	0.7	0.93	11.59	26.8	1.0	0.86	0.023	0.132	0.004	0.017	-	
VCC0856	1	11.26	14.0	1.02	0.9	-	-	-	-	-	-	-	-	-	-	-	-	N	sp
VCC0870	2	11.98	16.4	1.57	0.59	14.49	4.1	0.82	0.68	12.15	17.8	1.0	0.58	0.022	0.271	0.017	0.265	N	
VCC0916	1	12.16	5.4	1.87	0.94	-	-	-	-	0.007	0.073	-	-	-	-	-	-	N	
VCC0917	2	12.36	9.1	1.82	0.57	14.53	2.2	1.19	0.78	12.62	10.3	1.0	0.52	-0.003	-0.018	-0.013	-0.061	-	
VCC0929	1	10.26	16.0	1.5	0.87	-	-	-	-	0.016	0.37	-	-	-	-	-	-	N	
VCC0940	B	11.55	19.3	1.14	0.81	14.4	5.1	0.85	0.93	11.81	20.4	0.74	0.92	0.019	0.143	0.014	0.103	N	
VCC0949	1	12.28	19.7	1.18	0.67	-	-	-	-	-0.046	-0.148	-	-	-	-	-	-	-	
VCC0951	1	11.39	19.1	1.29	0.72	-	-	-	-	-	-	-	-	-	-	-	-	N	
VCC0990	2	11.5	10.0	1.66	0.67	16.76	1.8	0.95	0.38	11.52	9.8	1.59	0.69	0.001	0.011	-0.001	-0.029	-	
VCC1010	B	10.3	23.4	1.74	0.54	13.93	2.6	0.9	0.71	10.52	23.4	1.0	0.57	-0.0	-0.015	-0.009	-0.052	-	
VCC1049	L	12.08	7.9	1.81	0.82	-	-	-	-	12.23	7.9	2.04	0.83	0.006	0.023	0.0	0.017	-	
VCC1073	B	10.8	20.8	2.46	0.74	12.29	6.1	1.45	0.81	11.36	29.0	0.68	0.76	0.007	0.09	-0.002	0.086	-	
VCC1075	2	11.97	18.3	1.39	0.69	13.64	8.5	0.84	0.6	12.2	22.5	1.0	0.79	0.021	0.14	0.015	0.094	N	
VCC1087	L	10.79	18.8	1.47	0.72	-	-	-	-	10.93	20.8	1.0	0.68	0.012	0.076	0.007	0.046	N	
VCC1104	L	12.46	12.8	1.08	0.69	-	-	-	-	12.51	14.1	1.0	0.69	0.008	0.051	0.004	0.028	N	
VCC1148	L	12.24	5.5	2.47	0.96	-	-	-	-	12.27	5.8	3.02	0.94	-0.011	0.116	-0.024	-0.126	N	
VCC1167	1	12.28	15.5	1.48	0.96	-	-	-	-	-	-	-	-	0.004	0.02	-	-	N	
VCC1183	L	11.15	13.6	1.72	0.8	13.49	4.0	1.02	0.7	11.39	22.3	1.0	0.54	-	-	-	-	N	
VCC1185	1	12.37	16.4	1.48	0.94	-	-	-	-	0.007	0.036	-	-	-	-	-	-	N	
VCC1254	2	11.93	12.7	1.4	0.98	15.4	1.4	1.22	0.93	12.02	12.8	1.0	0.93	0.032	0.495	0.013	0.093	N	
VCC1261	2	10.33	22.3	1.87	0.62	13.27	3.5	1.23	0.92	10.48	23.1	1.22	0.57	0.019	0.243	0.003	0.033	N	
VCC1283	B	9.86	18.9	1.64	0.59	12.05	4.1	0.98	0.71	10.45	21.2	1.0	0.96	0.067	4.557	0.015	0.754	-	



Table 5 — Continued

Galaxy	Group	Simple model				Inner component				Global / outer component				Simple decomposition		Final decomposition		Nucleus	Additional information
		<i>m</i>	<i>r<sub>e</sub></i>	<i>n</i>	<i>b/a</i>	<i>m</i>	<i>r<sub>e</sub></i>	<i>n</i>	<i>b/a</i>	<i>m</i>	<i>r<sub>e</sub></i>	<i>n</i>	<i>b/a</i>	RFF	EVI	RFF	EVI		
VCC1308	2	12.47	9.6	1.22	0.67	13.81	5.1	0.92	0.84	12.82	13.7	1.0	0.57	0.008	0.038	0.005	0.027	N	
VCC1348	2	12.24	9.6	1.59	0.96	13.79	5.8	2.29	0.84	12.6	10.7	1.0	0.87	0.028	1.296	0.021	1.801	N	
VCC1355	2	11.46	26.3	1.48	0.81	12.89	14.2	1.17	0.68	11.81	30.9	0.8	0.96	0.013	0.094	0.012	0.089	N	
VCC1386	<i>B</i>	11.77	23.3	1.06	0.64	-	-	-	-	11.82	25.7	1.0	0.62	0.223	-0.19	0.015	0.13	N	
VCC1392	<i>B</i>	11.8	21.3	0.83	0.54	-	-	-	-	11.83	26.6	1.0	0.57	-	-	-	-	-	
VCC1407	1	11.9	11.1	1.44	0.83	-	-	-	-	-	-	-	-	0.003	0.017	-	-	N	
VCC1422	2	10.54	19.2	1.95	0.79	11.58	10.0	1.53	0.72	11.13	27.2	1.0	0.81	0.005	0.01	-0.0	-0.007	-	
VCC1431	1	11.01	9.2	1.48	0.96	-	-	-	-	-	-	-	-	0.006	0.092	-	-	N	
VCC1440	2	11.57	6.5	3.33	0.97	12.3	3.2	1.84	0.97	12.5	14.4	1.0	0.91	-0.015	0.21	-0.023	-0.126	N	
VCC1453	2	10.93	18.3	2.22	0.77	12.48	6.1	1.36	0.74	11.34	22.1	1.0	0.82	0.012	0.158	0.01	0.106	N	
VCC1488	2	12.01	13.0	1.39	0.6	13.47	6.0	0.93	0.64	12.31	17.9	1.0	0.59	0.02	0.135	0.015	0.093	-	
VCC1491	2	12.11	8.8	1.06	0.79	13.22	5.5	0.78	0.84	12.5	13.2	1.0	0.72	-	-	-	-	N	
VCC1499	<i>B</i>	12.54	7.8	1.15	0.63	-	-	-	-	12.62	8.3	1.0	0.68	-	-	-	-	-	
VCC1501	1	12.95	11.5	1.4	0.46	-	-	-	-	-	-	-	-	-0.006	-0.025	-	-	-	
VCC1512	2	12.3	20.8	4.04	0.79	14.34	2.7	2.05	0.85	13.0	15.0	1.0	0.72	0.024	0.127	0.014	0.064	-	
VCC1528	2	11.35	8.8	2.06	0.83	12.94	3.0	1.22	0.75	11.71	10.7	1.0	0.92	-	-	-	-	-	
VCC1545	2	11.67	9.6	2.57	0.84	12.72	4.0	1.9	0.89	12.36	14.0	1.0	0.73	0.002	0.007	-0.001	-0.004	N	
VCC1549	1	11.36	12.1	1.71	0.83	-	-	-	-	-	-	-	-	-	-	-	-	N	
VCC1614	<i>L</i>	11.43	8.6	0.83	0.88	-	-	-	-	11.61	10.7	1.0	0.93	0.039	1.084	0.02	0.634	N	
VCC1627	1	11.72	3.9	1.95	0.87	-	-	-	-	-	-	-	-	-0.032	-0.064	-	-	N	
VCC1695	2	-	-	-	-	13.25	5.0	1.05	0.63	11.85	20.5	1.0	0.81	-	-	-	-	N	
VCC1743	2	12.55	15.7	1.17	0.44	13.94	9.7	0.82	0.35	12.83	19.6	1.0	0.51	0.008	0.041	0.004	0.021	-	
VCC1779	2	12.04	16.9	1.52	0.48	13.49	7.1	0.94	0.51	12.32	24.8	1.0	0.45	0.041	0.262	0.029	0.175	-	
VCC1827	<i>B</i>	10.03	24.7	1.91	0.71	13.07	3.4	0.86	0.85	10.53	25.5	0.52	0.8	0.081	1.165	0.013	0.135	N	
VCC1828	1	12.13	15.1	1.46	0.71	-	-	-	-	-	-	-	-	0.009	0.052	-	-	N	
VCC1836	2	11.46	35.5	1.65	0.55	13.18	11.2	1.03	0.72	11.69	52.2	1.0	0.43	-0.034	-0.087	-0.047	-0.121	-	
VCC1857	1	12.19	26.1	0.72	0.53	-	-	-	-	-	-	-	-	0.01	0.04	-	-	-	
VCC1861	<i>L</i>	11.15	14.5	1.48	0.97	-	-	-	-	11.32	18.9	1.0	0.93	0.031	0.423	0.015	0.148	N	
VCC1871	<i>L</i>	10.64	7.4	1.97	0.87	-	-	-	-	10.75	7.2	2.21	0.86	0.013	5.85	-0.001	2.587	-	
VCC1876	1	12.07	16.1	0.92	0.51	-	-	-	-	-	-	-	-	0.006	0.052	-	-	N	
VCC1890	1	12.01	23.4	0.97	0.6	-	-	-	-	-	-	-	-	0.021	0.108	-	-	-	
VCC1895	1	12.08	13.1	1.32	0.47	-	-	-	-	-	-	-	-	-	-	-	-	-	
VCC1896	<i>B</i>	11.77	16.6	1.28	0.71	14.61	3.6	0.73	0.79	12.26	19.6	0.47	0.85	0.004	0.002	-0.006	-0.029	N	
VCC1897	2	11.31	30.5	1.5	0.59	14.26	5.8	1.12	0.93	11.45	32.3	1.0	0.54	0.018	0.072	0.009	0.034	-	
VCC1902	2	9.84	27.3	1.99	0.8	11.38	10.0	1.79	0.69	10.34	27.6	0.64	0.86	0.043	0.612	0.011	0.093	N	
VCC1910	2	10.73	12.5	1.58	0.84	11.71	8.4	1.48	0.74	11.35	15.5	1.0	0.92	-0.005	-0.034	-0.006	-0.039	-	
VCC1947	<i>B</i>	11.08	9.6	1.52	0.79	12.39	9.3	3.12	0.69	11.56	9.9	1.0	0.94	0.004	0.103	0.002	0.002	N	
VCC1949	<i>B</i>	10.66	29.0	1.47	0.5	14.96	4.5	1.4	0.65	11.12	31.4	0.52	0.64	0.069	0.651	0.021	0.166	-	sp
VCC2008	1	12.3	35.6	0.86	0.44	-	-	-	-	-	-	-	-	-0.078	-0.174	-	-	-	
VCC2012	1	11.45	22.6	1.18	0.85	-	-	-	-	-	-	-	-	0.015	0.092	-	-	-	
VCC2019	1	11.37	17.0	1.36	0.71	-	-	-	-	-	-	-	-	0.012	0.033	-	-	N	sp
VCC2042	1	12.38	18.5	1.04	0.96	-	-	-	-	-	-	-	-	-	-	-	-	N	
VCC2050	2	12.2	15.0	1.38	0.5	13.08	10.2	1.1	0.44	12.8	20.8	1.0	0.63	0.012	0.048	0.011	0.043	N	
VCC2080	<i>B</i>	-	-	-	-	-	-	-	-	12.87	20.1	1.61	0.46	-	-	0.016	0.071	N	
VCC2083	1	12.71	13.8	0.86	0.85	-	-	-	-	-	-	-	-	0.005	0.019	-	-	N	

**Note.** — The table lists the details of the decompositions for the 99 galaxies, for which the analysis was done. The columns list the structural group (with less certain group assignments printed with italics), the parameters (integrated brightness *m*, half-light radius *r<sub>e</sub>*, Sérsic index *n*, and the axis ratio *b/a*) of the simple, as well as the inner and global or outer components of the final model, where applicable. ‘Global component’ refers to the main component in galaxies with a lens in addition to one other component. Furthermore, we give the RFF and EVI indices for both models (see §3.4.3). Values are omitted for archive data and in case the one-component models with nucleus failed for galaxies, for which the final model includes a nucleus (‘N’ in the second last column). The parameters of nuclei, lenses, and bars that resulted from our best fits are not used in our analysis, but can be provided on request for specific objects. The final column indicates where there are hints of spiral arms in the residual images.